STUDYING NEUTRON-STAR AND BLACK-HOLE BINARIES WITH GRAVITATIONAL-WAVES

by

SERENA VINCIGUERRA

A thesis submitted to the University of Birmingham for the degree of
DOCTOR OF PHILOSOPHY

School of Physics and Astronomy
College of Engineering and Physical Sciences
University of Birmingham
March, 2018

UNIVERSITY OF BIRMINGHAM

University of Birmingham Research Archive

e-theses repository

Abstract

The revolutionary discoveries of the last few years have opened a new era of astronomy. With the detection of gravitational-waves, we now have the opportunity of investigating new phenomena, such as mergers of black-holes. Furthermore, multi-messenger observations now allow us to combine information from different channels, providing insight into the physics involved. With this rapid evolution and growth of the field, many challenges need to be faced.

In this thesis we propose three data analysis strategies to efficiently study the coalescences of compact binaries. First we propose an algorithm to reduce the computational cost of Bayesian inference on gravitational-wave signals. Second we prove that machine-learning signal classification could enhance the significance of gravitational-wave candidates in unmodelled searches for transients. Finally we develop a tool, `saprEMo`, to predict the number of electromagnetic events, which according to a specific emission model, should be present in a particular survey.

Acknowledgements

Alice:"How long is forever?"

White Rabbit:"Sometimes, just one second."
— Lewis Carroll, *Alice in Wonderland*

Three years away from my family and away from my world, they really felt *forever* at the beginning of my PhD. And yet, despite the challenges, in a second they were gone. In the few last years I have (re)discovered myself and for this I have only to thank the incredible people in my life.

To my mom and dad, who have always supported me and my decisions. Who have helped me to find a direction, who have been always there for me with kind words and warm hugs, and have been so strong for me when I had to face the difficulties of being away. Who have never asked me to come back (I know they have both been missing me a lot ;)), who had the strength to tell me what I needed to hear and who taught me to never give up. Thank you for being such fabulous parents!

To Stefano, Luca, Matteo and Giorgio, my fantastic and loud little brothers, who have always had a joke to make me smile, who have always had encouraging words, who have always had a story to tell, who have always had sweet hugs for me.

Thank you for being the fantastic people you are! To all my grandparents, who have supported me along all the way, who have spoiled me for years with their wonderful attention and who have made my life full of interesting stories. Who have been so close, and who taught me that it is not only possible to survive but also accomplish great achievements even being away from home. Thank you for all!

Thanks to my cousin Alex, who has been showing me how fun is to travel. Who knows where I will meet you next time!

To all my uncles and my big family, made of such wonderful and supportive people, thank you very much. I love you all!

Thank you, Matteo Michelini, for the incredible support you have been giving me throughout these years. I will always be grateful to have had you by my side. I would also like to express my gratitude to Matteo's family: Daniele, Gianni and Antonia, you all have been like a second family to me, and I am extremely grateful to have met you and to all the fantastic moments that we shared. Thank you for all your support and care.

To Matteo's uncles and cousins, thank you for your honesty, for your opinions and for the happy moments.

To Alessandro, Cristian, Stefano and Rosanna, thank you very much for having been such a great company when I was back, and thank you for being such close friends to Matteo!

To Elisa, thank you for the Skype calls during my Sundays alone!

Thank you to all my fantastic friends in Italy (Arianna Balter, Cristina Zoro (even though not in Italy), Gianfranco Dalbosco, Rocco Spagnolli, Mary Tringali, etc.)! Thank you, Valeria, for your visits, it's always a pleasure to spend time with you! And special thanks to Alexandra Zampedri and Silvia Romagna in particular, who supported me and listened to me both during my crises and my happy days. Really, thank you to you, who have always been there for me!

Thank you to all the great people I met here in Birmingham!

Thank you to my fantastic friends Daniel Töyra, Hannah Middleton, Jim Barrett, Matt Hunt, Bethany Wells, Coen Neijssel, Alejandro Vigna-Gómez, Kat Grover, Matteo Bianconi, Jake Crosset, Miguel Dovale, Anna Green, Morwenna Kearns, Karin De Figueiredo, Aleksandra Dajcz and Celine Bisson for the fun evenings spent together! Thank you all for having made my stay away from home much easier, for

and for being such nice friends, thank you!

To all the friends and fantastic people I met in the GraWIToN project and the schools in general, thank you.

To Shubhanshu Tiwari, Marco Drago and Giovanni Andrea Prodi, for being always so friendly and available for discussions. For helping, any time I asked, and for not asking for too many details on the fish dinners that I owe to some of them.

I am extremely grateful to Marica Branchesi and her family for their availability and incredible hospitality during my secondment in Urbino. It has been a real pleasure to meet such a great family, thank you.

I would also like to thank Riccardo Ciolfi for his help and availability.

To Michele Punturo, Elena Cuoco and Erika Morucci, thank you very much for having given us the fantastic and insightful opportunities of being part of the Initial Training Network, GraWIToN. Thank you for all the schools, the outreach activities and all the experiences that you have allowed us to take part in. These past years have been amazing!

I also would like to express my very great appreciation to my examiners Will M. Far and Ik Siong Heng for the patience in reading, the corrections, the thoughts and the suggestions on my thesis; it has really been interesting to discuss about it with you. Thank you!

To all the people I met, from the cleaning people, to the pub staff, students and professors, thank you! You all have contributed to this incredible experience!

A special thank to Coen Neijssel, Jim Barrett and Morwenna Kearns, who beside being fantastic people have also helped me by checking and proofreading this thesis.

On behalf of the authors of the published papers (Vinciguerra et al., 2017b), (Vinciguerra et al., 2017a) and of the paper draft presented in session 5.2, I would like to thank Rory Smith, Ilya Mandel, Neil Cornish, A. Belfiore, A. De Luca, M.Marelli,

D. Salvietti, A. Tiengo and R. Salvaterra for their comments and availability.

Thank you all for having contributed to my journey, this fantastic adventure, which is life!

> *But it's also true that the person who risks nothing, does nothing; has nothing. All we know about the future is that it will be different. But, perhaps what we fear is that it will be the same. So, we must celebrate the changes. Because, as someone once said "Everything will be all right in the end. And if it's not all right, then trust me, it's not yet the end."*
> —*The Best Exotic Marigold Hotel*

Declaration

In chapter 1 I report some basic concepts on the science of gravitational-waves, from the main observations to a brief overview on their theoretical properties and on gravitational-wave detectors. Chapter 2 outlines what are the expected gravitational-wave sources, specifically focusing on compact binary coalescences. Gravitational-waves emitted by mergers of compact objects, such as neutron-stars and black-holes, are indeed the main signals investigated in the projects presented in the following chapters. In chapter 3, after a brief introduction on parameter estimation and related computational challenges, I report the paper published in *Classical and Quantum Gravity* (Vinciguerra et al., 2017b), led by myself in collaboration with John Veitch and Ilya Mandel. Chapter 4 introduces and then reproduces the work carried out by myself in collaboration with Marco Drago, Giovanni Andrea Prodi, Sergey Klimenko, Claudia Lazzaro, Valentin Necula, Vaibhav Tiwari, Maria Concetta Tringali, Gabriele Vedovato, which led to the publication in *Classical and Quantum Gravity* of the paper (Vinciguerra et al., 2017a). In Chapter 5, after a brief introduction to the emission expected from mergers of binary neutron-stars, I present a tool aimed at predicting the number of electromagnetic events, generated by a specific source, expected in a particular survey. I developed the project with Marica Branchesi, Riccardo Ciolfi, Ilya Mandel, Coenraad Neijssel and Giulia Stratta. Methodology and results are presented in a paper draft (at the time of the thesis writing - March 2018), which we intend to submit to *Astronomy & Astrophysics*. In chapter 6, the work discussed in the thesis is briefly summarised in view of future projects.

Contents

Chapter 1

Introduction to

gravitational-waves

Some of the materials constituting chapter 1 belongs to my Mid Course Assessment and master thesis.

In November 25, 1915 Albert Einstein presented to the Prussian Academy his revolutionary theory of General Relativity (GR) (Einstein, 1916), (Einstein, 1918). His work drastically changed our interpretation of the physical laws, revealing deep connections between them and space-time geometry. Several extraordinary phenomena were predicted as consequences of the application of GR; by now some of these effects are proven, whereas others remain theoretical predictions. Among the most recent GR confirmation is the existence of gravitational-waves (GWs). GWs are ripples in space-time which propagate at the speed of light. Their existence is derived as a solution of the Einstein field equations, which are considered one of the key relations disclosed by GR. Before the first GW direct detection, GW150914 (Abbott et al., 2016d), GWs were indirectly supported by the orbital decay of the binary pulsar PSR 1913+16. This system was discovered from a radio signal by Hulse and Taylor in 1974 (Hulse and Taylor, 1975). Over the years, its period has been repeatedly measured, demonstrating that its orbital decay is consistent with

GR predictions on energy lost by the emission of GWs (Taylor and Weisberg, 1982). In 1993, this indirect proof of the existence of GWs, gave Hulse and Taylor the Nobel Prize.

Starting from the 1960s, many efforts have been devoted to the construction and development of infrastructures dedicated to direct detections of GWs. In early 2000, such efforts were realised in the first network of kilometers long ground-based interferometers, composed of the two Laser Interferometer Gravitational-wave Observatories (LIGOs) and the Virgo detector. No GW detection was claimed after the first scientific runs of these interferometers, which ended in 2010 to allow substantial upgrades of both sites and data analysis infrastructures. In fall 2015, the LIGO interferometers were again operational, opening the first observing run in their early advanced configuration with the first GW detection, observed on the 14th of September 2015 (Abbott et al., 2016d). The era of GW astronomy had then begun, leading to multiple detections both during the first (O1) and the second (O2) observing runs. During O2 Virgo also became operational, leading to considerable improvements in the sky localisation of GW sources. Nowadays the science of GWs is focused on detection and investigation of direct GW signals.

In the following we outline the main theoretical background which predicts the existence of GWs (section 1.1), we mention the main present and future GW-detectors (section 1.2) and finally report a brief overview of the GW signals observed so far (section 1.3).

1.1   The theory of gravitational-waves

In this section we briefly present the theory behind gravitational-waves, following the notes (Kostas, 2002), (Cognola, 2016), (Ravanini, 2008) and the books (Misner et al., 2017), (Maggiore, 2000).

1.1.1 Einstein Field Equations

GR is developed in the geometrical framework of a four-dimensional manifold. In this manifold an *event* is identified by 4 coordinates (x_0, x_1, x_2, x_3): where x_0 is related to the time t, $x_0 = ct$ with c speed of light, and the others x^i $(i = 1, 2, 3)$ describe the spatial location.

The Einstein field equations are one of the key results achieved by GR. They connect the gravitational potential and the associated metric g, to the physical properties of the matter, described by the energy-momentum tensor T. They are differential equations which at the Newtonian limit reduce to the Poisson equation $\nabla^2 \phi = 4\pi G \mu_0$, where ϕ is the newtonian gravitational potential, μ_0 is the mass density and G the universal gravitational constant. As suggested by this limiting case, the Einstein tensor $G_{\mu\nu}$ contains second derivatives of the gravitational potential. Indeed $G_{\mu\nu} = R_{\mu\nu} - \frac{1}{2} R g_{\mu\nu}$, where $R = g^{\mu\nu} R_{\mu\nu}$ is the scalar curvature and $R_{\mu\nu}$ is the Ricci tensor, defined as a contraction of the Riemann tensor $R_{\mu\nu} = R^{\sigma}_{\mu\sigma\nu}$. The Riemann tensor marks the effect of curved space in parallel transporting vectors on a closed curve. Calculated as commutator between covariant derivatives in two directions of the space-time, it can be expressed as a function of Christoffel symbols $\Gamma^{\sigma}_{\nu\mu}$ [1] as:

$$R^{\sigma}_{\mu\tau\nu} = \partial_{\tau} \Gamma^{\sigma}_{\nu\mu} - \partial_{\nu} \Gamma^{\sigma}_{\tau\mu} + \Gamma^{\sigma}_{\tau\gamma} \Gamma^{\gamma}_{\nu\mu} - \Gamma^{\sigma}_{\nu\gamma} \Gamma^{\gamma}_{\tau\mu} \tag{1.1}$$

Here we adopt the notation ∂_{σ} to label $\frac{\partial}{\partial x^{\sigma}}$ with $\sigma = 0, 1, 2, 3$. The Einstein field equations are:

$$G_{\mu\nu} = \frac{8\pi G}{c^4} T_{\mu\nu} \quad \mu, \nu = 0, 1, 2, 3 \tag{1.2}$$

The number of independent equations is cut down from 16 to 10 by symmetry arguments. One of the fundamental tasks of the modern theories of gravity is finding their solutions and comparing them to physical phenomena, such as Black-Holes (BHs) and Neutron-Stars (NSs). The main challenge come from their strong non-linearity

---

[1]$\Gamma^{\sigma}_{\nu\mu} = \frac{1}{2} g^{\sigma\gamma} \left(\partial_{\mu} g_{\nu\gamma} + \partial_{\nu} g_{\mu\gamma} - \partial_{\gamma} g_{\nu\mu} \right)$

and from the consequent invalidity of the superposition principle. At the moment only few exact solutions have been determined (Schwarzschild, 1916), (Finkelstein, 1958), (Kruskal, 1960), (Kerr, 1963), leading the development of approximations and numerical techniques. Gravitational-Waves (GW) are solutions of these equations (1.2), which consist in space-time perturbations propagating at the speed of light c, in this context also known as *speed of gravity*.

1.1.2   Gravitational-waves

Far away from the GW source, the effects of changes in mass distributions on the space-time geometry act as weak gravitational fields, which can be described adopting a perturbative approach. In this framework we can adopt the *linear approximation*, which represent the space-time variations (namely the GWs) with a tensor $h_{\mu\nu}$ added to the stationary metric component $\eta_{\mu\nu}$:

$$g_{\mu\nu} = \eta_{\mu\nu} + h_{\mu\nu} + O(|h_{\mu\nu}^2|) \tag{1.3}$$

where $|h_{\mu\nu}| \ll 1$.

Under these conditions the Einstein equations can be reduced to simpler relations, known as **linearised field equations**. Adopting the *Hilbert's gauge condition* $\partial_\mu h^{\mu\nu} = 0$, they can be formulated as:

$$-\frac{1}{2}\Box \left(h_{\mu\nu} - \frac{1}{2}\eta_{\mu\nu}h \right) = \frac{8\pi G}{c^4}T_{\mu\nu} \tag{1.4}$$

where $\Box$ is the Laplace-Beltrami operator. This result shows the key role of the wave equation, which governs the tensor:

$$\bar{h}_{\mu\nu} \equiv h_{\mu\nu} - \frac{1}{2}\eta_{\mu\nu}h \tag{1.5}$$

We can therefore describe GW emission and propagation with the system:

$$
\begin{cases}
\Box \bar{h}_{\mu\nu} = -\dfrac{16\pi G}{c^4} T_{\mu\nu} \\[2em]
\partial_\nu \bar{h}_{\mu\nu} = 0
\end{cases}
\tag{1.6}
$$

where $T_{\mu\nu}$ is the energy-momentum tensor which characterises the GW source. The propagation of these space-time ripples in the vacuum is described by setting $T_{\mu\nu} = 0$. By choosing a suitable gauge, it is possible to define the tensor $\bar{h}_{\mu\nu}$ with only two independent components, orthogonal to the direction of propagation. These are usually labelled as *cross* $h_\times$ and *plus* h_+ polarisations. The coordinate frame defined by these conditions can be characterised by null trace and time-components and it is therefore called **Transverse-Traceless Gauge** (TT). Considering GWs propagating in the z direction the only components different from zero are: $h_{11}^{TT}, h_{22}^{TT}, h_{12}^{TT}$ and h_{21}^{TT}. According to the TT Gauge properties, these define the two independent polarisations:

plus polarisation : $h_{xx} = -h_{yy} = h_+$;

cross polarisation : $h_{xy} = h_{yx} = h_\times$.

1.1.3   Gravitational-wave origin and properties

Part of the great interest in GWs is motivated by their weak interaction with matter. They carry almost unaltered information about their astrophysical source, remaining unaffected by phenomena such as absorption and scattering. GWs are therefore key instruments for exploring regions of the Universe characterised by the extreme physical conditions, including events characterised by none or weak electromagnetic counterparts or phenomena whose emission is strongly affected by the surrounding environments.

The process of GW generation is led by the energy-momentum tensor characterising the astrophysical source, so that the right-hand side of the Einstein field equations

has no-null components. The system (1.6) consists in a set of inhomogeneous differential equations whose solutions can be derived by introducing the Green's functions $G(t, \mathbf{x}, t', \mathbf{x}')$. In general the field $f(t, \mathbf{x})$ which solves equations of the form $\Box f(t, \mathbf{x}) = e(t, \mathbf{x})$ is defined by the integral:

$$f(t, \mathbf{x}) = \int G(t, \mathbf{x}, t', \mathbf{x}') e(t', \mathbf{x}') \, dt' dx'^3 \tag{1.7}$$

where the Green's function $G(t, \mathbf{x}, t', \mathbf{x}')$ is the solution of the associated equation $\Box G(t, \mathbf{x}, t', \mathbf{x}') = \delta(t - t')\delta(\mathbf{x} - \mathbf{x}')$, with δ being the Dirac delta function. The application of this technique to our case provides the following solution of the wave equation:

$$\bar{h}_{\mu\nu}(t, \mathbf{x}) = 4 \int \frac{T_{\mu\nu}(ct - |\mathbf{x} - \mathbf{x}'|, \mathbf{x}')}{|\mathbf{x} - \mathbf{x}'|} \, dx^3 \tag{1.8}$$

Taking into account the properties of the energy-momentum tensor, this expression finally results in the **quadrature formula**:

$$h_{\mu\nu}(t, r) = \frac{2G}{c^4} \frac{1}{D_L} \frac{\partial^2 I_{\mu\nu}}{\partial^2 t} \left(t - \frac{r}{c} \right) \tag{1.9}$$

where $D_L = |\mathbf{x}|$ is the luminosity distance of the source and $I_{\mu\nu} = \int d^3x \mu(t, \mathbf{x}) \left(x^\mu x^\nu - \frac{1}{3} R^2 \delta^{\mu\nu} \right)$ is its mass quadrupole moment tensor. In the last equation the $\delta^{\mu\nu}$ is the Kronecker delta and the previous integral is calculated inside the source.

The expression (1.9) reveals that GWs are generated by changes of mass distributions at the quadrupolar order evaluated at the retarded time $t - D_L/c$. This is indeed the first order of the multipolar expansion which is not linked to conservative properties. Equation (1.9) also highlights two other aspects: the weakness of the GW amplitude and its decrease as it propagates through space. The former is due to the factor $G/c^4 \approx 5.6 \times 10^{-42} s^2 \cdot kg^{-1} \cdot m^{-1} \approx 2.8 \times 10^{-12} s^2 \cdot M_\odot \cdot m^{-1}$. The latter is instead due to the inverse proportionality between waveform polarisation amplitudes $h_{\mu\nu}$ and distance from the source D_L.

In GR space-time deformations and matter properties are explicitly connected to each other. GWs propagate carrying energy and are therefore characterised by an appropriate energy-momentum tensor. In the linear approximation, within the TT gauge formalism, the energy-momentum elements different from zero can be defined by $T_{\mu\nu}^{TT} \approx (32\pi)^{-1} \langle \partial_\mu h_{\sigma\gamma} \partial_\nu h^{\sigma\gamma} \rangle_{n\lambda}$, where the symbol $\langle \cdot \rangle_{n\lambda}$ means an average over several wavelengths λ. Taking into account this last formula and the expression for the polarisation amplitudes (1.9), we can define the GW luminosity L_{GW}:

$$L_{GW} = -\frac{dE}{dt} = \frac{1}{5}\frac{G}{c^5}\left\langle \frac{\partial^3 I_{\mu\nu}}{\partial t^3}\frac{\partial^3 I^{\mu\nu}}{\partial t^3}\right\rangle_{n\lambda} \tag{1.10}$$

The extremely low factor $\frac{G}{c^5}$ of this formula remarks, once again, the extreme conditions necessary for the generation of non-negligible GWs. The GW luminosity is expected to roughly be a universal constant (Sathyaprakash, 2013): $L_{GW} \sim \alpha \frac{c^5}{G}$, where α is a factor which depends on the compactness and on the characteristic velocity of the system. The relevant astrophysical sources are characterised by velocities which achieve a considerable fraction of the speed on light and dimensions of the order of the Schwarzschild radius R_S, which lead to values of $\alpha \sim 10^{-1} - 10^{-3}$, almost independently from the masses of the systems [2].

1.2   Gravitational-wave Detectors

Despite GW prediction is dated 1916, it was only after the middle of the last century that a general agreement on the existence of GWs started to spread amongst the scientific community (Saulson, 2011). For a long time gravitational-waves were thought to be just a mathematical artefact, and, in any case, phenomena too weak to be detectable. The same Einstein doubted about their existence at least up to 1936, when he wrote to his friend Max Born the following sentence: "Together with a young collaborator, I arrived at the interesting result that gravitational-waves do

---

[2]Simple arguments allow to approximate $L_{GW} \sim \frac{c^5}{G}\left(\frac{R_S}{R}\right)^2\left(\frac{v}{c}\right)^6 \sim \frac{c^5}{G}$, where we are considering systems characterised by extreme conditions as expected for relevant GW sources (for more details, see following chapter).

Detectors	f[Hz]	Target sources
Cryogenic resonant bars (es. AURIGA, NAUTILUS)	$\approx 10^3$	NSs; Supernovae;
Terrestrial interferometers (es. LIGO, VIRGO, KAGRA, ET)	$\approx (0.01 - 5) \ 10^3$	Compact binary coalescences up to $10^3 \ M_\odot$; NSs; Supernovae; Gamma-Ray Bursts;
Space interferometer LISA/NGO	$\approx (10^{-4} - 10^{-1})$	Binary systems; Hypermassive BHs
Pulsar Timing EPTA/IPTA/SKA	$\approx (10^{-9} - 10^{-6})$	Super Massive Black-Holes Binaries

Table 1.1: Frequency-range and the main target sources of GW detectors.

not exist, though they had been assumed a certainty to the first approximation"
(Betz, 2016).

For this reason the first attempt for GW detection dates back to 1957, when Joseph Weber developed the first acoustic detector. The main idea behind GW-detectors is monitoring the relative distance between two test masses. The simplest idea of two bodies linked by a spring first resulted in the realisation of long metallic bars, which are predicted to vibrate in presence of GWs (Weber, 1960). Despite the great improvements, the sensitivity of these devices have not been sufficient for any GW detection (Astone et al., 2010). A different class of instruments is composed of interferometers in the frequency range of $\sim (0.01 - 5)$ kHz, which precisely measure variations on the position of two freely suspended test mirrors (see schematic diagram in fig. 1.1) (Gerstenshtein and Pustovoit, 1963), (Moss et al., 1971), (Weiss, 1972). The presence of GWs is then recorded by these devices in terms of changes on the interference pattern. At the moment the most sensitive GW-detectors belonging to this class are the two LIGO (Laser Interferometer Gravitational-wave Observatory) interferometers (Riles, 2013), Virgo (Acernese et al., 2014) and GEO (Affeldt et al., 2014). The former are two 4 km-arms detectors located in U.S., one in Livingston, Luisiana ($L1$) and one in Hanford, Washington State ($H1$). Virgo is a 3 km-arms interferometer built in Cascina, Italy, thanks to an Italian-French collaboration while GEO is a 600 m-arms detector located in Hannover, Germany. During the science run of the initial LIGO and Virgo configurations (ended in 2010/2011),
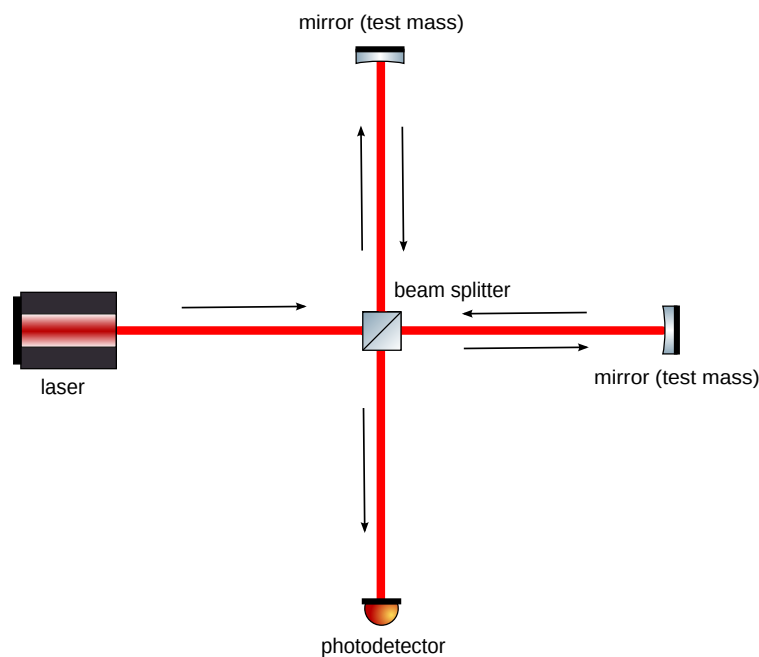
Figure 1.1: Schematic representation of an interferometer. A laser emits a beam of light which is divided in two orthogonal rays by the beamsplitter. They propagate along the arms until the mirrors reflect them back to the beamsplitter, where they destructively interfere, in absence of gravitational signal. When gravitational-waves pass trough such instrument, they change the arm lengths and consequently the interference patterns, revealed by the photodetector. The configuration of the most sensitive ground-based GW-detectors are based on the same operative principle, although to reach the required sensitivity the instruments have been equipped by several additional devices.

no GWs were detected, however, after the recent upgrades, back in 2015 the early aLIGO (Aasi et al., 2015a) was able to directly observe and record the first GWs (Abbott et al., 2016d). Since then more events were detected and with the recent joining of Virgo during observing runs, the sky localisation also improved significantly. While aLIGO and adVirgo will gradually reach the correspondent design configurations, the second generation network will slowly incorporate new interferometers such as KAGRA (Aso et al., 2013) and LIGO-India (Unnikrishnan, 2013), which are expected to be operative respectively in Japan after 2018 and in India after 2022. After 2022 the visible volume is expected to be increased by a factor of ~ 1000 compared to Initial LIGO and Virgo configuration, and of ~ 10 compared to the volume accessible during O2, considerably increasing the number of detections (Abbott et al., 2016j). We therefore expect to continue exploring the science carried by these emissions with future GW-detectors, such as Cosmic Explorer and Einstein Telescope (Abbott et al., 2017a), (Punturo et al., 2010).

While ground-based interferometers are continuously updated with cutting-edge technologies, the challenge of building a space-based interferometer is also being investigated. Within this context, LISA (Laser Interferometer Space Antenna) is the leading project (Danzmann et al., 1996),(Audley et al., 2017). The designed sensitivity curve of this experiment is expected to cover the frequency range $10^{-4} Hz$ to 10^{-1} Hz. Experimental demonstrations of LISA feasibility were completed in 2017 by the LISA Pathfinder mission (Armano et al., 2016). However, the time scale for the first observations by a space based GW-detector is expected beyond 2028.

A completely different approach, which can potentially lead to a direct GW detection, is given by pulsar timing array (Foster and Backer, 1990). Pulsars are fast rotating NSs characterised by a strong beamed electromagnetic radiation. Pulsars are incredibly stable clocks, which can be perturbed by the presence of GWs. Thus by monitoring the correlations between the signals emitted by more pulsars it is possible to reveal and measure a background of GWs. Because of the required observation time ($t_{obs}^{PTA} \geqslant$ yr) the target GWs are characterised by very low fre-
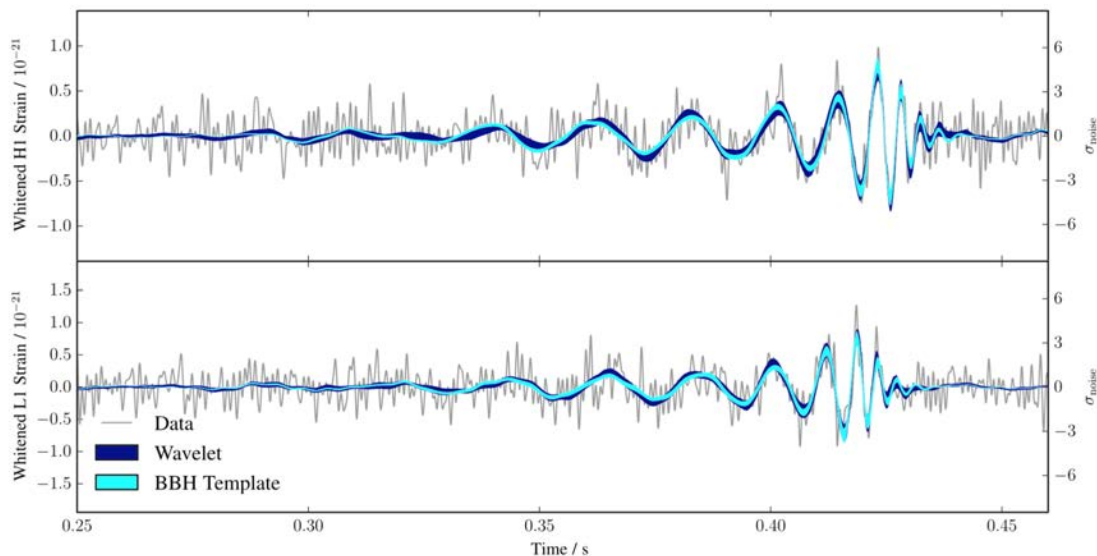
Figure 1.2: Time-domain data (sampled at 2048 Hz) and reconstructed waveforms of GW150914, whitened by the noise power spectral density, for the H1 (top) and L1 (bottom) detectors. Times are shown relative to September 14, 2015 at 09:50:45 UTC. The ordinate axes on the right are in units of noise standard deviations from zero, i.e., the peak alone is an $\sim 4\,\sigma$ excursion relative to the instrument noise at that time - and on the left are normalized in order to preserve the strain amplitude at 200 Hz. The waveforms are plotted as bands representing the uncertainty in the reconstruction. Shaded regions correspond to the 90% credible regions for the reconstructed waveforms. The broadest (dark blue) shaded region is obtained with the model that does not assume a particular waveform morphology, but instead uses a linear combination of sine-Gaussian wavelets. The lighter, narrower shaded region (cyan) is the result from the modeled analyses using two different template waveforms. The thin grey lines are the data. The agreement between the reconstructed waveforms using the two models is found to be $92^{+2}_{-3}\%$ (image from (Abbott et al., 2016f)).

quencies $(10^{-9} - 10^{-6})$ Hz. At this frequency range the most promising sources are the inspiralling of Super Massive Black-Holes (Jenet et al., 2005).

1.3   Gravitational-wave observations

On the 12th of September 2015, after about 5 years of upgrades, Advanced LIGO became operational, starting the first observing run of the second generation of GW-detectors. Only two days later, the era of GW astronomy began with the first GW direct detection, named after the date GW150914 (Abbott et al., 2016d) and whose data are reported in figure 1.2. This detection has been incredibly informative from several points of view. It proved the existence of binary black-holes, only theoreti-

cally predicted until that moment, as well as that these systems can merge within the age of the Universe (whose value is roughly the inverse of the Hubble constant $H_0 \sim 70$ km/s Mpc^{-1}). Analyses of the detected signal allowed us to determine the main parameters characterising the source of these GWs. They were generated about 1.3 billion years ago by two black-holes with respectively $m_1 \sim 39$ M$_\odot$ and $m_2 \sim 31$ M$_\odot$ (Abbott et al., 2016b). The two objects merged in a black-hole of ~ 68 M$_\odot$, freeing ~ 2 M$_\odot$ of energy in the form of GWs. At the time of the discovery, already the system components represented the most massive stellar black-holes ever observed. To date, the record of the most massive BH is still retained by the remnant resulted from this merger. Before GW detections, BH masses have been dynamically measured from observations of X-ray binaries. The majority of the discovered BHs have masses in the range $(5 - 10)$ M$_\odot$, however more massive BHs have also been claimed (Casares and Jonker, 2014), (Corral-Santana et al., 2016), (Tetarenko et al., 2016), (Prestwich et al., 2007), (Silverman and Filippenko, 2008). While the measurements of these latter are still debatable ((Laycock et al., 2015) and references therein), the first gravitational waves confirmed that such BHs as massive as 25 M$_\odot$ and more exist. Though the component masses of GW150914's source, together with the nearly unconstrained spins, do not allow inferences on the BBH formation channel, they imply consequences on the environment. Indeed the formation of such high mass black-holes requires low metallicity ($\leq 1/2$ solar) to prevent strong mass losses due stellar winds (Belczynski, K. and Bulik, T. and Fryer, C. L. and Ruiter, A. and Valsecchi, F. and Vink, J. S. and Hurley, J., 2010),(Spera, M. and Mapelli, M. and Bressan, A., 2015). Moreover the formation of BBHs constrains BH kicks to not always be > 100 km/s. If we assume evolution of an isolated binary as formation channel for the BBH, some population synthesis models/prescriptions, which predict no BBHs (such as e.g., (Nelemans et al., 2001), (Belczynski et al., 2002), (Mennekens and Vanbeveren, 2014), (Abbott et al., 2016a)), can already be rejected. GW150914 also allowed the first estimate of the rate of BBH mergers based on observations, which was constrained from several orders of magnitude

to $R_{BBH} = 2 - 400$ Gpc^{-3} yr^{-1} . This rate range, further limited by the successive GW detections, already suggested that LIGO will have soon detected further GWs. Observations met the expectations, with the detection of further 4 BBH coalescences; chronologically GW151226, GW170104, GW170608 and GW170814. An additional candidate of BBH coalescence LVT151012, likely of astrophysical origin, was also observed but with ranking statistics too low for a detection claim. BH masses inferred from GW signals are plotted against previous measurements from X-ray observations in figure 1.3. These merging binaries were detected during ~ 166 (~ 49 of O1 and ~ 117 of O2) days of LIGO coincidence data [3]. Although a revised rate estimate of BBH mergers, considering all observations, has not been published yet, these detections are consistent with the value obtained for the local universe ($z < 0.5$) from O1 events $R_{BBH} = 12 - 213$ Gpc^{-3} yr^{-1} (Abbott et al., 2017c).

According to many primordial black-hole models (such as (Rodriguez et al., 2016b),(Mapelli, 2016),(Stone et al., 2016),(Antonini et al., 2017), (Mandel and de Mink, 2016), (Hartwig et al., 2016), (Rodriguez et al., 2016a)), this rate range rules out the possibility of them being the only BBHs generating the observed GWs. However rate estimates are based on assumptions, whose uncertainties can considerably impact the rate value of merging BBHs. The LVC collaboration provides a range of rates which assumes two intrinsic mass distributions for each component in the black-hole binaries (Abbott et al., 2016b):

- two flat distributions in log;

- and a power law for the primary mass ($P(m_1) \propto m_1^{-2.35}$), combined with a flat distribution for the secondary.

The GW events detected up to now have not yet allowed a discrimination between different formation channels, though the spin distribution suggests that evolution of isolated binaries unlikely formed all the BBHs detected with GWs (Farr et al., 2017). Moreover aligned component spins limited at low positive values, as is the case of the source system of GW170104, argue against the standard scenario of

---

[3]Data collected while both the LIGO interferometers are correctly functioning.
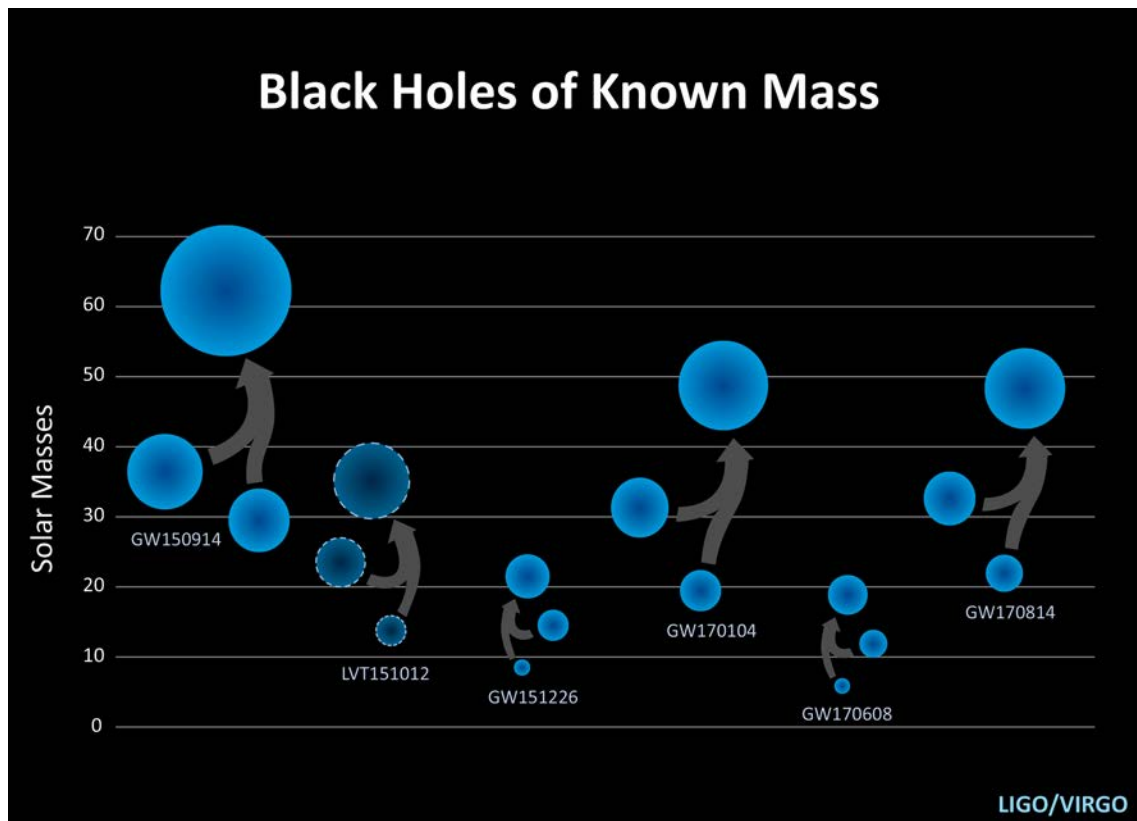
Figure 1.3: Black-holes discovered by LIGO. LIGO and Virgo have detected a range of black-holes. On the low-mass end, sources like the recently announced GW170608, and also GW151226, have masses comparable to those observed in X-ray binaries. The sources GW150914, GW170104, and GW170814 point to a higher-mass population that was not observed prior to these gravitational-wave detections. This figure also shows LVT151012, a LIGO candidate event that was too weak to be conclusively claimed as a detection. [Image credit: LIGO/Caltech/Sonoma State (Aurore Simonnet)] (LIGO Scientific Collaboration).

chemically homogeneous binary evolution. Environmental considerations can again be inferred from the component BH masses deduced from single GW events. For GW170104 and GW170814, as for GW150914, the high masses involved imply a likely formation of the compact objects in low-metallicity environments, unless the progenitors stars presented strong magnetic fields. Further detections will allow population studies which will help individualising the prominent BBH formation channels (Barrett et al., 2017) and hopefully disclose other astrophysical information carried by more exotic sources (such as eccentric binaries, intermediate mass BHs etc.). Moreover further detections will allow us to keep probing the theory of gravity, testing GR in strong and dynamic regimes, previously unexplored.

Since the second generation of ground-based interferometers has become operational, we not only detected the first gravitational-waves, but we also opened the era of multi-messenger astronomy (Abbott et al., 2017h). This happened with the first detection of gravitational-waves emitted during the merger of two neutron-stars (GW170817) (Abbott et al., 2017f), which occurred in temporal (with only ~ 1.7 s delay) and spatial coincidence with short Gamma-Ray burst (GRB) (GRB 170817A) (Abbott et al., 2017b). The availability of a 3-detector network determined a sky localisation for this event of ~ 30 deg^2 (Abbott et al., 2017f,h), which permitted an efficient follow up campaign. The sequent detection of the associated optical transient narrowed down the uncertainty on the source location to $\sim 1\%$ of an arc second squared, allowing observations covering most of the electromagnetic spectrum ((Abbott et al., 2017h) and references therein). Future detections of binary neutron-star (BNS) coalescences will help understanding the dynamic and the main physical processes leading to both electromagnetic and gravitational radiations (for further details section 5.1).

Chapter 2

Compact binary coalescences

Some of the materials constituting chapter 2 belongs to my Mid Course Assessment and master thesis.

2.1 Sources

In the previous chapter we show that any system, characterised by an evolving (non-null second derivatives) quadrupole moment of the mass distribution, generates GWs which propagate through the space-time. Practically, the weakness of the gravitational radiation limits our interest to only few astrophysical processes occurring within extreme physical conditions (Sathyaprakash, 2013). The detectability of an emitted GW mainly depends on the relation between the signal properties and the detector sensitivity. Choosing the class of instruments selects the spectral range of interest, determining the targeted sources. In this section we briefly present the nature of the GWs associated to the ground-based interferometers. Their typical spectral sensitivities span frequencies between few Hz and some kHz (Aasi et al., 2015a), (Acernese et al., 2014), allowing possible detections of a wide range of astrophysical phenomena, such as supernovae, coalescences of compact binaries, rotating NSs etc. (Thorne, 1987),(Schutz and Ricci, 2010), (Buonanno and Sathyaprakash, 2014), (Riles, 2013), (Sathyaprakash, 2013).

According to the characteristics of the target signals, the data acquired by these

instruments are analysed within four partially overlapping types of searches:

Compact Binary Coalescences (CBC): strong GWs are expected to be generated by the coalescences of two compact objects such as Black-Holes (BHs) and Neutron-Stars (NSs) (Postnov and Yungelson, 2014), (Flanagan and Hughes, 1998), citepLRR15. Searches dedicated in their detection and description are referred to with the same acronymous (see section 2.2 for more details). The signals emitted by these sources are sufficiently understood to allow template based searches, relying on match filtering techniques. However, in the last phase of their evolution, compact binaries enter in a highly relativistic regime, which require computationally expensive numerical relativity techniques to be solved (A. Buonanno et al., 2009).

Generic gravitational-wave transients (bursts): these signals are characterised by short life-times, typically from few ms to minutes. They are associated with very violent events happening in the universe such as supernovae explosions, CBCs and other unknown sources (Andersson et al., 2013). The analysis identifies time-correlated transients occurring in multiple interferometers. They rely on minimal assumptions, therefore allowing robust searches against uncertainties over GW sources, e.g. (Andersson et al., 2013);

Continuous-waves: these gravitational emissions are generated by rotating NSs and pulsars, characterised by non-completely spherical shapes, and present an almost constant frequency (Bildsten, 1998), (Prix, 2007). Detections of these waves are believed to be interrupted only by the life-time of the instruments. The main limitations on the correspondent searches are the weak predicted amplitudes of the signals and the high computational cost of the analysis;

Stochastic background: the GW background is expected to be generated by an incoherent superpositions of many GW signals (Allen, 1997), (Abbott et al., 2009b). Primordial GWs (Mandic et al., 2016) and cosmic string vibrations (Siemens et al., 2007) from the early universe, are among the most promis-

ing sources. However, the theoretical models of these source suffer of many uncertainties, which consequently affect the predicted GW amplitudes and detectability. Another possible contribution to the stochastic background is the overlap of many very distant BNS and BBH mergers (Evangelista and de Araujo, 2015), (Zhu et al., 2011).

This categorisation allows us to represent GW searches into a bidimensional plane, where one axis describes the waveform knowledge, and the other represents the signal duration in the sensitivity band (see fig. 2.1). As figure 2.1 shows, the most ex-
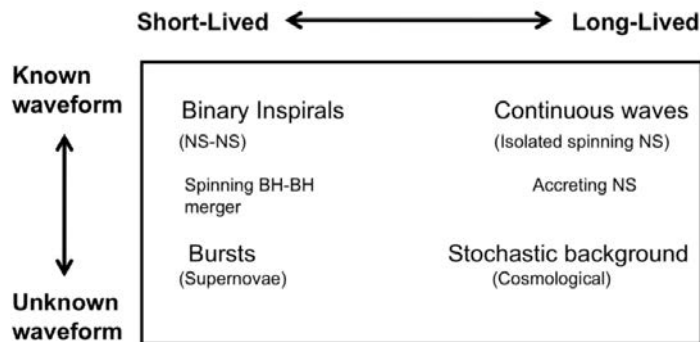
Figure 2.1: Schematic representation of GW searches as function of signal duration and knowledge of the waveform (Riles, 2013).

treme cases correspond to the gravitational emission generated by: two NS spiralling around each others, unspecified sources, spinning NSs and cosmological events.

2.2 Compact Binaries

One of the most promising sources of transient GWs are coalescing compact binaries, composed of NSs and/or BHs (Postnov and Yungelson, 2014) . Before the first GW detections, among these systems, only Binary NS (BNSs) (Faber and Rasio, 2012) were observed, while the existence of the Binary BH (BBHs) and systems composed of a NS and a BH were only supported by theoretical or indirect observational evidences. Binaries composed on a NS and a BH still remain unseen, while the existence of BBHs was confirmed with GW detections.

In the last few years, many different theoretical scenarios have been proposed to generate BBHs involving such massive objects. However the two most popular channels for the formation of such close compact binaries remain:

binary evolution in the galactic field (see (Tutukov and Yungelson, 1973), (Lipunov et al., 1997), (Belczynski et al., 2016a), (Belczynski et al., 2016b) and references therein): this scenario suggests the evolution of two massive stars in a binary orbit until the formation of a compact binary composed of BHs and /or NSs. Modelling the evolution of such systems involves the consideration of several stages still affected by many uncertainties, such as common envelope, SN kicks etc..., giving rise to a considerable spread over the predicted values of rates;

binary encounters in globular clusters (see (Sigurdsson and Hernquist, 1993), (Zwart and McMillan, 1999), (Rodriguez et al., 2015), (Rodriguez et al., 2016b) and references therein): this channel predicts the formation of compact binaries from dynamical interactions in dense stellar environments, such globular clusters.

Estimated rates of CBCs derived by these two formation channels span similar orders of magnitude (Abadie et al., 2010b). At the moment GW detections from BBHs do not allow us to distinguish between these two scenarios. However, assuming high BBH-spin magnitudes, as observationally supported (Miller and Miller, 2015), the spin distribution suggests that few of the detected BBHs were dynamically formed (Stevenson et al., 2017), (Farr et al., 2017).

GW detections allow to constrain CBCs intrinsic rates in the local Universe: the current estimates for BBH and BNS mergers are respectively $12-213\,\mathrm{Gpc}^{-3}\,\mathrm{yr}^{-1}$((Abbott et al., 2017d) and references there in) and $320-4740\,\mathrm{Gpc}^{-3}\,\mathrm{yr}^{-1}$ (Abbott et al., 2017g).

2.3 CBC emissions

Three different stages describe the dynamical evolution of compact binary coalescences: from the **inspiral**, where non-relativistic approximations can be applied, to the highly relativistic **merger** and **ringdown** (A. Buonanno et al., 2009), (Cutler and Flanagan, 1994).

2.3.1 Inspiral stage

The inspiral of the two bodies is the longest and a most understood evolutionary period of a merging binary. During this stage the lost of energy, due to the GW emission, implies a continuous decrease of the BH separation, correspondent to the increased orbital speed which establishes the known chirping behaviour. The inspiral starts when a compact binary is formed and evolves within a non-relativistic regime from low frequencies until the Innermost Stable Circular Orbit (ISCO) is reached. This condition represents the formal beginning of the merger; from this moment relativistic effects must be taken into account to accurately describe the system. In GR, the ISCO frequency is defined for a non-spinning BBH (Lai and Wiseman, 1996) as:

$$f_{ISCO}^{orb} = \sqrt{\frac{MG}{4\pi R_{ISCO}^3}} = \frac{1}{12\sqrt{6}\pi}\frac{c^3}{GM} \tag{2.1}$$

where $R_{ISCO} = 3R_S = \frac{6GM}{c^2}$ is the separation between the two compact objects. This relation shows that the more massive a system, the lower the orbital frequency at ISCO. The 1 to 1 correspondence between time evolution and orbital frequency implies that signals characterised by lower frequency ISCO cross the sensitivity band of the interferometers for a shorter period. Because the coalescence of a compact binary generates a GW whose frequency is twice the orbital one, f_{ISCO}^{orb} corresponds to $f_{ISCO}^{GW} = \frac{c^3}{6^{3/2}\pi GM}$. The dynamical evolution of a compact binary, while the companions spiral toward each other, is usually analytically described by adopting post-Newtonian approximations (A. Buonanno et al., 2009). At the lowest and dominant

order, the two waveform polarisations, generated by non-spinning companions moving on quasi-circular orbits, are observed as:

$$
\begin{aligned}
h_+(t) &= 4\frac{G^{5/3}}{c^4}\frac{\mathcal{M}^{5/3}}{D_L}\left(\frac{1+\cos^2\iota}{2}\right)\omega(t|t_c,\mathcal{M},q)^{2/3}\cos\left(2\phi(t;t_c,\mathcal{M},q)+\phi_c\right)\\
h_\times(t) &= 4\frac{G^{5/3}}{c^4}\frac{\mathcal{M}^{5/3}}{D_L}\cos\iota\,\omega(t|t_c,\mathcal{M},q)^{2/3}\sin\left(2\phi(t;t_c,\mathcal{M},q)+\phi_c\right)
\end{aligned}
\tag{2.2}
$$

where $\mathcal{M} = (m_1\,m_2)^{3/5}/(m_1+m_2)^{1/5}$ is the chirp-mass, q is ratio between the two component masses, D_L is the luminosity distance between source and observer, ι the inclination angle of the binary respect the line of sight, t_c the time of collision, ϕ_c the correspondent phase and the ";" in ϕ and ω separates the time dependence, which evolves $h_{+/\times}$, from the other parameters uniquely fixed for each source ((Punturo et al., 2011), pp 29).

This stage is also characterised by a peculiar frequency evolution (Cutler and Flanagan, 1994), given by the equation:

$$
f(t) = \left[\frac{256}{5}\frac{G^{5/3}\mathcal{M}^{5/3}\pi^{8/3}}{c^5}(t_c-t)\right]^{-3/8}
\tag{2.3}
$$

2.3.2   Merger

The binary progressively evolves towards a relativistic regime, where the velocities involved reach a considerable fraction of c and the distance between the two compact objects becomes comparable to their radii. (Flanagan and Hughes, 1998) Dynamical instabilities start to take place and the bodies undergo a freely-falling plunge which drives the system to the final collision, independently of gravitational radiation emitted during this stage. This phase and the actual collision define the merger. Because the merger takes place in a strong relativistic regime and the Einstein equations cannot be linearised, the involved processes are not yet perfectly understood. However numerical relativistic techniques have been developed to describe this stage and the related gravitational emission. GW detections of a CBC mergers can potentially constrain the uncertainties of the physics and dynamics behind such processes.

Current studies suggest that the observed events are consistent with the predictions of GR (Abbott et al., 2016b),(Abbott et al., 2017d).

2.3.3   Postmerger

The final collision of compact binaries generates a new object, which, at the end, stabilises into a NS or a BH (for more details see 5), according to the masses involved and the unknown equation of state, in the case of BNS mergers. When two BHs coalesce, the post-merger phase is also referred as *ringdown*. At the beginning the newly born body is strongly deformed and, after a very quick phase characterised by gravitational emissions, it eventually settles down to a stationary state. The GW associated to this binary stage can be modelled by perturbative theories. They predict waveforms composed of a superposition of quasi-normal modes, identified by their overtone n and their spheroidal harmonic indices l and m. These modes can be represented by damped sinusoids, defined by a complex angular frequency $w_{(l,m,n)} = 2\pi f_{(l,m,n)} - i/\tau_{(l,m,n)}$ whose real part describes the oscillation $f_{(l,m,n)}$ and the imaginary one is the inverse of the damping period $\tau_{(l,m,n)}$ (Buonanno et al., 2007). The dominant mode is expected to be defined by $n = 0$ and $m = l = 2$ (bar-mode).

Chapter 3

Parameter estimation with multi-banding

In this chapter we present the implementation of an efficient sampling technique to accelerate the standard analysis of `LALInference`, the LSC Algorithm Library dedicated to the inference of the parameters which describe GWs emitted during Compact Binary Coalescences (CBCs) (section 3.3).

In section 3.1, we briefly introduce the basis of parameter estimation (PE) analyses, including data and waveform models. We then outline the correspondent computational challenges and motivations in section 3.2. In particular, we focus on the impact of the increased amount of data for future GW-detectors and some alternative procedures dedicated to accelerate the analysis of CBC signals.

Part of the introductory material of this chapter replicates the content of my Mid Course Assessment. Section 3.3 reproduces the text of (Vinciguerra et al., 2017b), published on the journal Classical and Quantum Gravity. The overall project has been presented to the European Commission for financing my PhD position in the GraWIToN ITN by Ilya Mandel in collaboration with John Veitch. The design and its concrete implementation was the result of the conjunct efforts of all the authors. I led code implementation and tests, supported in debugging, editing and developing by John Veitch. The code dedicated in testing the speed of particular part

of `LALInference` *code was written by John Veitch. I produced all the plots presented in the paper, while the text was written by myself in collaboration with John Veitch with modifications by Ilya Mandel.*

3.1   Parameter estimation

In the previous chapter, we present some of the main features which characterise GWs emitted by coalescences of compact binaries. Here we are interesting in understanding the information carried by GWs and how to effectively extract them from the data (for more details see e.g. (Cutler and Flanagan, 1994),(Veitch et al., 2015a)).

In the past years many efforts have focused on improving the detection algorithms to optimise the signal recognition inside very noisy data. For well modelled signals, such as the ones generated by standard CBCs, the most effective searches are addressed by matched filtering techniques. The main astrophysical parameters carried by these waveforms are masses, spin and distance of the merging binaries. The inference of these quantities is among the fundamental challenges of CBC studies. The natural framework for inferring these parameters is provided by Bayesian analyses.

3.1.1   Bayesian Analysis

The main scientific goal of GW analysis is to extract as much astrophysical information as possible from the data. Gravitational signals generated by CBCs are determined by several physical parameters $\boldsymbol{\theta} \equiv \{\theta_0, ..\theta_i, ..., \theta_n\}$, which are commonly estimated within a Bayesian framework. According to Bayesian theory, they can be deduced from the data $\mathbf{d}$ in form of posterior distributions $p(\boldsymbol{\theta}|\mathbf{d}, H)$ by applying the Bayes' theorem:

$$p(\boldsymbol{\theta}|\mathbf{d}, H) = \frac{p(\boldsymbol{\theta}|H)p(\mathbf{d}|\boldsymbol{\theta}, H)}{p(\mathbf{d}|H)} \tag{3.1}$$

Here:

- $p(\boldsymbol{\theta}|H)$ is the *prior probability* on the set of parameters $\boldsymbol{\theta}$, given the model H;

- $p(\mathbf{d}|\boldsymbol{\theta}, H)$ is the *likelihood* of obtaining the data $\mathbf{d}$ assuming H and $\boldsymbol{\theta}$;

- $p(\mathbf{d}|H)$ is the *evidence*, the normalisation factor defined by the following integral over the parameter space Θ:

$$Z = p(\mathbf{d}|H) = \int_{\Theta} p(\mathbf{d}|\boldsymbol{\theta}, H)p(\boldsymbol{\theta}|H)\, d\boldsymbol{\theta} \tag{3.2}$$

The posterior of each individual parameter is then obtained integrating the $p(\boldsymbol{\theta}|\mathbf{d}, H)$ over all the other physical quantities (*marginalisation*).

$$p(\theta_i|\mathbf{d}, H) = \int_{\bar{\boldsymbol{\Theta}}_i} p(\boldsymbol{\theta}|\mathbf{d}, H)\, d\bar{\boldsymbol{\theta}}_i \tag{3.3}$$

where with $\bar{\boldsymbol{\theta}}_i$ we indicate the set of parameters complementary to θ_i ($\bar{\boldsymbol{\theta}}_i = \theta_0, ..\theta_{i-1}, \theta_{i+1}.., \theta_n$) and with $\bar{\boldsymbol{\Theta}}_i$ the related parameter space. With the resulting posterior distributions, it is then possible to calculate statistical properties associated to the quantities of interest.

Adopting the Bayes' theorem, we can estimate the posterior probability of a given set of $\boldsymbol{\theta}$ combining our a priori knowledge (the priors) with the likelihood, normalised to the evidence.

In the following section we outline data (section 3.1.2) and waveform (section 3.1.3) models, adopted within the just described Bayesian analysis, for estimating the parameters of GWs emitted by CBCs.

3.1.2 Data model

The *likelihood* transfers the information carried by the data into our estimation of the parameter posterior probability density functions (PDFs). The likelihood aims to quantify the correlation between data $\mathbf{d}$ and an hypothesised GW emission $\mathbf{h}(\boldsymbol{\theta})$. This is the projection of the two waveform polarisations ($\mathbf{h}_{\times}$ and $\mathbf{h}_{+}$) over the instrument network sensitivity, represented by the two antenna patterns $F_{\times}$ and

F_+: $\mathbf{h}(\boldsymbol{\theta}) = F_\times(\boldsymbol{\theta_{ex}})\mathbf{h}_\times(\boldsymbol{\theta}) + F_+(\boldsymbol{\theta_{ex}})\mathbf{h}_+(\boldsymbol{\theta})$, where $\boldsymbol{\theta_{ex}}$ are the external parameters which only depend on source position relative to the detector location. Because of the Earth rotation, such functions are formally time dependent, but for signals characterised by short in-band durations, such as transients generated in CBCs, this dependence can be neglected. However techniques to account for such variability are currently under investigations, in view of future generations of GW-detectors. The analysis is then carried out by representing the data as:

$$\mathbf{d} = \mathbf{n} + \mathbf{h} \tag{3.4}$$

where $\mathbf{n}$ is the noise realisation. The noise is assumed to be a stationary Gaussian process, with zero-mean and known variance. The latter is estimated from the power spectrum of the GW-detector noise.Although real noise is far from being Gaussian and stationary, (Berry et al., 2015) conclude that, in average, this does not compromise parameter estimation analyses based on templates. Under the hypothesis of pure noise realisation H_n, which implies $\mathbf{d} = \mathbf{n}$, this model predicts that the measured data occur with probability:

$$p(\tilde{\mathbf{d}}|H_n, \mathbf{S_n}) = \left(\prod_i \sqrt{\frac{\delta f}{\pi S_n(f_i)}} \right) e^{\sum_i \left[\frac{-2|\tilde{d}(f_i)|^2}{S_n(f_i)} \delta f \right]} \tag{3.5}$$

where δf is the sampling step in the frequency domain and $S_n(f)$ the one-sided power spectral density of a single detector. Because the likelihood is evaluated in frequency domain, the data are Fourier transformed into $\tilde{\mathbf{d}}(f)$.

To infer the astrophysical parameters in the case of signal presence (H_{n+h}), we quantify how likely it is that the data contain a particular waveform, by evaluating the following expression:

$$p(\tilde{\mathbf{d}}|H_{h+n}, \boldsymbol{\theta}, \mathbf{S_n}) = \left(\prod_i \sqrt{\frac{\delta f}{\pi S_n(f_i)}} \right) e^{\sum_i \left[-\frac{2|\tilde{d}(f_i) - \tilde{h}(\boldsymbol{\theta}, f_i)|^2}{S_n(f_i)} \delta f \right]} \tag{3.6}$$

where $\tilde{\mathbf{h}}(\boldsymbol{\theta})$ is the signal strain in frequency domain. This can be obtained merging the antenna patterns with frequency-defined models or with Fourier transformations of time-domain waveforms. Since independent from both model $\tilde{h}(\boldsymbol{\theta}, f_i)$ and data $\tilde{d}(f_i)$, the multiplication factor enclosed in the brackets of equations 3.5 and 3.6 is irrelevant for the PE analyses. We therefore need to calculate only the exponent of the previous expression (3.6), the *log-likelihood*. It is a common approach to express this quantity in terms of the following inner product:

$$\langle a|b \rangle = 2 \int_0^\infty \frac{\tilde{a}(f)\tilde{b}^*(f) + \tilde{a}^*(f)\tilde{b}(f)}{S_n(f)} \, df \tag{3.7}$$

The Bayesian data-analysis is therefore led by the estimation of:

$$\log p(\tilde{\mathbf{d}}|H_{n+h}, \boldsymbol{\theta}, \mathbf{S_n}) \propto -\frac{1}{2} \langle h(\boldsymbol{\theta}) - d|h(\boldsymbol{\theta}) - d \rangle$$
$$\propto -\frac{1}{2} \left[\langle h|h \rangle - 2\Re\{\langle h|d \rangle\} + \langle d|d \rangle \right] \tag{3.8}$$

where

$$\langle d - h|d - h \rangle = 4 \int_0^\infty \frac{|\tilde{d}(f) - \tilde{h}(\boldsymbol{\theta}, f)|^2}{S_n(f)} \, df$$
$$\approx 4\delta f \sum_{i=0}^N \frac{|\tilde{d}(f_i) - \tilde{h}(\boldsymbol{\theta}, f_i)|^2}{S_n(f_i)} \tag{3.9}$$

and $\Re\{\langle h|d \rangle\}$ is the real part of the inner product $\{\langle h|d \rangle\}$. The last line of equation (3.9) represents a common numerical estimation of $\langle d - h|d - h \rangle$.

To analyse data recorded by a network of interferometers $\mathbf{d_D}$, we further assume the noise to be uncorrelated between different instruments. This conjecture allows us to define the network likelihood with a product of the single detector (D_i) likelihoods:

$$p(\tilde{\mathbf{d}}_{\mathbf{D}}|H_{n+h}, \boldsymbol{\theta}, \mathbf{S_{nD}}) = \prod_{D_i \in \mathbf{D}} p(\tilde{\mathbf{d}}_{D_i}|\boldsymbol{\theta}, H_{n+h}) \tag{3.10}$$

3.1.3   Waveform models

Several studies are dedicated to accurately modelling the gravitational emission generated by CBCs (see for example (Blackman et al., 2017), (Pannarale et al., 2015) and (Barkett et al., 2016)). Different approximations can be adopted to represent the inspiral and the ringdown stages. Numerical relativistic techniques are instead used to represent the merger and to calibrate the whole simulated gravitational emission. Nowadays a rich variety of waveform families is available (A. Buonanno et al., 2009). They differ from each other in theoretical assumptions, approximations and regime of validity. They can also considerably differ in the description accuracy and in the computational cost: often the most precise waveforms are also the most computationally expensive. Given the parameters of a binary $\boldsymbol{\theta}$, these theoretical predictions determine the vectors $h_+(\boldsymbol{\theta}, t)$, $h_\times(\boldsymbol{\theta}, t)$ or $h_+(\boldsymbol{\theta}, f)$, $h_\times(\boldsymbol{\theta}, f)$ depending on weather the adopted model is developed in time or frequency domain.

At least 9 parameters are necessary to accurately describe GWs generated by the coalescences of two compact objects:

Masses [2]: m_1 and m_2 are the masses of the binary components, the common convention is $m_1 \geq m_2$. However, depending on the signal, other parameterisations might be used: in particular the mass combination *chirp-mass* $\mathcal{M} = (m_1 \cdot m_2)^{3/5}(m_1 + m_2)^{1/5}$ sets the first order inspiral dependence on the masses of the system. Usually, once adopted $\mathcal{M}$, the second term mass is the *mass-ratio*, which can be defined as:

    $\star$ asymmetric mass-ratio q: $q = m_2/m_1$, with $q \in 0, 1]$;

    $\star$ symmetric mass-ratio $\eta = (m_1 * m_2)(m_1 + m_2)^{-2}$;

Sky localisation [2]: δ is the declination and α is the right ascension relative to the source position;

Distance [1]: D_L is the luminous distance of the source;

Inclination [1]: θ_{JN} is the generalised angle between the total angular momentum and the line of sight. For non-spinning and aligned systems the angular

momentum points in the same direction of the total angular momentum, and therefore $\theta_{JN} = \iota$, where ι is the angle between the orbital angular momentum and the line of sight;

Polarisation [1]: Ψ represents the polarisation angle, the rotation around the line of sight of the orbital angular momentum;

Coalescence [2]: t_c is the arbitrary absolute time at which the collision of the binary is estimated to occur and ϕ_c is the value of the waveform phase at the same instant t_c.

These are the basic physical quantities required to describe the coalescence of **non-spinning** bodies moving on **circular orbits**. Including the two spin vectors $\mathbf{S}_i$ in the waveform model implies adding further 6 parameters:

Amplitudes [2]: a_i usually parametrised as function of the component masses, as follows: $a_i = cS_i/(Gm_i^2)$

Orientations [4]: described by two angles for each $\mathbf{S}_i$.

These can be reduced to the 2 spin amplitudes, assuming aligned or anti-aligned configurations. Further parameters should be introduced to adequately represent sources described by more elaborated physical models. They could for example include eccentricity of the binaries, deviations from GR and matter effects in systems involving NSs.

3.2   Computational challenge

The main task of the project consists in reducing the computational cost, and consequently the run-time, required to perform Bayesian analyses dedicated to the estimation of the parameters which characterise GWs emitted during CBCs. In this section we outline the computational issues related to these estimates, motivating the urge of development and implementation of new and general techniques, aimed

in accelerating these inferences.

Despite the simplicity of the formulation, performing a full Bayesian analysis is often computationally challenging. This has made these techniques effectively available only during the last few years, with the increased availability of computer power. The high computational demand can be traced back to: (i) high dimensions of the parameter space, (ii) complexity of the posterior distributions, and (iii) recurrent estimates of quantities which require long calculations, such likelihood and models. In the context of GW studies, the high computational cost is due the dimension of $\boldsymbol{\theta}$ and the correspondent (usually) wide priors, which challenge the investigation of parameter space. To mitigate this issue, stochastic techniques based on Markov chain Monte Carlo (MCMC) and nested sampling are now commonly adopted in GW studies. Despite the efficiency of such techniques, the complexity of the model and the amount of data to be analysed, make their implementation computationally expensive and time demanding, even when combined with parallel tempering methods. Indeed usually Bayesian inferences require $\sim 10^6$ proposed jumps in the parameter space; each of these selected set of parameters $\boldsymbol{\theta}$ is then evaluated with the calculation of the likelihood (3.6). For CBC studies based on match filtering techniques, the evaluation of such function represents one of the main computational issues of the whole analysis, as it includes (i) generating waveforms $\tilde{h}(\boldsymbol{\theta}, f)$ (or $h(\boldsymbol{\theta}, t)$ and correspondent Fourier transform), and (ii) the actual numerical integration of the inner product of eq. (3.9). The inner product is indeed calculated with a sum over N terms, correspondent to the number of Fourier components, necessary to correctly represent a gravitational signal. To avoid aliasing in the signal, the frequency step δf_0 needs to be smaller that the inverse of the longest signal duration allowed by the search. N is therefore set by the frequency range and δf_0:

$$N = int[(f_{max} - f_{min})/\delta f_0] \tag{3.11}$$

and determines the computational demand of the likelihood evaluation, considerably affecting the time required by the whole Bayesian analysis. Decreasing the

delay between data-achievement and PDF construction means also extending the applicability of this approach to bigger volumes of the parameter space and larger amount of data, such as the one expected from future generation of GW-detectors.

3.2.1 Sensitivities of Future Generations

Among the several upgrades planned for the next generations of GW-detectors, the improvement in the lower frequency range has a major impact for CBC studies. Indeed, given a compact binary, a better sensitivity at lower frequencies implies a higher number of cycles in the instrument band. This deeply affects the analysis of CBC, especially for low-mass systems, such as the detected Binary Neutron-Star (BNS) merger (Abbott et al., 2017g). In particular a GW signal in a frequency range $[f_{min}, f_{max}]$ (with $f_{max} \gg f_{min}$) will approximatively last:

$$T = t(f_{max}) - t(f_{min}) \approx 5c^5 \left[8\pi \left(f_{min} \right) \right]^{-8/3} \left(G\mathcal{M} \right)^{-5/3} \tag{3.12}$$

For emissions generated by CBCs, f_{min} is usually set by the sensitivity band, while f_{max} is limited by the maximum frequency contained in the GW (f_{ISCO} if we are interested to the only Inspiral). We therefore expect that the noise reduction in the low-frequency range (from $f_{min} \sim 40Hz$ of initial LIGO to $f_{min} \leq 15Hz$ of aLIGO at designed sensitivity and finally to $f_{min} \leq 5Hz$ for Einstein Telescope) will considerably increase the duration of CBC detections. The availability of longer signals will increase the accumulated Signal-to-Noise Ration (SNR):

$$SNR^2(f) = 4 \int_0^f \frac{|\tilde{h}(f')|^2}{S_n(f')} \, df' \approx 4 \int_{f_{min}}^f \frac{|\tilde{h}(f')|^2}{S_n(f')} \, df' \tag{3.13}$$

Extended durations of the detected gravitational emissions are thus expected to significantly improve the parameter estimation results, providing more reliable astrophysical information. The bottleneck of this improvement consists in the substantial increase of the amount of data which needs to be analysed. The data are divided in segments of constant period T_{seg}. To avoid lost of information or signal distortions:

$$T_{seg} \geq max_{\boldsymbol{\theta} \in \boldsymbol{\Theta}} T(\boldsymbol{\theta}) \approx max_{(f_{min}, \mathcal{M}) \in \boldsymbol{\Theta}} T(f_{min}, \mathcal{M}) \tag{3.14}$$

where $\boldsymbol{\Theta}$ is the parameter space of interest. According to equation (3.12), the duration of the longest GWs is substantially set by the lower frequency limit f_{min} and the chirp-mass $\mathcal{M}$. f_{min} is set by the limitations of the instrument sensitivity, while the chirp-mass value $\mathcal{M}$, which maximises the in-band signal, consists in the lightest system included in the target sources (given a fixed mass-ratio, the chirp-mass is indeed a monotonic function of the total mass of the binary).

Because of the mass dependence of relation (3.12), the extension of the sensitivity band to lower frequencies is going to particularly affect the analysis of low-mass systems. The in-band duration of signals emitted by BNSs are thus expected to increase by orders of magnitude, passing from typical duration of *seconds* for the initial LIGO configuration to *minutes* for aLIGO and *days* for the Einstein Telescope (see fig. 3.1). Detections of GWs generated by such light binaries are largely dominated by the inspiral stage, whose duration substantially sets the correspondent amount of data. The bottleneck of these improvements, and the consequently increased SNR, is going to be the considerable growth of the computational time required to perform a complete parameter estimation. Indeed the number N, which leads the likelihood cost, is going to increase by a factor $N \propto n_0^{8/3}$, assuming n_0 to be the improvement on the lower frequency limit f_{min}: $f_{min}^{new} = f_{min}^{old}/n_0$.

It is this expected increase in computational time which motivates the investigations of faster parameter estimation procedures. The most successful approaches are briefly summarised in the following.

3.2.2 Solution Proposed

Studies of CBC signals require a large set of filter templates. The correspondent points in the parameter space are chosen to avoid a loss of the SNR greater than a
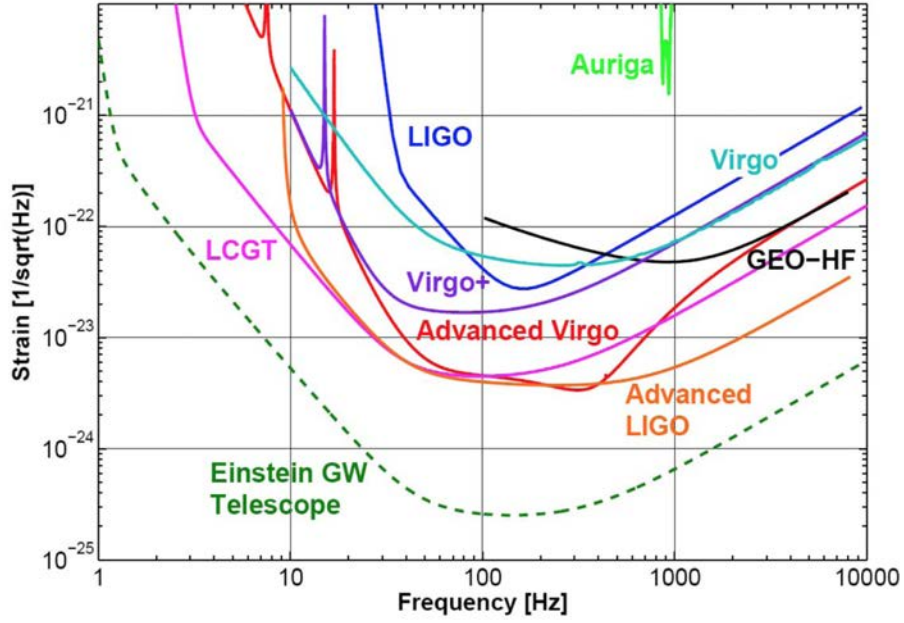
Figure 3.1: Comparison between the sensitivity curves for past, present and future generations of ground-base detectors (Hild, 2012).

given threshold. The very low value of such threshold implies considerable overlaps between waveforms neighbour in the parameter space. By adopting Singular Value Decomposition (SVD), it is possible to reduce the number of templates necessary for the investigation by building an orthogonal basis. This technique is successfully implemented in pipelines devoted to detection searches (e.g. (Cannon et al., 2010), (Cannon et al., 2012b), (Cannon et al., 2013), (Cannon et al., 2012a; Canizares et al., 2015a)).

Another approach proposed for accelerating parameter estimation consists in developing Reduced-Order-Modeling (ROM) (Pürrer, 2014), (Canizares et al., 2015b). The main idea is to define a reduced basis $B(f)$ through which it is possible to effectively span the whole parameter space. Under this approach any $\tilde{h}_{ROM}(\boldsymbol{\theta}, f)$ can be represented by:

$$\tilde{h}_{ROM}(\boldsymbol{\theta}, f) = e^{-i2\pi t_c f} \sum_{i=1}^{M'} c_i(\boldsymbol{\theta}) B_i(f) \tag{3.15}$$

where the waveforms belonging to the basis are selected by applying the *reduced basis method* and the coefficient $c_i(\boldsymbol{\theta})$ are calculated using an *empirical interpolation method* (Barrault et al., 2004).

Finally the analysis can also take advantage of a *reduced order quadrature* (ROQ) (Canizares et al., 2013) equivalent to the inner-product:

$$\langle d|h(\boldsymbol{\theta})\rangle = 4\delta f \sum_{k=1}^{N} \frac{\tilde{d}(f_k)\tilde{h}^*(\boldsymbol{\theta}, f_k)}{S_n(f_k)} \tag{3.16}$$

since this is the only part of the likelihood, as shown by equation (3.8), dependent on both the data and the template and that therefore needs to be computed online for any choice of the parameter set $\boldsymbol{\theta}$.

3.3 Accelerating gravitational-wave parameter estimation with multi-band template interpolation

Parameter estimation on gravitational-wave signals from compact binary coalescence (CBC) requires the evaluation of computationally intensive waveform models, typically the bottleneck in the analysis. This cost will increase further as low frequency sensitivity in later second and third generation detectors motivates the use of longer waveforms.

We describe a method for accelerating parameter estimation by exploiting the chirping behaviour of the signals to sample the waveform sparsely for portions where the full frequency resolution is not required. We demonstrate that the method can reproduce the original results with a waveform mismatch of $\leq 5 \times 10^{-7}$, but with a waveform generation cost up to ~ 50 times lower (compared to the case of constant frequency resolution) for computationally costly frequency-domain waveforms starting from below $8\,\mathrm{Hz}$.

3.3.1   Introduction

The discovery of gravitational-waves from coalescing Binary Black-Hole (BBH) systems made by Advanced LIGO in its first observing run opened the door to gravitational-wave astronomy (Abbott et al., 2016d). As the second generation of ground based detectors continues to evolve towards their design sensitivities the rate of detections is expected to increase, leading eventually to the detection of lower mass binary systems such as Binary Neutron-Star (BNS) and Neutron-Star - Black-Hole (NSBH) binaries (Abadie et al., 2010b).

The characterisation of these sources involves the use of Bayesian parameter estimation and model selection algorithms based on stochastic sampling of the posterior probability distribution for the model parameters conditioned on the observed data. This process involves repeated comparisons of the data with template waveforms through evaluation of the likelihood function. Previous implementations (e.g. `LAL-Inference` (Veitch et al., 2015b)) have required millions of likelihood evaluations, which implies that a similar number of template waveforms must be generated. In the case of sophisticated waveform models this template generation dominates the computational cost of the analysis, with the cost scaling linearly with the length of the waveform τ, which in turn scales with the low frequency starting point of the waveform as $f_{\min}^{-8/3}$. As the low-frequency sensitivity of the second-generation instruments improves, $f_{\min}$ is expected to reduce from $\sim 30\,\mathrm{Hz}$ to $\sim 10\,\mathrm{Hz}$ or lower. The issue becomes even greater in the case of subterranean third-generation instruments such as the Einstein Telescope which are expected to reduce this further to $5\,\mathrm{Hz}$ or lower (Punturo et al., 2011, 2010). This improvement in low-frequency sensitivity should translate to much more accurate estimation of key parameters. However, taking full advantage of this improvement in a timely and computationally efficient manner is a challenge. We present a method that leverages the frequency evolution of the waveform to effectively reduce the number of waveform samples that must be computed. This has the potential to asymptotically reduce the computational cost of template generation by a factor that is proportional to $f_{\min}^{-1}$. Here we give details

of a practical implementation which does not compromise the accuracy of parameter estimation and study the computational cost scaling in a realistic analysis.

Several methods have been developed previously to overcome the need to evaluate the waveform and likelihood at each point in the Fourier domain.

Reduced order quadrature (ROQ) methods, first introduced for CBC waveforms in (Field et al., 2011) and developed for the purpose of parameter estimation (PE) in (Canizares et al., 2013; Smith et al., 2013; Canizares et al., 2015a; Smith et al., 2016), seek to represent the waveform in an alternative basis from the standard Fourier components. A waveform for a particular point in parameter space is represented as the linear combination of a number of these basis templates. By projecting the data into the same basis the likelihood function can be computed using a sum over bases rather than a sum over Fourier components, where the number of bases is far smaller than the number of Fourier components. This method significantly accelerates the likelihood computation. However, it has the drawback of requiring the basis to be constructed in advance for each waveform family, a process which is costly in terms of both computation and memory requirements to store the input waveforms, with a cost that grows rapidly as the dimensionality of the model is increased to include misaligned spins. The large intrinsic volume of the mass parameter space requires that it be subdivided into patches of manageable size, with each patch having a different set of bases. The ROQ likelihood calculation is also dependent on the particular noise curve used through the ROQ integration weights, which must be computed for the particular characteristics of the data at the time of the event of interest. Furthermore, severing the link between frequency and the representation of the waveform makes it difficult to model the effect of frequency-dependent detector calibration errors, which were included in the analysis of BBH systems in O1 (Abbott et al., 2016f,b).

A different approach has been developed in the context of low-latency searches for gravitational-waves. In this context the incoming data-stream is filtered against a pre-determined bank of templates which is chosen to cover the mass parameter space

with a certain maximum guaranteed loss of signal-to-noise ratio (SNR). Although here the filtering can proceed in parallel it is still desirable to reduce the cost of the search by reducing the volume of data that has to be processed. The MBTA (Abadie et al., 2012c; Adams et al., 2016) and gstlal (Cannon et al., 2012a) pipelines divide the templates into bands, which are chosen to exploit the chirping nature of the inspiral signal. Each band has a certain maximum signal frequency $f < f_{\max}$, so both the template and the data can be down-sampled to a lower sampling rate, reducing the cost of the filtering process for each band. The original high-bandwidth SNR time-series can be reconstructed from the output of the banded filters by subsequent up-sampling, which can be done selectively on data stretches which have significant SNR in the banded filters. A similar approach has been advocated for LISA data analysis, employing two bands for each template (Porter, 2014), as is also the case for MBTA.

In this paper we pursue an approach inspired by the latter method of subdividing the waveform into band-limited pieces, with the aim of using it for PE rather than searching. This places some additional constraints on the accuracy of waveform reconstruction required to reproduce the results from a full-bandwidth analysis without adding systematic or statistical errors. Our method is currently limited to the computation of the template (likelihood evaluation is still performed in the full Fourier basis), but nevertheless can produce large reductions in computational cost for long duration signals when the more sophisticated (and costly) waveform models are employed. Unlike the ROQ, this allows us to maintain the link with frequency and easily include calibration error modelling in the analysis. Also, because the method requires no pre-computation of a new basis it can be applied without modification to any frequency-domain waveform model, including modifications to the signal such as tidal effects (Vines et al., 2011; Hinderer et al., 2016) and parameterised deviations from general relativity (Abbott et al., 2016h; Agathos et al., 2014). This flexibility is the main advantage of the method, which makes it especially suitable for analyses where an ROQ model is not available, or where its production

would be too costly. An implementation is provided in the open source `LALInfer-ence` PE software (Veitch et al., 2015b). We describe the method in detail in section 3.3.2 and demonstrate its efficacy when applied to the analysis of simulated signals in section 3.3.3. We discuss possible future developments in section 3.3.4.

3.3.2 Multi-banding approach: the method

Motivation

In gravitational-wave PE, the aim is to explore the posterior probability distribution of the source model,

$$p(\vec{\theta}|\vec{d}, H) = \frac{p(\vec{\theta}|H)p(\vec{d}|\vec{\theta}, H)}{p(\vec{d}|H)} \qquad (3.17)$$

where $\vec{\theta}$ are the physical parameters of the source such as the masses, spins, position and orientation (Veitch et al., 2015b). The likelihood function for a single detector under the assumption of Gaussian noise depends on the data $\vec{d}$ and the parameter $\vec{\theta}$, as well as the particular waveform model used H, as

$$p(\vec{d}|\vec{\theta}, H) \propto \exp\left[-2\sum_i^N \frac{|h_i(\vec{\theta}) - \vec{d}_i|^2}{\tau S_n(f_i)}\right] \qquad (3.18)$$

where $S_n(f_i)$ is the power spectral density of the detector, $\tau = \delta f^{-1}$ is the duration of the data segment to be analysed, and $N = \tau/(2\delta t)$ is the number of Fourier components in the frequency-domain complex representation of the modeled signal $h_i(\vec{\theta})$ as it would be observed in the detector. Since the details of the detector responses are not important for what follows we refer the reader to (Veitch et al., 2015b) for a full description of how the extrinsic parameters are used to construct the observed signal in each detector. In order to accurately capture the waveform we must choose τ and δt such that the entire signal duration, from the time it enters the sensitive band of the instrument at frequency $f_{\min}$, is contained in τ, and the sampling resolution $\delta t < (2f_{\max})^{-1}$ is sufficient to capture the highest frequency
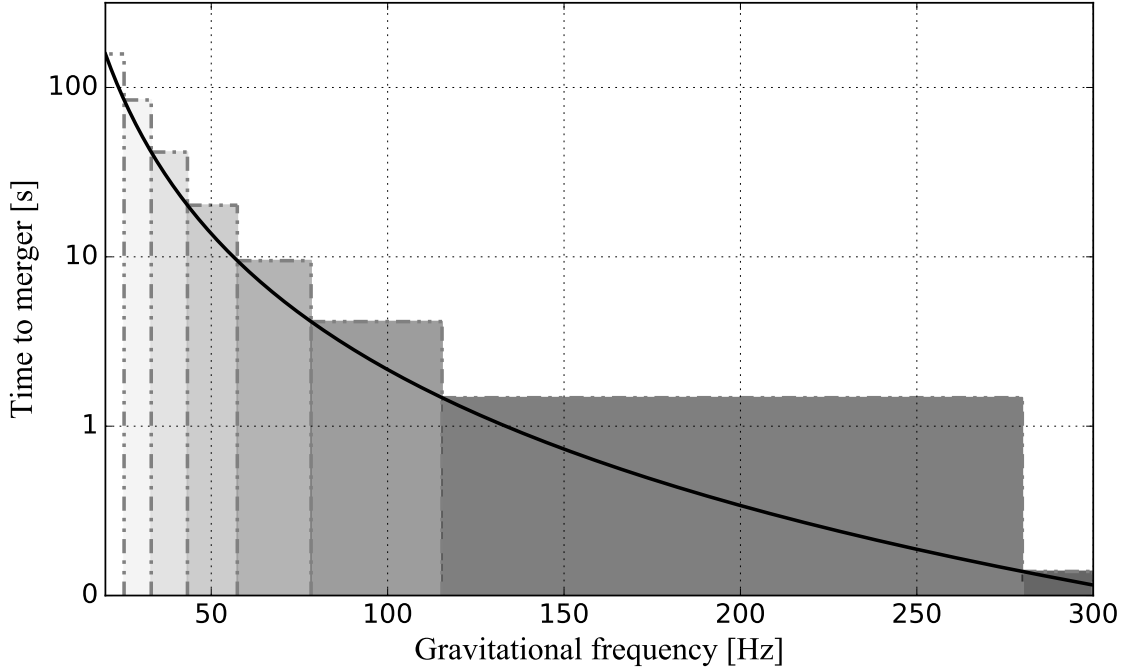
Figure 3.2: Time from a given frequency to coalescence for a fiducial binary neutron-star signal. Coloured boxes indicate the subdivision of the waveform into bands with adaptive frequency resolution, as determined by the time before coalescence; see section 3.3.2.

components of the signal at f_{max}.

To leading order, the duration of an inspiral signal from a certain frequency f to the formal time of coalescence is (Cutler and Flanagan, 1994) (in geometrical units $G = c = 1$)

$$t(f) \approx 5 \left[8\pi f \right]^{-8/3} \mathcal{M}^{-5/3}, \tag{3.19}$$

where $\mathcal{M} = M_1^{3/5} M_2^{3/5} (M_1 + M_2)^{-1/5}$ is the chirp mass of a binary with component masses $M_{1,2}$ and mass ratio $q = M_2/M_1 \leq 1$. During the inspiral, the gravitational-wave frequency monotonically increases until the merger and ring-down phases. An example is shown in figure 3.2, where we put frequency on the abscissa to emphasize that we are working in the frequency domain. In the standard calculation, there is a fixed frequency resolution of $\delta f = \tau^{-1}$ between frequency bins, and the total

number of frequency-domain samples required to describe the signal is

$$
\begin{aligned}
N_{\text{fix}} &= \int_{f_{\min}}^{f_{\max}} \delta f^{-1} df \\
&= (f_{\max} - f_{\min})\tau \\
&\approx 5(8\pi)^{-8/3} \mathcal{M}^{-5/3} (f_{\max} - f_{\min}) f_{\min}^{-8/3} \,.
\end{aligned}
\tag{3.20}
$$

We can see from the figure that this frequency resolution is necessary to contain the full length waveform starting at time τ before merger, but as the frequency increases the time before merger $t(f)$ decreases and the waveform is over-sampled in frequency. Our aim is to take advantage of this to increase δf as a function of frequency without losing any information about the waveform phasing, thereby reducing the total number of points at which the waveform must be evaluated.

We now consider the asymptotic limit of multi-banding. In the idealized limit, the frequency step $\delta f = t(f)^{-1}$ can vary continuously throughout the signal. We then have

$$
\begin{aligned}
N_{\min} &= \int_{f_{\min}}^{f_{\max}} t(f) df \\
&= -3(8\pi)^{-8/3} \mathcal{M}^{-5/3} (f_{\max}^{-5/3} - f_{\min}^{-5/3}) \,.
\end{aligned}
\tag{3.21}
$$

The relative number of points required for the standard case compared to the ideal case is then

$$
\frac{N_{\text{fix}}}{N_{\min}} = \frac{5}{3} \frac{(f_{\max} - f_{\min}) f_{\min}^{-8/3}}{f_{\min}^{-5/3} - f_{\max}^{-5/3}} \,,
\tag{3.22}
$$

which for $f_{\max} \gg f_{\min}$ indicates an asymptotic reduction in number of points $5 f_{\max}/3 f_{\min}$. For a BNS waveform which enters the detector at $20\,\text{Hz}$ and terminates at $1500\,\text{Hz}$, the potential reduction in number of points is therefore a factor of ~ 125.

Choice of bands

Rather than taking the continuously varying δf case, in our practical implementation we work with a pre-determined set of frequencies which divides the total frequency span into several bands with constant δf within each band. We position the bands in frequency space so that δf changes by a factor of 2 between neighboring bands, while ensuring that the Nyquist sampling criterion is always met.

Figure 3.2 shows a schematic of the basic idea. We must choose our bands such that they are able to accurately represent the longest waveform in our allowed mass prior. This can be determined automatically at run-time of the PE code; e.g., a $1+1M_{\odot}$ binary neutron star signals lasts $281\,\mathrm{s}$ from $20\,\mathrm{Hz}$ to coalescence. Starting at the lowest frequency f_{min}, the frequency resolution necessary to contain the waveform is $\delta f_0 \leq t(f_{\mathrm{min}})^{-1}$. Each subsequent band has a sampling rate $\delta f_b = 2\delta f_{b-1}$ and so the time at the start of the new band is a factor of two closer to coalescence, $t(f_b) = t(f_{b-1})/2$. The frequencies at which to place the band boundaries are then determined by inverting Eq. 3.19 and solving for the series of δf_b. To summarise, we can specify the frequencies at which the waveform is evaluated via the following algorithm

$\quad b = 0,\ i = 0$

$\quad \delta f_b = t(f_{\mathrm{min}})^{-1},\ f_i = f_{\mathrm{min}}$

$\quad$**while** $\underline{f_i < f_{\mathrm{max}}}$ **do**

$\quad\quad$**while** $\underline{t(f_i) > (2\delta f_b)^{-1}}$ **do**

$\quad\quad\quad f_{i+1} = f_i + \delta f_b$

$\quad\quad\quad i = i + 1$

$\quad\quad$**end**

$\quad\quad \delta f_{b+1} = 2\delta f_b$

$\quad\quad b = b + 1$

$\quad$**end**

Up-sampled waveform

Having defined the reduced set of frequencies at which the waveform is to be calculated, we now outline the procedure for reconstructing the full waveform. Note that unlike in reduced order quadrature methods, we still compute the likelihood using the fully sampled dataset. A naïve decimation or averaging of the frequency-domain detector data leads to a loss of information relative to the fully-sampled results. We therefore use an interpolation scheme to reconstruct the waveform at the full sampling rate in order to match filter the original data.

Direct linear interpolation of the reduced waveform $\tilde{h}(f_j)$ does not accurately reproduce the original waveform as the oscillatory behaviour is not captured by the interpolating straight line segments. We therefore work with the waveform represented in amplitude and phase as $\tilde{h}(f_j) = A_j \exp(i\phi_j)$, where j labels the reduced set of frequencies. Within each coarse bin, we linearly interpolate the amplitude A and phase ϕ to obtain estimates of the amplitude $\hat{A}_k = \hat{A}(\hat{f}_k)$ and phase $\hat{\phi}_k = \hat{\phi}(\hat{f}_k)$ at the dense set of frequencies $\hat{f}$ labeled with k:

$$\hat{A}_k = A_j + \frac{\hat{f}_k - f_j}{f_{j+1} - f_j}(A_{j+1} - A_j), \tag{3.23}$$

$$\hat{\phi}_k = \phi_j + \frac{\hat{f}_k - f_j}{f_{j+1} - f_j}(\phi_{j+1} - \phi_j), \tag{3.24}$$

where f_j is the nearest coarse frequency point below $\hat{f}_k$ and $\hat{f}_{k+1} - \hat{f}_k = \delta f_0$. The up-sampled waveform after multi-banding and interpolation (hereafter MB-Interpolation) is then $\tilde{h}(\hat{f}_k) = \hat{A}_k \exp(i\hat{\phi}_k)$.

One practical problem with applying this formula is that the exact estimation of $\exp i\hat{\phi}_k$ is computationally expensive. To avoid this we use the recursive property $e^{i\hat{\phi}_{k+1}} = e^{i\hat{\phi}_k} e^{i\delta f_0(\phi_{j+1} - \phi_j)/(f_{j+1} - f_j)}$. The last term needs to be computed only once for each coarse bin (Press et al., 2007). The recursion relation can be expressed in

terms of the real and imaginary parts of the complex frequency-domain signal as

$$
\Re(\hat{h}_{k+1}) = \left[1 + \frac{(A_{j+1} - A_j)\delta f_0}{\hat{A}_k(f_{j+1} - f_j)}\right]\left[\Re(\hat{h}_k)\left(1 - 2\sin^2\frac{\delta\phi_j}{2}\right) - \Im(\hat{h}_k)\sin\delta\phi_j\right],
$$

$$
\Im(\hat{h}_{k+1}) = \left[1 + \frac{(A_{j+1} - A_j)\delta f_0}{\hat{A}_k(f_{j+1} - f_j)}\right]\left[\Im(\hat{h}_k)\left(1 - 2\sin^2\frac{\delta\phi_j}{2}\right) + \Re(\hat{h}_k)\sin\delta\phi_j\right],
$$

where $\delta\phi_j \equiv \delta f_0(\phi_{j+1} - \phi_j)/(f_{j+1} - f_j)$; therefore we only need to compute $\sin(\delta\phi_j)$ and $\sin^2(\delta\phi_j/2)$ [1].

Accuracy

The waveform accuracy required for parameter estimation is determined by the condition that systematic bias in parameter estimates from imperfect waveforms should be much smaller than the statistical measurement uncertainty of inference on data with finite signal-to-noise ratios (e.g., (Ohme, 2012)). Therefore, the shift in the log likelihood due to the use of MB-Interpolation waveforms in lieu of the original waveforms, $\delta \log L_{\text{MB-Interpolation}}$, should be smaller than the spread in the log likelihood over the posterior $\sigma_{\log L}$:

$$
\delta \log L_{\text{MB-Interpolation}} \ll \sigma_{\log L} \sim \sqrt{\frac{N_{\text{param}}}{2}}, \tag{3.25}
$$

where N_{param} is the number of parameters in the model. This condition on the log likelihood can be expressed in terms of the match between the original waveform h_0 and the MB-Interpolation waveform h (Baird et al., 2013; Hannam et al., 2010; Haster et al., 2015):

$$
\frac{\langle h_0 - h | h_0 - h \rangle}{\langle h_0 | h_0 \rangle} \ll \frac{\sqrt{2N_{\text{param}}}}{\rho^2}, \tag{3.26}
$$

where ρ is the signal-to-noise ratio. Considering $\rho \sim 20$, typical for a moderately loud signal (Chen and Holz, 2014), the threshold on the mismatch is $\sim 10^{-3}$.

---

[1]The adopted recursion formulas are based on the Chebyshev approximation, which reach exponential accuracy for infinitely differentiable functions (Roger, 2002).

Figure 3.3 show that the mismatch of MB-Interpolation waveforms against the original waveforms is a factor of a thousand smaller than this requirement over the BNS region, decreasing for more massive systems. This is expected, as in the frequency domain the density of cycles at low frequency increases with the time duration of the waveform, so the most demanding case is that of the lowest mass considered in a particular analysis (in our case a $1 - 1\,M_\odot$ binary). Therefore, we conclude that this procedure provides sufficient accuracy for unbiased inference at all masses above $1 - 1\,M_\odot$.
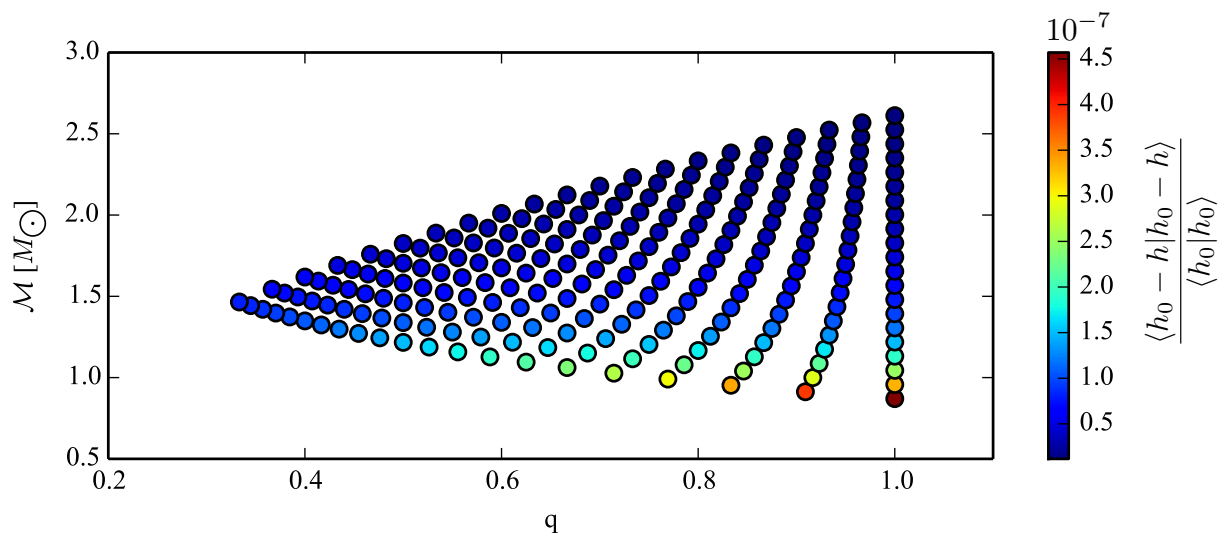
Figure 3.3: Mismatch of MB-Interpolation waveforms (h) against waveforms computed with the standard procedure (h_0) as a function of chirp mass and mass ratio. The mismatch is calculated up to 1024Hz.

3.3.3 Results

We implemented the MB-Interpolation approach (section 3.3.2), including the waveform interpolation procedure (subsection 3.3.2) within `LALInference` (Veitch et al., 2015b). We performed several tests in order to validate MB-Interpolation. We first checked the effectiveness of the MB-Interpolation by verifying the reduction of the number of frequencies at which the template is evaluated when multibanding. We then measured the speedup in the waveform computation following multibanding and interpolation. Finally, we tested the overall acceleration of the complete PE

analysis with MB-Interpolation and confirmed its accuracy.

Reduction of template evaluations

To measure the speedup in waveform generation we first defined the frequency set at which the multibanded template is evaluated according to the algorithm in section 3.3.2. The in-band signal duration is set by a BNS with both component masses equal to $1M_\odot$ as a reference system, corresponding to the lowest limit of the component mass prior adopted in the analysis. The number of frequencies at which the waveform is evaluated is shown in figure 3.4 as a function of the starting frequency $f_{\min}$ for both MB-Interpolation and the standard algorithm. This figure clearly demonstrates the effectiveness of the approach in reducing template evaluations: the number of frequencies defining the two sets, N_{fix} and N_{MB} respectively for the standard and the MB-Interpolation algorithm, differs by an order of magnitude or more for starting frequencies below 40 Hz.

The evident segmented structure of N_{MB} reflects the varying number of frequency bands used in MB-Interpolation. Within each band, δf is constant and the number of frequencies follows the same $\sim f_{\min}^{-8/3}$ scaling as for the standard algorithm. As expected, this yields sub-optimal behaviour relative to the theoretical limit of a continuously varied sampling frequency, as clearly demonstrated by the ideal case (green line) falling well below the actual N_{MB} points in the same figure.

Speedup of waveform generation

We measured the reduction in the total waveform generation time, including both multibanding and interpolation, for compact binary systems with chirp-mass of $\sim 1.48\, M_\odot$. The waveforms were generated up to a frequency $f_{\max}$ of 2048 Hz with a time domain sampling rate of 4096 Hz. We used two different waveform models for both generating and analysing injections to test the efficacy of our approach: *TaylorF2* (see for example (A. Buonanno et al., 2009)) and *IMRPhenomPv2* (Hannam et al., 2014). The former is one of the simplest and most common waveform models
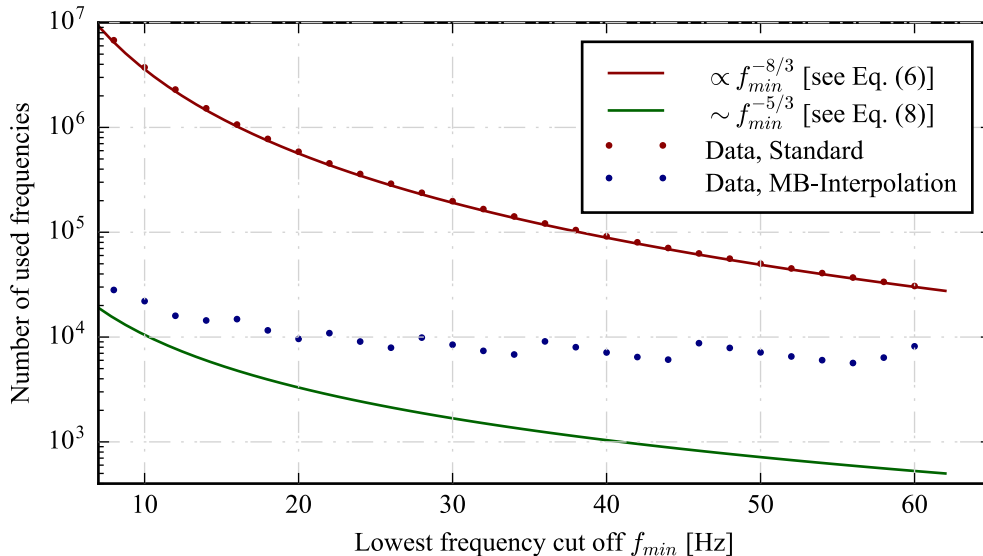
Figure 3.4: Number of frequencies at which the waveform is evaluated when using the standard (N_{fix}, red dots) and MB-Interpolation (N_{MB}, blue dots) algorithms as a function of the lower frequency limit. The red curve corresponds to equation 3.20 while the green curve shows the number of frequency samples in the theoretical limit of continuously adapted sampling steps, equation 3.21. MB-Interpolation is sub-optimal but approaches the asymptotic case in the limit $f_{\text{min}} \to 0$, as the templates become very long and δf_0 approaches 0; the number of frequency bands increases from 3 at $f_{\text{min}} = 60$ Hz to 8 at $f_{\text{min}} = 20$ Hz and 11 at $f_{\text{min}} = 8$ Hz.

available for the coalescence of compact binaries. It analytically describes the inspiral stage of the coalescence using the *stationary phase approximation*. Meanwhile, the analytical *IMRPhenomPv2* model includes the inspiral, merger and ringdown phases, calibrated to numerical relativity simulations. The *IMRPhenomPv2* waveform family has been used to characterise the BBH systems discovered during O1, the first science run of Advanced LIGO (Abbott et al., 2016b). *IMRPhenomPv2* waveforms are more sophisticated and more computationally expensive than *TaylorF2* ones. Since the main effect of the proposed method is reducing the number of template evaluations, it is for computationally expensive cases that we expect to benefit the most from its application. Figure 3.5 shows the speedup in the template generation as a function of the starting frequency, for the *TaylorF2* waveform model in the left panel, and for *IMRPhenomPv2* in the right one. The length of the data segments was set by calculating the duration of a BNS signal with $1 \, M_{\odot}$ components starting from the chosen f_{min}. The template generation speed was calculated
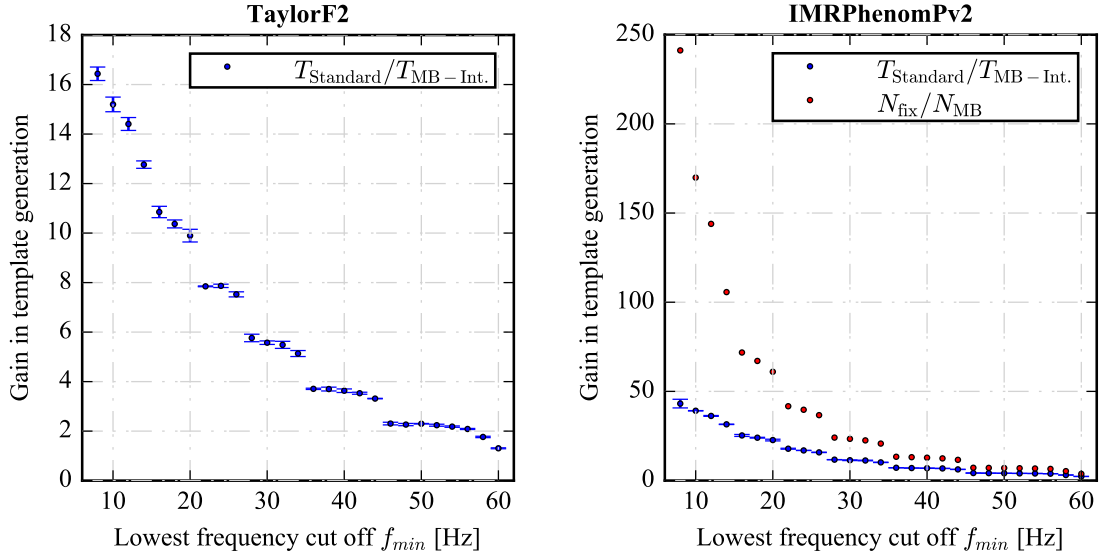
Figure 3.5: Gain factor in computational speed of template generation as a function of $f_{\min}$. Blue points: ratio of the average waveform computation cost for the standard procedure versus MB-Interpolation as a function of the starting frequency for *TaylorF2* (left panel) and *IMRPhenomPv2* (right panel) waveform families. Red points in right panel: ratio between the number of frequencies at which the waveform is evaluated when using the standard procedure versus MB-Interpolation.

by averaging the time necessary to construct one waveform over 3000 (300) trials for the *TaylorF2* (*IMRPhenomPv2*) model. We define the gain in speed (blue points in figure 3.5) as the ratio between the average time required by the standard and the MB-Interpolation algorithms to compute one template.

For comparison, the right panel of figure 3.5 includes the reduction in the number of frequencies at which the waveform is evaluated when using MB-Interpolation, $N_{\mathrm{fix}}/N_{\mathrm{MB}}$ (red points). The gains for MB-Interpolation are smaller than the ratio $N_{\mathrm{fix}}/N_{\mathrm{MB}}$ because of the additional cost of interpolating between the N_{MB} frequency samples.

We find that the MB-Interpolation scheme yields a dramatic gain in computational speed for smaller values of $f_{\min}$. At $f_{\min} = 20\,\mathrm{Hz}$ *TaylorF2* templates were accelerated by a factor of 10. The slower *IMRPhenomPv2* family shows significantly greater gains than the faster *TaylorF2* family, as illustrated by the difference in ordinate scales between the two panels of figure 3.5. Thus, *IMRPhenomPv2* template generation was around 25 times faster with MB-Interpolation at $f_{\min} = 20\,\mathrm{Hz}$.

While both waveform families show a greater gain for smaller values of $f_{\min}$, the same segmentation is present as in figure 3.4, although this is less obvious for the *TaylorF2* family. This reflects the dependence of the time required to compute one waveform, T, on the number of frequency bands.

Within the standard approach, this time T_{Standard} can be approximated as the product of the time necessary to calculate the waveform at a given frequency t^{w} with the number frequencies N_{fix}:

$$T_{\text{Standard}} \sim N_{\text{fix}} \cdot t^{\text{w}}. \tag{3.27}$$

To estimate the same time in the MB-Interpolation algorithm we need to take into account two different contributions: the template generation applied to a reduced set of frequencies, and the calculations necessary for the waveform interpolation t^{i}. This leads to the following approximation:

$$T_{\text{MB-Int.}} \sim N_{\text{fix}} \cdot t^{\text{i}} + N_{\text{MB}} \cdot \left(t^{\text{w}} + \delta t^{\text{i}}\right) \tag{3.28}$$

Here δt^{i} represents the time required to compute the quantities necessary for the interpolation (such as phase, derivatives, etc.); typically $\delta t^{\text{i}} \ll t^{\text{w}}$.

According to Eq. 3.28, the time required to compute a complete waveform via MB-Interpolation depends on $f_{\min}$ only through N_{fix} and N_{MB}. However, the first term in Eq. 3.28 becomes increasingly dominant as $f_{\min}$ decreases, since $N_{\text{fix}} \propto f_{\min}^{-8/3}$. For sufficiently small $f_{\min}$, $N_{\text{fix}} \cdot t^{\text{i}} \gg N_{\text{MB}} \cdot \left(t^{\text{w}} + \delta t^{\text{i}}\right)$ and the speedup asymptotes to a fixed factor $T_{\text{Standard}}/T_{\text{MB-Int.}} \to t^{\text{w}}/t^{\text{i}}$, independent of $f_{\min}$. The frequency at which this happens depends in general on the computational cost of the particular waveform model. The results reported in figure 3.5 suggest gains exceeding ~ 16 ($\sim$ 50) for starting frequencies below 8 Hz for the *TaylorF2* (*IMRPhenomPv2*) waveform models.

Inference

To verify that the results obtained with the MB-Interpolation algorithm remain accurate, and to measure the speedup of an end-to-end inference run, we also performed several complete PE analyses. We injected a gravitational-wave signal emitted by a BNS with component masses $M_1 = M_2 = 1.4\,M_\odot$ into stationary Gaussian noise, coloured according to the design sensitivity curves of advanced LIGO and Virgo (Aasi et al., 2016). The signal was always injected at a distance of $D_L \approx 200\,\mathrm{Mpc}$ so that the SNR at $f_{\min} = 40\,\mathrm{Hz}$ source was 15; signals with lower $f_{\min}$ have correspondingly higher SNR.

The PE analyses were performed with `LALInferenceNest`, using the same maximum frequency $f_{\max} = 2048\,\mathrm{Hz}$ and time-domain sampling rate (4096 Hz) adopted in section 3.3.3. Priors on companion masses were uniform in the range $1-3\,M_\odot$ and the prior on distance was uniform in volume with a maximum distance of 500 Mpc. We chose this region of mass space as it is the most challenging in terms of computational cost and has the strictest accuracy requirements for waveform interpolation.

PE Consistency

The analysis of the mock data with MB-Interpolation templates produced posterior distributions statistically identical to the ones obtained with a standard analysis. As a representative case, in figure 3.6 we show the marginalised posterior probability density functions for chirp mass, mass ratio and luminosity distance, the quantities most sensitive to phase and amplitude errors. We confirmed the visual agreement between the marginal probability distributions obtained with the standard and the MB-Interpolation algorithms by performing a Kolmogorov-Smirnov test, which showed that the two sets of samples are consistent with random draws from the same distribution.
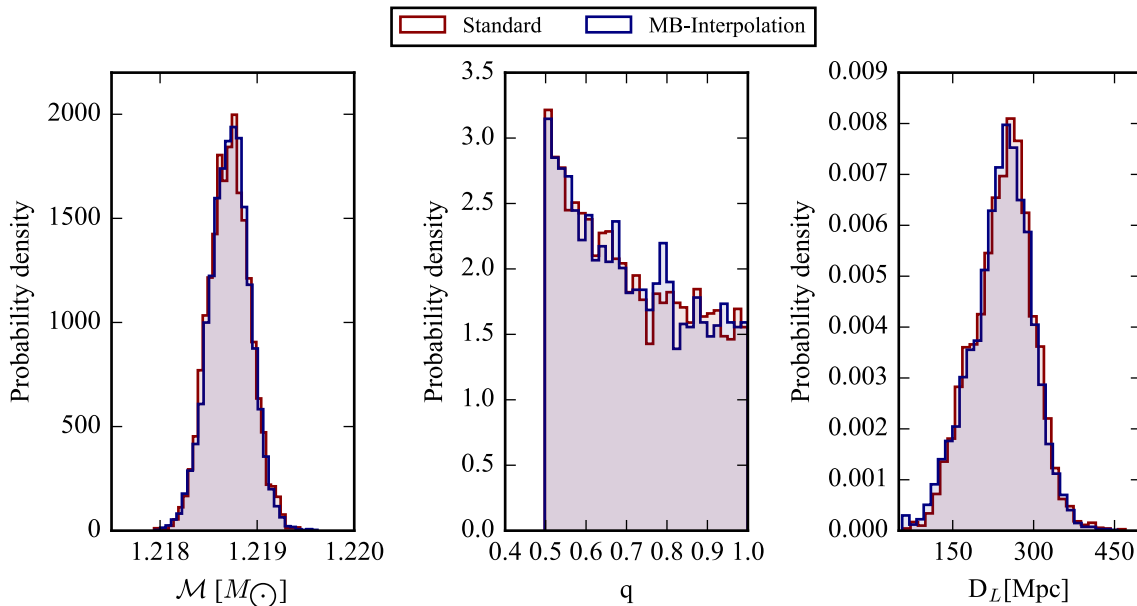
Figure 3.6: Posterior distributions of chirp mass $\mathcal{M}$, mass ratio q and luminosity distance D_L with the *TaylorF2* waveform model.

PE speedup

To test the effect of the speedup in the waveform generation on the overall PE analysis, we measured the computational time required to perform end-to-end PE runs. We performed PE analyses from different values of the starting frequency $f_{\min}$, consequently changing the lengths of the data segments. The results are reported in table 3.1 and figure 3.7.

For each starting frequency and for both standard and MB-Interpolation algorithms, the times of 4 runs have been averaged. The ratio between the average time required to complete a PE analysis adopting the standard and the MB-Interpolation algorithms has been used to define the overall speedup gain G_{PE}. Each group of 4 identical analyses has been run at the same time on a Dual-Core AMD Opteron 2218 Processor with a clock speed of 2.6GHz.

Table 3.1 reports the measured speed gain for the whole PE analysis with the *TaylorF2* (abbreviated as TF2) waveform model in the third column. The fourth column contains the speedup in the template calculation (cf. fig. 3.5). In the last two columns we also report the ratio between the number of frequencies at which

the waveform is evaluated in the standard and the MB-Interpolation algorithms $N_{\text{fix}}/N_{\text{MB}}$, as well as the idealized improvement in the limit of continuously adapted sampling rates $N_{\text{fix}}/N_{\text{min}}$ (equation 3.22).

As can be seen from table 3.1, we do not obtain the full idealised gain that may be expected from multi-banding for three reasons. Firstly, the actual number of frequencies at which the waveform is computed in our multi-banding algorithm is larger than the theoretical limit, so $N_{\text{fix}}/N_{\text{MB}} < N_{\text{fix}}/N_{\text{min}}$. Secondly, the template computation speedup is less than the reduction in the set of frequencies due to multi-banding, $G_{\text{template}} < N_{\text{fix}}/N_{\text{MB}}$, because of the additional cost of interpolation. Thirdly, the PE speedup is smaller than the speedup in template generation, $G_{\text{PE}} < G_{\text{template}}$, because template generation is only one component of the PE algorithm. Although the waveform computation is the dominant computational cost for computationally expensive templates, the cost of evaluating the likelihood still grows with the number of frequency bins even when using MB-Interpolation, and along with interpolation this can become the most expensive step when using MB-Interpolation with very long waveforms.

We did not repeat the end-to-end parameter estimation calculations across the full range of starting frequencies with *IMRPhenomPv2* waveforms because the computational cost was unacceptably high when using the standard procedure. Nonetheless, it is possible to estimate the computational cost gain one would achieve with *IMRPhenomPv2* waveforms when starting with low values of f_{min}. For computationally expensive waveforms, the parameter estimation cost is dominated by the waveform computation cost; this is a factor of ~ 3 higher for *IMRPhenomPv2* waveforms than for *TaylorF2* waveforms. (This factor is independent of the waveform duration or starting frequency, and reflects the difference in the cost of computing the two waveforms at a given frequency point.) Therefore, we expect that the total PE computational cost with *IMRPhenomPv2* waveforms to be about the same factor of 3 larger than for *TaylorF2* waveforms when starting at low frequencies and using the standard procedure. Meanwhile, for sufficiently low starting frequencies,

the MB-Interpolation waveform computation cost is dominated by interpolation, so that the template computation cost with *IMRPhenomPv2* and *TaylorF2* waveforms when using MB-Interpolation asymptotes to the same value – and so does the full PE computational cost. Thus, we expect that end-to-end PE gains from using MB-Interpolation with *IMRPhenomPv2* will be a factor of ~ 3 greater than with *TaylorF2* waveforms.

MB-Interpolation is most effective for smaller values of the starting frequency. fig. 3.5 shows that with $f_{\min} = 8\,\mathrm{Hz}$ the template speed-up factor is ~ 16 for *TaylorF2* waveforms and ~ 50 for *IMRPhenomPv2* waveforms, where we conservatively assume that there are no further significant gains in waveform computation at lower starting frequencies because of fixed interpolation costs. As discussed above, the total PE speed-up will not be as large as the speed gain in template generation because of other fixed costs. Nevertheless, as next generation interferometers (such as the Einstein Telescope (Punturo et al., 2011), KAGRA (Aso et al., 2013) and the Cosmic Explorer (LIGO, 2015)) take advantage of low-frequency data, MB-Interpolation should improve parameter estimation costs by factors of tens, or more for more expensive waveform models.

$\mathbf{f}_{\min}[Hz]$	$\boldsymbol{\delta}\mathbf{f}_0[Hz]$	$\mathbf{G}_{\mathrm{PE}}^{\mathrm{TF2}}$	$\mathbf{G}_{\mathrm{template}}^{\mathrm{TF2}}$	$\mathbf{N}_{\mathrm{fix}}/\mathbf{N}_{\mathrm{MB}}$	$\mathbf{N}_{\mathrm{fix}}/\mathbf{N}_{\mathrm{min}}$
60	1/16	1.09 ± 0.03	1.31 ± 0.01	3.76	55.4
40	1/64	1.56 ± 0.05	3.8 ± 0.1	12.82	83.8
30	1/128	1.91 ± 0.07	5.5 ± 0.1	23.40	112.2
20	1/300	2.72 ± 0.14	8.8 ± 0.2	61.01	169.1

Table 3.1: The table reports the results obtained for different values of starting frequency $f_{\min}$ (first column) and corresponding sampling steps δf_0 for standard template generation (second column). The values $G_{\mathrm{PE}}^{\mathrm{TF2}}$ are the actually measured speed gains in the complete PE analyses with *TaylorF2* due to using MB-Interpolation. $G_{\mathrm{template}}^{\mathrm{TF2}}$ is the gain in the waveform generation speed ($T_{\mathrm{Standard}}/T_{\mathrm{MB-Int.}}$). $N_{\mathrm{fix}}/N_{\mathrm{MB}}$ is the ratio between the number of frequencies at which the standard and multi-banded waveforms are evaluated, while $N_{\mathrm{fix}}/N_{\mathrm{min}}$ is the limiting case for the reduction in waveform evaluations when continuously adapting frequency steps.
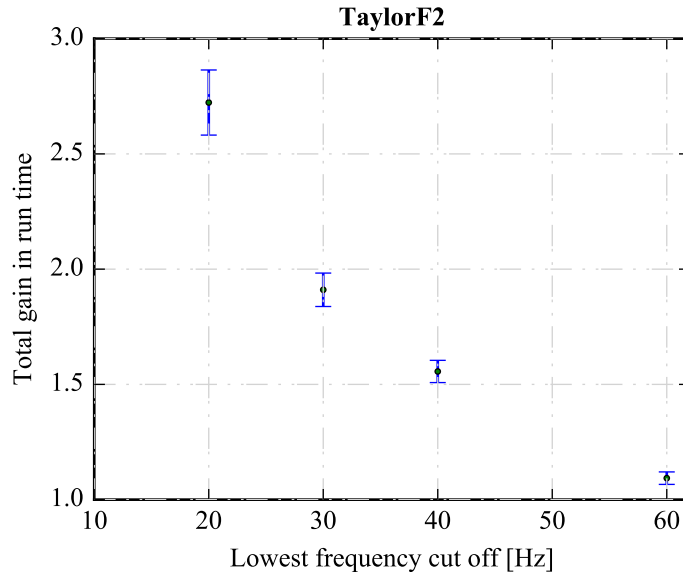
Figure 3.7: Observed gains in the end-to-end PE run-time, $G_{\mathrm{PE}}^{\mathrm{TF2}}$, as a function of the starting frequency for analyses carried out with *TaylorF2* waveforms.

3.3.4 Conclusions

Parameter estimation has played an important role in the opening of the field of gravitational-wave astronomy, as demonstrated in the analysis of Advanced LIGO's first observations (Abbott et al., 2016f,b). The stochastic sampling algorithms used in these analyses require the generation of millions of template waveforms which are compared to the data, a computational task that becomes more expensive as the in-band signal duration increases: for signals from lower mass binaries and for detectors with improved sensitivities at lower frequencies. The generation of computationally expensive template waveforms is the bottleneck in the PE analysis, limiting our ability to obtain results quickly. In this paper we proposed an alternative approach to reduce this cost and consequently the overall time required to produce a result. The procedure is inspired by the same *multi-banding* approach already adopted for low-latency algorithms dedicated to gravitational-wave searches (Cannon et al., 2012b; Adams et al., 2016). It consists in reducing the set of frequencies at which to evaluate waveforms by dividing the spectral range into different bands and optimising the sampling procedure. However, the greater accuracy required in the context of PE demanded an additional up-sampling of the waveform when computing the likelihood

function, which led us to apply a linear interpolation in phase and amplitude.

We have demonstrated the effectiveness of the method by implementing it in the `LALInference` PE code and comparing the results to inference with the full waveform. We found negligible differences between the results at a greatly reduced computational cost. We showed that the MB-Interpolation algorithm reduces the number of frequencies at which the waveform is evaluated by more than an order of magnitude for $f_{\min} < 40\,\mathrm{Hz}$. This leads to an acceleration of the waveform generation and, consequently, the whole analysis. For a fixed chirp mass of the binary, the speed-up factor depends on the complexity of the model and on the starting frequency $f_{\min}$. We studied the most challenging case of BNSs, adopting the *TaylorF2* and *IMRPhenomPv2* waveform families. In section 3.3.3 we reported speedup factors in the template generation which reached ~ 50 for the most sophisticated waveform model (*IMRPhenomPv2*) at $f_{\min} \sim 10\,\mathrm{Hz}$. Although the overall decrease in the computational cost of end-to-end PE is more modest than the improvement in template generation because of fixed costs, we expect factors of tens in speed gain when using *IMRPhenomPv2* templates with starting frequencies of a few Hz. The considerable speedup gains reached by the implementation of the MB-Interpolation method demonstrates the effectiveness of the approach.

Our method is related to the reduced order quadrature models of gravitational-waveforms introduced for the simple TaylorF2 model in (Field et al., 2011) and later created for more sophisticated SEOBNR and IMRPhenomP models (Smith et al., 2016). These methods also result in a large acceleration of PE, by factors of 70 for a TaylorF2 waveform (Canizares et al., 2015a) or 300 for IMRPhenomPv2 (Smith et al., 2016) from $20\,\mathrm{Hz}$. The two methods are conceptually similar in that the number of points in frequency at which the waveform is evaluated is reduced. However, for ROQ the interpolation makes use of a different set of bases, which means that interpolation must be performed across the parameter space of the signals in addition to interpolation in frequency. Unlike our MB-Interpolation method, this requires significant setup costs to create the parameter space interpolants, which are difficult to

produce for the higher dimensional precessing spin parameter space. In this regard our method is more flexible, since it can be used for any signal without pre-computing a reduced order model. This is advantageous in the case of models which include additional physical parameters, such as neutron-star tidal deformability, which further increase the dimensionality of the parameter space. The MB-Interpolation method can also be used in combination with ROQ, where the MB-Interpolation is used to accelerate the initial creation of the ROQ model by reducing the number of calculations and also the memory overhead. Indeed, the reduced frequency basis idea was used in (Smith et al., 2016), but without the interpolation up-sampling step.

Accelerated waveform generation techniques such as the one we have developed here are likely to be essential in future, as the detectors evolve toward greater sensitivity at low frequencies. Third-generation detectors such as the Einstein Telescope (Punturo et al., 2011) or LIGO Voyager (McLelland et al., 2016) will be sensitive down to a few Hz, meaning signals may be in band for hours or longer. The same MB-Interpolation procedure can also be applied to GW studies in the context of space missions (Porter, 2014), and in particular for phase-coherent modeling of the signal in both space-based and ground-based detectors as would be useful for joint science exploitation (Sesana, 2016; Vitale, 2016).

In principle, a similar multi-banding approach could also be applied to time-domain waveforms, which could be sampled at a lower rate earlier in the waveform. However, the time domain waveforms of greatest interest use numerical integration of the waveform with an adaptive step size in time. This prevents a great speedup from being obtained as one cannot reduce the step size arbitrarily in the simple way we could for the frequency domain waveforms. This factor, in addition to the technical difficulty of efficiently reconstructing the FFT of a non-uniformly sampled time series prevented us from exploring this option in the current work.

Finally we note that despite the specialisation to gravitational-wave analysis, the same technique of adapting the sampling interval could be applied to any area where the signal frequency changes monotonically with time.

Chapter 4

Signal classification in GW burst searches

In this chapter we present a first case study of signal classification in the context of unmodelled searches targeting GW transients (sec. 4.4). We start the chapter (sec. 4.1) introducing these signals and the main concepts behind the generic methods dedicated to their detection. In section 4.2, we then briefly describe one of the LVC flagship pipelines dedicated to such analysis, `coherent WaveBurst`. Finally, in section 4.3, we give a brief overview of the artificial neural networks we use in our GW study, presented in section 4.4.

Part of the overview material in sections 4.1, 4.2 and 4.3 reproduces the introductory chapters of my master thesis (Vinciguerra, 2014b). Section 4.4 reproduces the text of (Vinciguerra et al., 2017a), published in the Journal Classical and Quantum Gravity. The overall idea described in the paper was discussed by all the authors. Gabriele Vedovato proposed using artificial neural network to recognise the time-frequency chirping feature, typical of signals emitted by CBCs. I implemented the main part of the post-processing code required by the specific application presented in the paper and ran all the tests. Code review and editing was done in collaboration with Marco Drago. Gabriele Vedovato wrote the plug-in necessary for the extraction

of time-frequency event representation from the main transient analysis performed by coherent WaveBurst. The main developers to the pipeline are Gabriele Vedovato, Sergey Klimenko and Marco Drago, while Valentin Necula and Vaibhav Tiwari contributed specific sections. Gabriele Vedovato also wrote the code dedicated in converting the time-frequency map produced by coherent WaveBurst into a normalised matrix. Such script was later modified by myself. Results and further applications of such methodology were discussed by all authors: myself, Marco Drago, Giovanni Andrea Prodi, Sergey Klimenko, Claudia Lazzaro, Valentin Necula, Vaibhav Tiwari, Maria Concetta Tringali, Gabriele Vedovato. Details of the analysis, results and their potential implications were considered by myself, Marco Drago, Giovanni Andrea Prodi and Sergey Klimenko. We compared and combined the results of our methodology with the classification performed by an already implemented fit of chirp - mass (see 4.4 for further detail). I produced all the plots presented in the paper, while the text was written by myself in collaboration with Marco Drago and Giovanni Andrea Prodi, with modifications from Vaibhav Tiwari and Francesco Salemi.

4.1 Generic gravitational-wave transients

GW transients are signals characterised by a short time (from ms to minutes) duration, emitted during very violent events happening in our Universe. These transients include gravitational emissions generated by a large variety of phenomena, some of which are not well known. There are two main approaches for the detection of GW transients: template-based methods and unmodelled searches. The former is very effective for GWs generated by standard compact binary coalescences (CBCs), whose GW emission is theoretically modelled up to good approximations (as demonstrated by current GW detections (Abbott et al., 2016b), (Abbott et al., 2017c), (Abbott et al., 2017d), (Abbott et al., 2017e), (Abbott et al., 2017g)). However the gravitational emission produced by more exotic binaries, such as intermediate-mass black-hole (BH) binaries (Mazzolo, 2013; Mazzolo et al., 2014; Abbott et al., 2017i), eccentric BH binaries (Tiwari et al., 2016) and BH-NS (neutron-star) systems (Pan-

narale et al., 2015), are not yet well approximated. A general approach is therefore necessary to detect weakly constrained signals, coming from both predicted and unknown sources. Burst searches aim at the detection and characterisation of poorly understood GW transients. Contrary to match filtering techniques, these general analyses benefit from targeting a subclass of specific sources, even if complex to model, as the mentioned coalescences of exotic compact binaries. Indeed, while for template-based approaches this complexity requires increasingly more sophisticated waveforms, in burst searches it introduces constrains which simplify the overall analysis reducing the available parameter space.

CBCs and supernovae (SNe) explosions and are among the most promising sources of GW bursts. However other astrophysical events have been suggested as progenitors of transients lying in the sensitivity band of ground based detectors: (i) r-modes and bar instabilities of new born NSs, (ii) accretion-induced collapse of white-dwarfs, (iii) phenomena linked to electromagnetic super flares and (iv) cosmic string cups and kinks.

Within the LIGO-Virgo collaboration, many efforts have been devoted to the development of pipelines dedicated to the detection of these weakly modelled (or completely unknown) GW signals; in the following we focus on `coherent WaveBurst`.

4.2   Coherent Waveburst Analysis

`coherent WaveBurst`(`cWB`) is a LIGO-Virgo collaboration pipeline dedicated to the detection of unmodelled GW transients. Algorithms aimed at this kind of searches are designed to be robust against the variety of possible astrophysical signals. `cWB` is implemented using ROOT, a software written in C++ and developed for the particle physics data analysis by CERN. The core of the pipeline consists in a preliminary event selection based on the likelihood analysis. Interaction with this main process are possible thanks to scripts called *Plugins*, which are customised according to the case study.

The all-sky search is one of the main analyses performed with `cWB`; it consists in iden-

tifying GW transients, adopting only minimal assumptions on the signal characteristics, leaving substantially unconstrained key properties such as strain evolution, GW direction and time of arrival. However searches more focused on particular signals or triggered by external electromagnetic events (e.g. Gamma Ray Bursts, hereafter GRBs) are also available within cWB. These more selective analyses are particularly important to maximise the detection chances in the context of the multi-messenger astronomy, just opened with the first observation of a BNS merger (Abbott et al., 2017h). Indeed, while for this event GRB 170817A and GW170817 independently triggered both the gravitational and electromagnetic searches, this will probably not be the standard scenario in the future, which will therefore require follow-ups with targeted analyses.

cWB algorithm classifies GW candidates according to their background occurrence (further discussed 4.2.2). Labelling triggers as GW signals or noise artefacts can

	Signal presence	Signal absence
Hypothesis of presence	True Alarm	False Alarm
Hypothesis of absence	False Dismissal	True Dismissal

Table 4.1: Possible cases derived by decision rules.

results in the four outcomes reported in table 4.1. Two kinds of errors are possible: the *true dismissals* and the *false alarms*. In our case, true dismissals are real (or simulated) astrophysical signals which the analysis cannot distinguish from the background. False alarms are instead noise artefacts (glitches), classified as GW signals. The correct evaluation of GW signals and glitches is respectively represented in the table as true alarm and false dismissals. Performances of detection pipelines are usually represented with Receiver Operating Characteristic (ROC) curves, based on true and false alarms. True alarms are strictly related to the efficiency of the analysis, which for searches of GW transients can be estimated from the fraction of injected waveforms recovered by the pipeline. In the context of GW generic searches, as the all-sky analysis performed by cWB, the signal characteristic which mostly affects the detection efficiency is the root-sum-square of the GW amplitude:

h_{rss}:

$$h_{rss} = \sqrt{\int_{-\infty}^{+\infty} h(t)^2 \, dt} \tag{4.1}$$

The main limitation of unmodelled analyses consists in the impact of non-Gaussian noise tails, which can mimic signal characteristics. To better identify glitches, several sensors monitor the environment surrounding the interferometers. The data collected by these sensors are then recorded in output channels used to reject or clean data (see (Abbott et al., 2016e) and references therein) affected by environmental disturbances. This procedure is particularly important for unmodelled GW searches, as the all-sky search for GW transients.These weakly constrained analyses often rely on the correlation between the data collected by different interferometers. There are two different approaches to analyse multiple streams of data: *incoherent*, i.e. the final list of GW candidates is obtained by the analysis of the multiple lists of triggers, previously produced for each single detector; and *coherent*, i.e. the data collected by the different interferometers is immediately combined for a unique analysis, leading to a single trigger list. `cWB` adopts a coherent approach and therefore requires the operation of a network of GW detectors. The simplified concept behind such analysis is the identification of the most energetic data which show coherent characteristics between the different detectors. The main challenge of such generic search consists in identifying astrophysical GW signals among the list of triggers, often generated by instrumental or environmental disturbances. `cWB` pipeline adopts a coherent method to analyse the data stream of a detector network based on a *Constrained Likelihood* approach, introduced in the following section.

4.2.1   Likelihood method

As presented in section 3.1, given the data $\mathbf{d} = \mathbf{h} + \mathbf{n}$, with $\mathbf{h} = \mathbf{h}_+ \, F_+ + \mathbf{h}_\times F_\times$, the likelihood allows to test two different hypothesis: the absence $p(\mathbf{d}|H_n, \mathbf{S_n})$ and the presence $p(\mathbf{d}|H_{h+n}, \mathbf{S_n})$ of a GW signal, assuming Gaussian white noise with 0 mean.

The ratio between $p(\mathbf{d}|H_{h+n},\mathbf{S_n})$ and $p(\mathbf{d}|H_n,\mathbf{S_n})$ is then used to discriminate noise from signals.

$$
\begin{aligned}
L &= \log\left[\frac{p(\mathbf{d}|H_{h+n},\mathbf{S_n})}{p(\mathbf{d}|H_n,\mathbf{S_n})}\right] = -\frac{1}{2}\sum_{i=1}^{N}\left[\langle h_i|h_i\rangle - 2\Re\langle h_i|d_i\rangle\right] \\
&\approx -2\sum_{i=1}^{N}\sum_{j=0}^{J}\frac{h_{ij}^2 - 2\,d_{ij}\,h_{ij}}{\tau S_{n,i}} \\
&= \sum_{i=1}^{N}\sum_{j=0}^{J}\frac{1}{\sigma_{ij}}\left(d_{ij}h_{ij} - \frac{1}{2}h_{ij}^2\right)
\end{aligned}
\tag{4.2}
$$

where we sum over the J frequencies of data and the N GW-detectors in the network (more details can be found in (Veitch and Vecchio, 2010)). In presence of a network of interferometers it is convenient to introduce a different representation of data. We define a mathematical space whose dimension is set by the number of detectors. The space can be defined imposing orthonormality between the normalised antenna pattern vectors $f_+ = (F_{1+}/\sigma_1, F_{2+}/\sigma_2...F_{N+}/\sigma_N)$ and $f_\times = (F_{1\times}/\sigma_1, F_{2\times}/\sigma_2...F_{N\times}/\sigma_N)$ (i.e. $f_+ \cdot f_\times = 0$). This space is called *Dominant Polarisation Frame* (DPF). In this frame, L can be rewritten as:

$$
\begin{aligned}
L &= \left(D \cdot H - \frac{1}{2}H \cdot H\right) \\
&= \left[D \cdot (f_\times \mathbf{h}_\times + f_+ \mathbf{h}_+) - \frac{1}{2}(f_\times \mathbf{h}_\times + f_+ \mathbf{h}_+)\cdot(f_\times \mathbf{h}_\times + f_+ \mathbf{h}_+)\right] \\
&= \left[D \cdot f_\times \mathbf{h}_\times + D \cdot f_+ \mathbf{h}_+ - \frac{1}{2}(f_\times^2 \mathbf{h}_\times^2 + f_+^2 \mathbf{h}_+^2)\right]
\end{aligned}
\tag{4.3}
$$

where $D = (\mathbf{d}_1/\sigma_1, \mathbf{d}_2/\sigma_2, ..., \mathbf{d}_N/\sigma_N)$, $H = (\mathbf{h}_1/\sigma_1, \mathbf{h}_2/\sigma_2, ..., \mathbf{h}_N/\sigma_N)$ and $F_{+/\times}$ are vectors in this DPF frame, while $\mathbf{h}_{+/\times}$ are the time series correspondent to the real GW polarisations. Here, to further simplify the notation we also normalise all the vector elements to the correspondent standard deviation σ_i. Since cWB is dedicated to unmodelled searches, differently form chapter 3.1, the two GW polarizations $\mathbf{h}_\times$

and $\mathbf{h}_+$ are unknown and the likelihood ratio is therefore maximised over them:

$$
\begin{aligned}
\frac{\delta L}{\delta h_\times} &= D \cdot f_\times - |f_\times|^2 \mathbf{h}_\times = 0 \\
\frac{\delta L}{\delta h_+} &= D \cdot f_+ - |f_+|^2 \mathbf{h}_+ = 0
\end{aligned}
\tag{4.4}
$$

which imply:

$$
\begin{aligned}
\mathbf{h}_\times &= \frac{D \cdot f_\times}{|f_\times|^2} \\
\mathbf{h}_+ &= \frac{D \cdot f_+}{|f_+|^2}
\end{aligned}
\tag{4.5}
$$

Adopting such solutions for the GW polarisations implies the maximum L is:

$$
L_{max} = \frac{1}{2} \left(\frac{(D \cdot f_\times)^2}{|f_\times|^2} + \frac{(D \cdot f_+)^2}{|f_+|^2} \right)
\tag{4.6}
$$

The detector response to the GW polarisations so defined can therefore be written as:

$$
H = \mathbf{h}_\times f_\times + \mathbf{h}_+ f_+ = D \cdot \hat{e}_\times + D \cdot \hat{e}_+
\tag{4.7}
$$

where $\hat{e}_\times$ and $\hat{e}_+$ are unitary vectors defined as $\hat{e}_\alpha = f_\alpha/|f_\alpha|$, with $\alpha = [+, \times]$. The detector response H is therefore the projection of the data D on the plane defined by the antenna pattern $(\hat{e}_\times, \hat{e}_+)$. The maximum L value is $L_{max} = (D \cdot H)^2/(2|H|^2)$. We can rewrite the maximum likelihood ratio as:

$$
L_{max} = \frac{1}{2} \frac{(D \cdot H)^2}{|H|^2} = \frac{1}{2} \frac{[(H + W) \cdot H]^2}{|H|^2} = \frac{1}{2} \frac{[H \cdot H]^2}{|H|^2} = \frac{1}{2} H \cdot H
\tag{4.8}
$$

where $W = (\mathbf{n}_1/\sigma_1, \mathbf{n}_2/\sigma_2, ..., \mathbf{n}_N/\sigma_N)$ is the normalised noise vector. Defining as SNR of a single detector $SNR_i^2 = \mathbf{h}_i^2/\sigma_i^2$ and as network $SNR^2 = \sum_{i=0}^{N} SNR_i^2 = H \cdot H$, the maximum value of L also corresponds to $L_{max} = SNR^2/2$.

To define the maximum likelihood, we have assumed the orthogonality between detector response and noise. This is however an oversimplification, as noise can

partially lie on the same plane identified by the antenna patterns of the DPF (f_+, $f_\times$). To mitigate this issue, `cWB` allows to apply different *regulators*, which consider the antenna pattern properties in the DPF, in particular the relation: $f_+ \geq f_\times$ (Drago, 2010). Regulators are the first constrained applied in `cWB` to the more standard likelihood approach. The regulators allow to reduce the impact of the cross component of the detector response H. While introducing such constraints usually considerably improves the background rejection, it also worsens detection and reconstruction of injected waveforms. The best compromise depend on the source sky location and more in general on the type of search.

To further improve the foreground-background discrimination, in `cWB` it is possible to set constraints on the GW polarisations. Such option allows to introduce signal assumptions, such as elliptical, circular or linear polarisations. For all sky searches, the same parameter permits to apply constraints on the signal chirality, lowering the noise impact without loosing the generality of the search. Two different chirality values are assigned, depending on the clockwise or anticlockwise evolution of the polarisations. Physical signals are expected to maintain the same chirality, while noisy events do not exhibit any particular rule.

4.2.2 Production stage

To permit a reliable analysis, while containing the computation cost, `cWB` analyses data, provided by the detector network, in segments of hundreds of seconds. The production stage of `cWB` consists in the following main blacks.

(i) **Data conditioning:** which includes procedures dedicated to the removal of noise lines, such as Linear Prediction Error filter (S. Klimenko and Mitselmakher, 2008) and Regression (Tiwari et al., 2015). It also includes a whitening procedure to account for the detector sensitivity dependence on frequencies;

(ii) **Time-frequency (TF) data representation:** as typical for unmodelled searches. The TF representation has therefore a considerable impact on the analysis.

The efficiency of the data decomposition depends on the match between the signal and transformation properties. The data are elaborated in the TF regime adopting the Wilson-Daubechies-Meyer (WDM) transformation (Necula et al., 2012a). The WDM TF transformation allows the definition of two complete representation of the same event. A WDM transformation is computed to the data stream collected by each detector. The event components obtained with this process are called pixels; each TF transformation requires the definition of time (pixels' width) and frequency (pixels' high) resolutions (liked by the relation $\delta t \ \delta f \sim 1/2$), which define a specific level of the decomposition. Usually a single event representation is constructed analysing different levels and selecting the most energetic pixels. After this first energy selection, cWB applies constraints based on the coincidence of such pixels between the data collected by the detectors in the network, testing different possible source locations. The pixels surviving such cut, define a cluster. The likelihood analysis is then newly applied to the entire cluster. At this stage, pixels belonging to different levels are collected in superclusters, on which the likelihood approach is applied again. The likelihood analysis is then applied to the best representation of the data, which can be composed by a selection of pixels belonging to the most descriptive level (optimal level) or by the most energetic components collected in the whole analysis. This latter case is particular important for events whose spectral characteristics significantly evolve in time. Indeed in such cases, which include signals generated during CBCs, this approach considerably reduces the number of pixels necessary to describe the event, enhancing the contrast between signal and noise components and therefore improving the GW description;

(iii) **Background statistics:** to evaluate the occurrence of glitches and therefore estimate the significance of GW candidates, cWB compute time shifts between the different data stream of the instrument, increasing the effective operative time and assuring not real signals (though triggers generated, in one of the

detector, by astrophysical events cannot be excluded a priori). To avoid the presence of real coincident signals, the time shifts have to account for both the contributions due to the distance between the detectors and the expected GW maximum duration. Shifts are performed on each segment of data, temporally translating $N - 1$ data streams by multiples of an adequate time. These shifts are called *lags*. Segments collected in different periods are also combined and used to increase the statistics, defining the so called *superlags*;

(iv) **Waveform parameter inference:** which includes the signal reconstruction as well as the estimate of the source sky localisation.

4.2.3 Post-Production stage

The maximum likelihood approach discriminates glitches from signals in the assumption of Gaussian and stationary noises. However real data are affected by disturbances which might not exhibit these qualities, lowering the effectiveness of the likelihood approach in rejecting background events. To boost the analysis, `cWB` is equipped by upstream and downstream procedures to improve the rejection of noise artefacts. Upstream methods include vetoes and data quality flags, which tag the data according to the simultaneous environmental disturbances recorded in the auxiliary channels and their impact. Downstream procedures are instead applied at the post-production stage. Information collected in the production stage are analysed to infer statistical properties of GW candidates. New variables are introduced to further qualify the final list of events and so improve the overall `cWB` performances in discriminating glitches against GW signals. The *network correlation coefficient* and the *effective correlated SNR* are the parameters most effective in the signal - noise classification. The thresholds applied on these quantities vary according to the characteristics of the considered detector network and desired search.

Network correlation coefficient In the DPF, we can represent the maximum

likelihood ratio L_{max} as an $N \times N$ matrix:

$$L_{max} = \frac{1}{2}\left(D \cdot \hat{e}_+\right)^2 + \frac{1}{2}\left(D \cdot \hat{e}_\times\right)^2 = \frac{1}{2}\sum_{i=1}^{N}\sum_{k=1}^{N}\left(D_k e'_{+k} D_i \hat{e}_{+i} + D_j \hat{e}_{\times j} D_i \hat{e}_{i\times}\right) = \sum_{i,k=1}^{N} L_{ik}$$

$$(4.9)$$

where $\hat{e}_+$ and $\hat{e}_\times$ are the normalised antenna pattern vectors and N is the number of detectors in the network. By summing the off-diagonals matrix elements, we can evaluate the *coherent energy* E_c of the GW candidate: $E_c = \sum_{n \neq m} L_{mn}$ and adopt this quantity to define the *network correlation coefficient* :

$$cc = \frac{E_c}{E_c + E_{null}} \tag{4.10}$$

where $E_{null} = |D - H|^2$ is the square of the reconstructed noise energy. The network correlation coefficient measures of the coherent energy of each event against its total.

Effective Correlated SNR Another key parameter to discriminate noise from signals is the *effective correlated SNR*, which represents a coherent version of the standard SNR (Abbott et al., 2016e; Vinciguerra et al., 2017a):

$$\rho = \sqrt{\frac{2\langle E_c \cdot cc\rangle}{N-1}} \propto \sqrt{cc\sum_{k=1}^{N} SNR_k^2} \tag{4.11}$$

The introduction of cuts on the network correlation coefficient cc and the effective correlated SNR ρ are particularly effective in discriminating noise from signal populations. Indeed from noise fluctuations, we expect only a very small fraction of glitches to present both high excesses of energy and correlation.

4.3 Artificial Neural Networks for signal recognition

Going to the problem...

Non stationary and non Gaussian noise tails are the main limitation of burst umodelled searches. Despite noise attenuation which characterised the second generation of detectors, the rate of such disturbances remains much higher than the rate of the astrophysical detectable GWs. To better discriminate glitches from GW signals, standard `cWB` analyses separate the raking of GW candidates characterised by well known noise properties from the remaining ones. For example to account for the marked presence of glitches at low frequencies, `cWB` distinguishes between events characterised by a central frequencies smaller or larger than a certain threshold f_{th}, which depends on the instrument sensitivities (one of the 2 rules applied for C1 class, as explained in (Abbott et al., 2016e)). In view of O1, during which only weak constraints based on the coherence analysis could be placed because of the operation of only two GW-detectors, the analysis of `cWB` was developed to maximise the sensitivity to chirping signals without loosing the generality of the search. To face the challenges posed by the early advanced detector network, the default ranking separation, has been further developed toward the construction of a signal classification procedure aimed in boosting the significance of GW candidates in burst searches. The main idea consists in recognising different signal classes and assigning them the correspondent specific subset of False Alarm Rate. As our first case study, for proving the effectiveness of a signal classification approach in unmodelled searches, we aim at the identification of time-frequency traces consistent with GWs emitted during CBCs. Because of their chirping peculiar feature, such signals are indeed difficult to mimic coherently by uncorrelated disturbances in multiple detectors. Two different approaches have been tested on `cWB` to the identify chirp-like signals on the data: (i) a *chirp-mass estimation* and (ii) a *TF pattern recognition* performed by artificial neural networks.

Machine Learning

Several efforts have been devoted to the development of data analysis procedures, dedicated to the improvement of the signal-noise discrimination. In the last years, *machine learning* techniques have become more and more popular within the GW community. Indeed, their flexibility and classification/identification potentialities make them the perfect tools for spotting similarities and unknown relationships between input parameters.

Machine learning (Nilsson, 1998) is the field of computer science that allows programs to learn without an explicit predefined structure. The key property of such tools consists in learning from examples. The advantages of adopting such techniques are: (i) the possibility of efficiently handle big data, difficult to treat with explicit procedures; (ii) the possibility to extract complicate and/or unknown relations (*data miming* and *data interpretation*); Different types of algorithms have been developed to address different tasks; the most popular are Boosted Decision Trees, Suport Vector Machines and Artificial Neural Networks (ANN) (for more details see (Kotsiantis et al., 2007)).

4.3.1   Artificial Neural Network

In this section are summarised some basic concepts concerning artificial neural networks, further details can be found in (Kotsiantis et al., 2007),(Rojas, 2013), (Rota), (Golfarelli, 1718). ANNs resemble biological neural networks, complex structures composed by cells, called *neurons*. They are composed by calculation units (called indeed neurons) which calculate a weighted sum of the inputs and use it as independent variable of an activation function, to determine their response. The key property of such algorithms is their ability of learning from examples. The learning processes consists in changing the weight values associated to each connection (synapses) according to an optimisation procedure.

The main properties of ANNs derive from the network structure and from the neuron properties:

- the network behaviour of ANNs is mainly determined by the strength of the synapses and the type of connections between neurons;

- neurons are characterised by: (i) a threshold applied as a offset to the input weighted sum in each neuron; (ii) an activation function, which determines the output signal.

The strength of each connection as well as the neuron thresholds are defined by the training procedure. This is based on a set of examples called *training set*, through which the algorithm adapts, generalising the input interpretation. We are particularly interested in supervised learning procedures, where samples belonging to the training set are associated to the desired ANN outputs. These quantities are used to evolve weights and neuron thresholds, by minimising the *error (or cost) function*, which estimates the distance between the target and present ANN outputs. Construction of associations and functions for data interpretation are among the most popular uses of ANNs. In the project presented in the following, we adopt ANNs for classification/regression purposes. In particular, we apply ANNs to mitigate the impact of non Gaussian noise tails testing a first case of signal classification, aimed to recognise chirping TF traces consistent with CBC emissions.

4.3.2 Multilayer perceptron

For our first application, we adopt feedforward ANNs (i.e. ANNs without cyclic connections between neurons), structured in multilayer perceptrons. Multilayer perceptrons (Kotsiantis et al., 2007) consist in a particular subset of ANNs, where neurons are grouped in structures called *layers*. For the purpose of the project, the aim of ANNs is to approximate a function able to correctly classify events belonging to different classes. The final characterisation of an ANN is lead by the discrete series of training data, the learning algorithm, the architecture and the activation function, usually leaving as random component the initial weight values. In principle the discretisation of the data leaves an infinite number of possible functions which can correctly interpret the input-output couples of the training set. The challenge in

the ANN design is to find most suitable number of training examples and epochs of weight updates to allow a correct, not overfit, approximation of the target function.

Perceptron

A perceptron is a calculation unit, resampling a biological neuron, which allows binary classification by solving linear systems of inequalities. Given an input vector $x{\in}\mathbb{R}^n$, the corresponding weight vector $w{\in}\mathbb{R}^n$ and the number θ, which sets an offset on the weighted sum of the input values, the neuron output y is provided by the the equation:

$$y(x) = g\left(\sum_{i=1}^n w_i x_i - \theta\right) \equiv g\left(w^T x - \theta\right) \tag{4.12}$$

Here x and w are respectively input and weight vectors, while $g(x \mid w, \theta) : \mathbb{R}^n \to \mathbb{R}$ represents the activation function of the neuron (in our analysis a sigmoidal-function). For a set of points linearly separable in a n dimensional space, the classification can always be performed with the definition of $n-1$ dimensional hyperplane $H = \{x{\in}\mathbb{R}^n : w^T x = \theta\}$. Events belonging to two categories, say signals S and background B, can therefore be distinguished evaluating the sign of $w^T x - \theta$. Formally the problem can be solved if, given a input vector $x = \{x_1, ... x_n, -1\}$, there exists a vector $w = \{w_1, ... w_n, \theta\}$, with $x,\ w \in \mathbb{R}^{n+1}$, which satisfies the system:

$$\begin{aligned} w^T x > 0 \quad for \quad x{\in}S \\ w^T x < 0 \quad for \quad x{\in}B \end{aligned} \tag{4.13}$$

Perceptron are algorithms defined by supervised learning. The training set T is composed of P input- output couples:

$$T = \{(x^p, t^p), \quad x^p{\in}\mathbb{R}^n, \quad t^p{\in}\{-1, 1\}, p = 1, ..., P\} \tag{4.14}$$

where t is the desired output of the neuron (*target*). The basic idea of learning processes consists in updating the weight vector w to correct for events wrongly

classified. Given the linearly separable subsets of T ($S = \{x^p : (x^p, t^p) \in T, \quad t^p = 1\}$ and $B = \{x^p : (x^p, t^p) \in T, \quad t^p = -1\}$), a common approach adopted to identify the hyperplane H, which separates S from B, consists in updating the w values according to the cost/error function derivatives. Perceptrons are effective classifiers for linearly separable subsets of events, however they cannot correctly interpret more complicated functions or logical relations (such as for example the Exclusive OR).

Multilayer perceptron

Perceptron limits have pushed for the development of more elaborated structures, finalised to address a wider range of problems, including performing classification of sets non linearly separable. One of the most successful approaches consists in grouping perceptrons in ordered structures, called *layers*, to define *Multilayer perceptrons* (MLPs). The architecture of multilayer perceptrons is defined by the following types of *layers*:

input layer composed of n nodes associated to the n inputs and characterised by a transfer function equal to 1 (no calculation performed). The input layer aim is to define links between the input quantities and the perceptrons of the following layer;

hidden layers composed of calculation units organised in successive groups and aimed to elaborate most of the information carried by the output-input couples;

output layer composed of K perceptrons which compute the last elaboration of data and finally define the network outputs.

In multilayer perceptrons only neurons belonging to two successive layers are connected between each others, as shown in the example of MLP reported in figure 4.1. Each connection is identified by two indexes, j and i, respectively associated to the calculation-unit of the layer $l \in [1,..L]$ and the neuron or node of the previous layer.
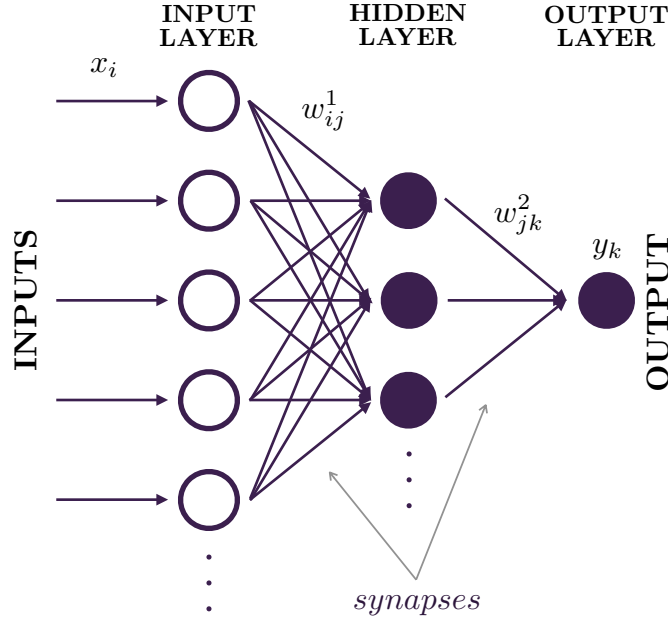
Figure 4.1: Example of multilayer perceptron defined by a single hidden layer.

At each j unit of each hidden layer, the algorithm calculates:

$$
\begin{aligned}
a_j^{(1)} &= \sum_{i=0}^{n} w_{ji}^{(1)} x_i, \quad z_j^{(1)} = g_j^{(1)}\left(a_j^{(1)}\right), \quad w_{j0} = \theta_j, \quad x_0 = -1, \quad l = 1 \\
a_j^{(l)} &= \sum_{i=0}^{N^{(l-1)}} w_{ji}^{(l)} z_i^{(l-1)}, \quad z_j^{(l)} = g_j^{(1)}\left(a_j^{(l)}\right), \quad w_{j0} = \theta_j, \quad z_0^{(l-1)} = -1, \quad l > 1
\end{aligned}
\tag{4.15}
$$

where N^l are the number of neurons in the l layer and the activation function can differ from layer to layer.

The performances in data interpretation of MLPs depend from their architecture (number of layers $L + 1$ and perceptron per layer $N^{(l)}, \quad l = 1, ..L$), as well as from the applied *learning method*. The former determines the number of weights w_{ij}^l, while the latter sets the efficiency of the algorithm in reaching "optimal" values. To be efficient, these parameters should however be set accounting for the dimension of the training set $(T = \{(x^p, t^p), \quad x^p \in \mathbb{R}^n, \quad t^p \in \mathbb{R}^K, p = 1, ...P\})$, i.e. the P number of the examples used in the learning procedure. The training process consists in a rule which defines the weight updates, targeting the minimum of the error function.

To address the signal classification in GW transient searches, we apply the toolkit

for the multivariate analysis (TMVA) provided by ROOT. In such toolkit, the weight values are initially assigned by default adopting a uniform distribution in the range $[-0.5, 0.5]$.

4.4 Enhancing the significance of gravitational-wave bursts through signal classification

The quest to observe gravitational-waves challenges our ability to discriminate signals from detector noise. This issue is especially relevant for transient gravitational-waves searches with a robust *eyes wide open* approach, the so called all-sky burst searches. Here we show how signal classification methods inspired by broad astrophysical characteristics can be implemented in all-sky burst searches preserving their generality. In our case study, we apply a multivariate analyses based on artificial neural networks to classify waves emitted in compact binary coalescences. We enhance by orders of magnitude the significance of signals belonging to this broad astrophysical class against the noise background. Alternatively, at a given level of mis-classification of noise events, we can detect about 1/4 more of the total signal population. We also show that a more general strategy of signal classification can actually be performed, by testing the ability of artificial neural networks in discriminating different signal classes. The possible impact on future observations by the LIGO-Virgo network of detectors is discussed by analysing recoloured noise from previous LIGO-Virgo data with coherent WaveBurst, one of the flagship pipelines dedicated to all-sky searches for transient gravitational-waves.

4.4.1 Introduction: signal classification for background rejection

General searches for transient gravitational-waves of generic waveform (GW *bursts*) have been accomplished exploiting the full sensitivity bandwidth of the Laser Interferometer Gravitational-Wave Observatory (LIGO) (Aasi et al., 2015a; Abbott

et al., 2009a) and Virgo (Acernese et al., 2014; Accadia et al., 2012) detectors. This type of *all-sky* search has been performed by analysing the network detector data with coherent methods (Abadie et al., 2010a, 2012a) looking for signals lasting from *ms* to *s* scale. These methods successfully identified the first detected gravitational-wave, GW150914 (Abbott et al., 2016d,e). In burst searches, the main factor which limits the statistical confidence of a gravitational-wave candidate comes from non Gaussian noise outliers of single detectors, which may accidentally mimic a coherent response of the network. The implemented strategies to improve the capability of discriminating between signals and noise include both upstream and downstream methods. Upstream methods include data quality flags and vetoes at single detector level (Aasi et al., 2015b; Abbott et al., 2016c) to clean the input of the network analysis. Downstream methods apply post processing procedures such as splitting the end results in a few separate frequency bands: to account for the most evident inhomogeneities of non Gaussian noise tails, any candidate belonging to a specific frequency band is thus ranked against the noise outliers characteristic of the same band.

coherent WaveBurst (cWB) (Klimenko et al., 2016) is the flagship pipeline aiming at all-sky burst searches on LIGO-Virgo data using minimal signal assumptions. cWB has already been used for the analysis of data collected by the first generation of interferometers (Drago, 2010; S. Klimenko and Mitselmakher, 2005) and during the first observation run of Advanced LIGO, O1. In September 2015 cWB was the first pipeline to identify GW150914 (Abbott et al., 2016e). cWB is based on a likelihood maximisation of the coherent response of the network, which also allows the reconstruction of the most significant signal characteristics (Drago, 2010, 2009). To further reduce the false alarm probability at a reasonable cost in terms of false dismissals, additional procedures have been implemented. These procedures include simpler tests, such as the rejection of candidate signals in case of unusually high energy disbalance at different detectors, as well as more elaborate methods. Among

them, `cWB` uses procedures for constraining the polarisation and direction of detectable signals, since noise spectra and directional sensitivities affect the fraction of detectors which significantly contribute to the coherent response of the network. All the strategies mentioned above preserve the degree of universality, typical of burst searches.

The performance of the pipeline can also take advantage of priors on the target signals; however, this is accomplished at the cost of a loss of generality of the search. Different versions of `cWB` pipeline have been tailored for, e.g., the search for coalescences of intermediate mass binary black holes (Abadie et al., 2012d) or of highly eccentric binary Black Holes (Tiwari et al., 2016).

The scope of this work is to demonstrate how signal classification methods can complement all-sky burst searches to enhance the significance of selected signal classes without losing the generality of the search. The proposed signal classification method is based on machine learning techniques (I. Bratko and Kubat, 1999) to identify such signals against the non Gaussian noise outliers recorded in LIGO-Virgo observations. The signal vs. noise discrimination based on the use of machine learning techniques on single detector data has been discussed in several papers. For instance (S. Rampone and Pinto, 2013; Powell et al., 2015; Zevin et al., 2016) address the classification of transient noise outliers and (Acernese et al., 2005) the whitening of the detector output. A signal recognition approach based on boosted decision trees has been tested for the case of a burst search triggered by astrophysical events in a network of detectors (Adams et al., 2013). Similarly, in (Baker et al., 2015), the authors developed a multivariate classification with random forests in the context of matched filtering searches for high-mass black hole binaries.

The novelty of our work lies in its integration into all-sky burst searches and on the implementation of new strategies for signal classification, taking advantage of

pattern recognition in the framework of the time-frequency (TF) representation of the candidate signals. The latter is accomplished by averaging the response of more artificial neural networks (ANNs), as explained in section 4.4.2. As a case study, we focus on the recognition of signals consistent with coalescences of compact binaries (section 4.4.3). Section 4.4.4 and section 4.4.5 discuss respectively the effectiveness of the ANN analyses of the TF representations and its robustness against changes in the target signal distribution. Section 4.4.6 explores the potentiality of a further multivariate step: we test a new ranking statistic built by combining the discrimination variables, adopted in a standard `cWB` analysis, with the output parameter describing the recognition of time-frequency patterns. By comparing the receiver operating characteristics, we show the achievable enhancement of GW burst searches through our signal classification strategies. In section 4.4.7, we give more general remarks about the impact of signal classification approaches on all-sky searches for GW bursts.

4.4.2   Methodology

With the purpose of enhancing the significance of GW bursts in all-sky searches, we complement the standard analysis pipeline `cWB` with a new discrimination variable based on ANNs, dedicated to signal classification according to their TF characteristics. In its standard operation, `cWB` uses two main post-processing statistics to discriminate gravitational-waves from noise artefacts (glitches): the network correlation coefficient (cc) and the effective correlated SNR (ρ) (Abbott et al., 2016e). The latter is used to rank candidate events and assign them a false alarm rate. The former measures the consistency of the candidate with a coherent response of the network to a GW. `cWB` uses TF transformations (Necula et al., 2012a) at different resolutions (or levels) and defines the TF characterisation for each candidate (Vedovato et al.), collecting the least number of TF pixels describing the event from the available resolutions.

To perform the ANN classification, a post-processing algorithm converts the TF

representation of the whitened data into a frame, made by 8×8 pixels. The scalar amplitude associated to each pixel is calculated from the fraction of total likelihood included in the portion of the TF representation correspondent to the pixel. [1] (see fig. 4.2). Each frame carries no information about the absolute scale of the candidate strength, duration or frequency band and keeps only the uncalibrated shape information of the candidate's TF trace (for more details see 4.4.8).

The 64 entries of the 8×8 frame feed the ANNs dedicated to the classification
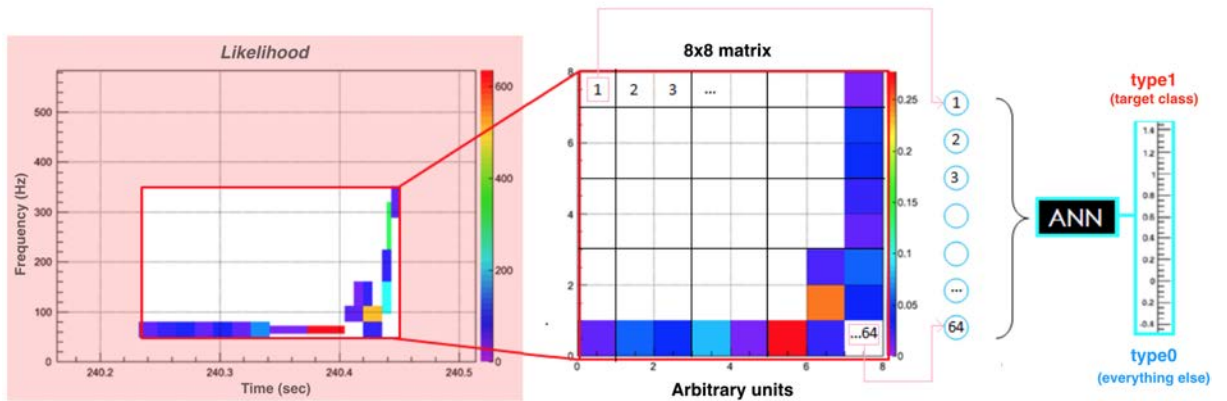
Figure 4.2: Schematic representation of the proposed event classification. The procedure is based on the reconstructed time-frequency map of candidates. ANNs are trained to produce an output number close to 1 for events are classified as belonging to the target distribution, and close to 0 otherwise. Our procedure does not constrain the output value to be limited to [0,1] and overflows and underflows are possible.

of the TF pattern. ANNs are tools composed of calculation units (neurons - represented by circles in fig. 4.3), connected together by synapses (represented by lines in fig. 4.3), which acquire specific values (weights) accordingly to a supervised training procedure[2] (see (Stergiou and Siganos) and references therein). The ANNs adopted for this study are multilayer perceptrons defined within ROOT (Vinciguerra, 2014a)

---

[1]In the algorithm dedicated to the definition of the frame, we also allow the rejection of late TF pixels with low likelihood. Starting from the pixels that appeared at the latest times, the procedure, which defines the 8×8 frame, discards a fraction of the TF pixels, corresponding to at most 10% of the total likelihood. This selection prevents the occurrence of problematic distortions of patterns in the 8×8 frames. Noisy pixels selected after the merger time would indeed shrink and move the characteristic trace left by chirping events on the 8×8 frame. This operation is particularly useful for the classification in real noise. In fact, it favours a neater TF map by rejecting any weak structures appearing after the merger time, which will then dominate the last column of the frame (see fig. 4.2).

[2]A supervised training procedure consists in an optimisation rule tailored to minimise the error between actual and desired output over the selected target and complementary sets of signals.

(the object oriented framework developed at CERN). Every ANN is composed of an input layer, fed by the 8×8 frame, and of 3 hidden layers, requiring the definition of about 2×10^3 synapses. Each ANN is trained against a set of $\sim 10^4$ target signals (type1 class) and a set of $\sim 10^4$ complementary events (type0 class) composed of either noise glitches or signals belonging to alternative classes. The classification rule consists in obtaining output values close to 1/0 for elements of type1/type0 class respectively. For more details on the structure and training procedure used for the present study, see 4.4.8 and (Vinciguerra, 2014a).

We mitigate the impact of the statistical fluctuations intrinsic to the ANN definition, such as the initial weight values and the samples included in the training set, by averaging the output of 4 (unless otherwise specified) independently trained ANNs and so introducing the *ANN average*, as shown in figure 4.3. Every considered ANN is built with the same fixed training procedure, but each of them is trained over an independent set of events sampled from the same distributions. The time required for the definition of a single ANN varies by several orders of magnitude according to the adopted training. However, once defined, ANNs are able to quickly evaluate `cWB` triggers, providing an effective discriminating variable, as illustrated in figure 4.4. In this preliminary test, we considered a population of target signals (type1) made by compact binary coalescences (see table 4.3) and a population of accidental coherent responses of the initial LIGO-Virgo network of detectors (network glitches, type0). The former is produced by software injections of signals in a few days of initial LIGO and Virgo data from S6D-VSR3 runs (Abadie et al., 2012a; Aasi et al., 2015c), recoloured according to the early phase spectral sensitivity of advanced detectors (Abbott et al., 2016j). The set of network glitches is produced by running the standard `cWB` all-sky search on the same recoloured data streams after applying a set of time-shifts among different detectors so to cancel any physical correlation present. The use of actual data is necessary to model the non Gaussian noise features that dominate the performances of all-sky burst searches. Figure 4.4 shows that ANNs
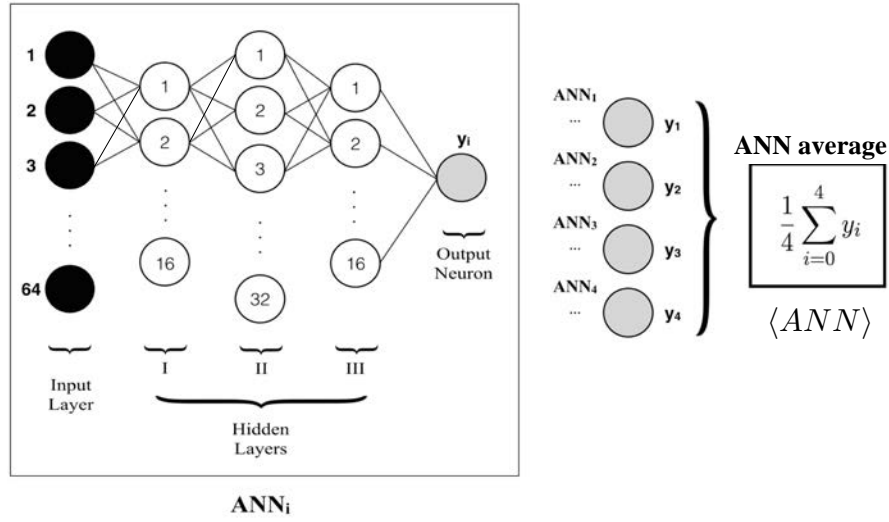
Figure 4.3: Schematic representation of the algorithm adopted to obtain the ANN average. In the square it is summarised the structure of each ANN: the black filled circles compose the input layer, while the empty ones represent elaborating units. Each of them sums the output values of the previous layer, by weighting them with the correspondent synapse's (lines) strength. The new classification parameter is obtained by averaging the result of 4 independent ANNs (ANN average).

can be effective in discriminating these target signals from network glitches, to a much more efficient degree than the more general criteria used by `cWB`.
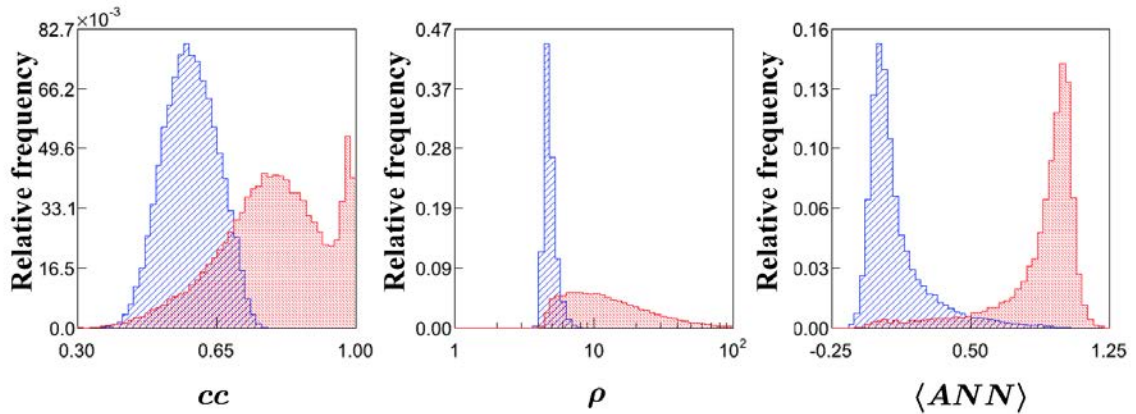
Figure 4.4: Distributions of 5×10^4 target CBC signals (red, see table 4.3) and 5×10^4 network glitches (blue) as seen in different analysis variables.
y axis: fraction of events in the x bin.
x axis, from left to right: network correlation coefficient, correlated SNR and average of 4 trained ANN outputs. The first two are the main test statistics used by `cWB` in GW burst searches.

4.4.3   Case study: classification of chirping signals

In this section we focus on the classification of a specific signal class, emitted by compact binary coalescences. The results will be highlighted in section 4.4.4 while their robustness will be discussed in section 4.4.5, proving that the enhancement provided by our classification still holds over a much wider signal parameter space than that used to train the ANNs.

Type1 or target signal class

The results of the first observing run of advanced LIGO (Abbott et al., 2016b) and the measured rate for binary black hole (BBH) mergers of $9 - 240 \ Gpc^{-3}yr^{-1}$ (Abbott et al., 2016g) confirm that compact binary coalescences are the most numerous sources for current ground based detectors. In this study, we focus on the classification of the inspiral phase of the binary evolution. During the inspiral, the gravitational emission is mainly determined by the chirp-mass $\mathcal{M} = \frac{(m_1 m_2)^{3/5}}{(m_1+m_2)^{1/5}}$, where m_1 and m_2 are the masses of the two companions. The chirp-mass drives:

- the frequency evolution $\dot{f} \propto \mathcal{M}^{5/3} f^{11/3}$ of the gravitational-waves, which sets the chirping behaviour commonly associated to these signals;

- the gravitational-wave strain amplitude, which in time domain is: $\mathcal{A}(t) \propto f^{2/3} \mathcal{M}^{5/3}$;

- the time spent in the most sensitive part of the spectral sensitivity of the detectors, which scales as $t_{det} \propto \mathcal{M}^{-5/3}$. This time is also strongly dependent on the noise spectral density (PSD) of detectors at lower frequencies.

Since the classification procedure depends on these properties, we investigated different distributions of chirp-masses. In particular, we mainly tested two signal populations:

- a *low-mass* distribution (see table 4.2) composed of signals characterised by a clear chirping feature in the TF representation, which is dominating the detectable signal within the spectral sensitivity of the detectors.

Mass distribution	uniform in M_{tot} and m_1/m_2
Total mass range $[M_\odot]$	$M_{tot} \in [3, 50]$
Mass ratio range	$m_1/m_2 \in [1, 11]$
Distance range d **[Mpc]**	$\sim [70, 225]$
number of Shells* (Mazzolo, 2013)	3
Distribution in each shell	uniform in volume

Table 4.2: main parameters of the **low-mass CBC signal distribution**.
* The subdivision in shells is performed to decrease the computational load while ensuring more homogeneous statistical uncertainties on detection efficiency. The reference shell range is $[100 - 150]$ Mpc and by rescaling signal amplitudes we populate the two contiguous shells ($[\sim 70, 100]$ Mpc and $[150, 225]$ Mpc).

- a *wide mass range* distribution (see table 4.3), composed of a CBC population including more massive systems and therefore shorter detectable signals, in which the inspiral phase plays a weaker contribution within the spectral sensitivity considered in this study (early phase of advanced detectors).

Mass distribution	uniform in $log(m_1)$, $log(m_2)$ *
Mass range $[M_\odot]$	$m_{1,2} \in [1.5, 96.0]$, $M_{tot} \in [3.0, 136.0]$
Distance range d **[Mpc]**	$\sim [45, 500]$
number of Shells** (Mazzolo, 2013)	6
Distribution in each shell	uniform in volume

Table 4.3: Main parameters of the **wide-mass range signal distribution**.
* As case (i), assumed in (Abbott et al., 2016b) to calculate rate from astrophysical populations. ** As described in table 4.2, but rescaling signal amplitudes to populate five contiguous shells from ~ 45 Mpc to ~ 500 Mpc. Detection efficiencies are listed in table 4.4.

As CBC signals models, we adopt EOBNRv2 waveforms (Pan et al., 2011; Mino et al., 1997). They rely on the effective-one-body (EOB) formalism and describe all the phases (inspiral, merger and ring-down) of the coalescence. The actual distributions of the detected signals used in this study are a convolution between the signal population (from table 4.2 or table 4.3) and the `cWB` detection efficiency. Figure 4.5 illustrates the selection effect due to this convolution on the *wide-mass-range signal distribution* (table4.3). As expected the detection pipeline is more sensitive to louder signals, i.e. for more massive systems (fig. 4.5). Indeed the gravitational-wave amplitude scales as $\mathcal{A}(t) \propto f^{2/3} \mathcal{M}^{5/3}$ and $\mathcal{M}(M, q) = Mq^{3/5}(q+1)^{-6/5}$, where $q = m_1/m_2$ is the mass ratio. Table 4.4 lists the overall detection efficiencies of `cWB`

in the different shells. As expected, the pipeline efficiency decreases as the distance range increases.
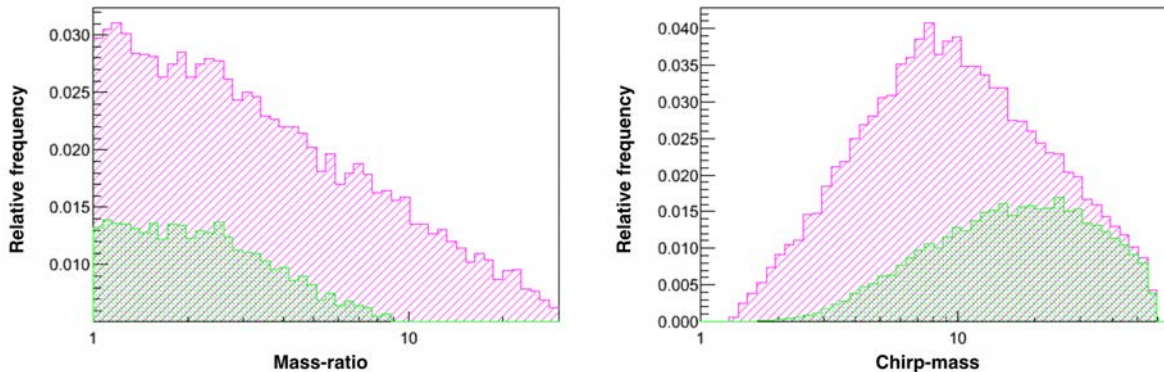
Figure 4.5: Event distribution of injected signals (violet) and reconstructed by `cWB` (green) for mass-ratio (left panel) and chirp-mass (right panel). `cWB` pipeline reconstructed $\sim 6.5 \times 10^4$ out of about 1.7×10^5 signals, injected according to table 4.3.

Shell distance range [Mpc]	Efficiency %
[$\sim$45,$\sim$65]	72.3 ± 0.3
[$\sim$65,100]	57.8 ± 0.2
[100,150]	42.5 ± 0.1
[150,225]	29.2 ± 0.2
[225,$\sim$340]	18.3 ± 0.3
[$\sim$340,$\sim$505]	10.2 ± 0.1

Table 4.4: `cWB` detection efficiency per shell (Mazzolo, 2013), for CBC signals belonging to the *wide-mass-range distribution* (see table 4.3 and fig. 4.5)

Type0 or alternative signal class

Our case study requires to test the classification procedure with respect to both network glitches and alternative GW signals. The network glitch distribution has been described in section 4.4.2. As alternative signal class we considered a mixture of GW signal waveforms widely used in simulations of GW burst searches, i.e. the BRST set described in (Abadie et al., 2012b), which includes Gaussian pulses, sinusoidal signals with Gaussian amplitude envelope as well as White-Noise-Bursts waveforms. Such alternative signals lack of a proper astrophysical model and therefore their amplitude distribution at earth has been modelled by scaling their nominal amplitude

value ($h_{rss} \equiv \sqrt{\int_{-\infty}^{\infty} h^2(t)\, dt} = 2.5 \times 10^{-21}$) by a grid of logarithmically distributed scaling factors (0.075, 0.15, 0.3, 0.6, 1.2, 2.4, 4.8, 9.6, 19.2), see (Abadie et al., 2012a; Drago, 2010). All these signals have been injected on the same recoloured data set used for the target signals injections.

4.4.4 Classification performance results

The main three tests of classification performances are summarised in table 4.5.

	type1 class	type0 class
Test 1	chirp-like GWs from *low-mass distribution* (table 4.2)	network glitches
Test 2	chirp-like GWs from *low-mass distribution* (table 4.2)	alternative BRST GWs
Test 3	chirp-like GWs from *wide-mass distribution* (table 4.3)	network glitches

Table 4.5: Summary of type1 and type0 classes used for the main three tests of classification performances.

The results are described in terms of the fraction of type1 (type0) events which are correctly classified (miss-classified) as belonging to the target class, $F_{1 \to 1}$ ($F_{0 \to 1}$) defined by:

$$F_{k \to 1} = \frac{1}{N_k} \sum_{i=1}^{N_k} \delta_i \tag{4.16}$$

Here N_k is the total number of tested events drawn from the k class (where $k = 1, 0$ for type1,type0) and δ_i is defined for each event i by:

$$\delta_i = \begin{cases} 1, & \text{if } \rho_i \geq \rho_{th} \ \wedge \ cc_i \geq cc_{th} \ \wedge \ \langle ANN \rangle_i \geq \langle ANN \rangle_{th} \\ 0, & \text{otherwise} \end{cases} \tag{4.17}$$

where the subscript "th" refers to threshold value on the related variable. Events with $\delta_i = 1$ ($\delta_i = 0$) are classified as belonging to the type1 (type0) class. Figures 4.6 and 4.8 summarise the results of each test and provide a comparison of the effects of the standard test statistics of `cWB` (correlated SNR and network correlation coefficient) with the ANN average. Each figure is made by four plots, whose *y-axis* reports $F_{1 \to 1}$

and $F_{0\to1}$ respectively in the top ones and bottom ones. The plots to the left show $F_{1\to1}$ and $F_{0\to1}$ as a function of the threshold on the correlated SNR, ρ_{th}. The red lines represent results obtained without applying a threshold on the ANN average (or $\langle ANN \rangle_{th} = -\infty$), while green curves show the effects of selected threshold values, namely $\langle ANN \rangle_{th} = \{0.0, 0.5, 1.0\}$. The plots to the right show $F_{1\to1}$ and $F_{0\to1}$ as a function of the threshold on the ANN average. Here blue curves are computed by applying different thresholds on the correlated SNR $\rho_{th} = \{5, 6, 7\}$. In all the plots a constant threshold on the network correlation coefficient is used, $cc_{th} = 0.6^3$, which is a common choice in standard GW burst searches (Abbott et al., 2016e). This cc threshold makes all the plotted fractions $F_{1\to1}$ and $F_{0\to1}$ lower than 1.

Test1: low-mass chirp-like GWs vs glitches

The first classification test aims to discriminate network glitches from chirp-like signals of the *low-mass* distribution (first line of table 4.5). The results on a population of 5×10^4 events per each type are reported in figure 4.6: both correlated SNR and the ANN average are effective classifiers but their joint use shows advantages. In fact, it is possible to enhance the statistical confidence with a much smaller cost in terms of detection efficiency. For instance, considering the left plots, at any selected value of ρ_{th}, by adding $\langle ANN \rangle_{th} = 0.5$ almost the same fraction of chirp-like signals are recovered, while the fraction of mis-classified glitches $F_{0\to1}$ is reduced by about one order of magnitude. The right plots lead to similar considerations. $F_{1\to1}$ depends very weakly on $\langle ANN \rangle_{th}$ as long as $\langle ANN \rangle_{th} \leq 0.8$, while the mis-classified fraction of events $F_{0\to1}$ drops substantially in the same $\langle ANN \rangle_{th}$ range.

Test2: low-mass chirp-like GWs vs alternative GWs

The signal classes considered for this test are the low-mass distribution and the BRST simulation set introduced as alternative signal class in 4.4.3. The results

---

[3]The adopted version of `cWB` usually runs with a cut on the cc of 0.6 or 0.7, the lower threshold allows the inclusion of more events which can therefore be analysed with the subsequent application of thresholds on ρ and $\langle ANN \rangle$.
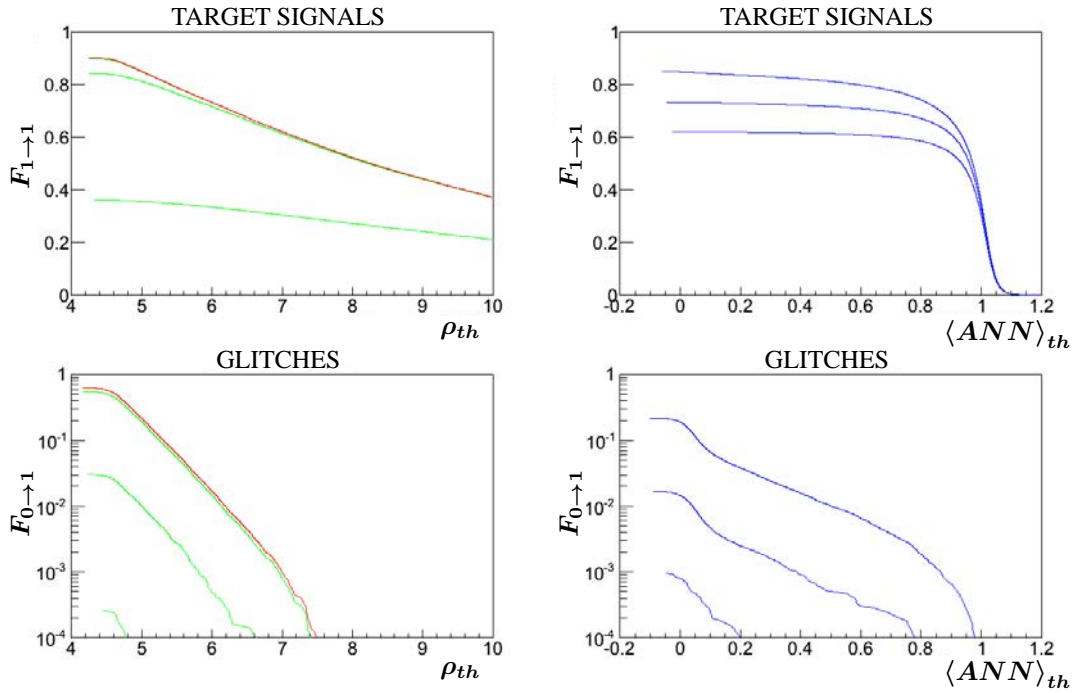
Figure 4.6: Left plots: $F_{1\to1}$ (top) and $F_{0\to1}$ (bottom) as a function of ρ_{th}. Right plots: $F_{1\to1}$ (top) and $F_{0\to1}$ (bottom) as a function of $\langle ANN \rangle_{th}$. A constant threshold for $cc_{th} \geq 0.6$ is used. In the left plots, the red lines show the results obtained by a standard `cWB` analysis, while the green curves use also the signal classification with $\langle ANN \rangle_{th} = \{0.0, 0.5, 1\}$, from top to bottom. In the right plots, the blue lines are computed for $\rho_{th} = \{5, 6, 7\}$ from top to bottom. The results refer to 5×10^4 events from the low-mass GW distribution and to the same number of network glitches.

of the classification are reported in figure 4.7, which shows the performances in terms of $F_{1\to1}$ and $F_{0\to1}$ with the same structure of figure 4.6. In particular, the right plots illustrate that the ANN average provides an efficient separation of the two GW populations, while the correlated SNR is instead agnostic with respect to the GW waveform class. In this test we selected a population of alternative GWs which are louder than the target GWs, to test an opposite condition with respect to what described in the previous subsection. The results are consistent with the ANN average being agnostic with respect to the loudness of the events, as it was designed to be. The chosen loudness of the alternative GW class carries no specific physical meaning, and the difference between $F_{1\to1}$ and $F_{0\to1}$ in the left plots cannot be used to classify type1 and type0 events in an actual GW search.
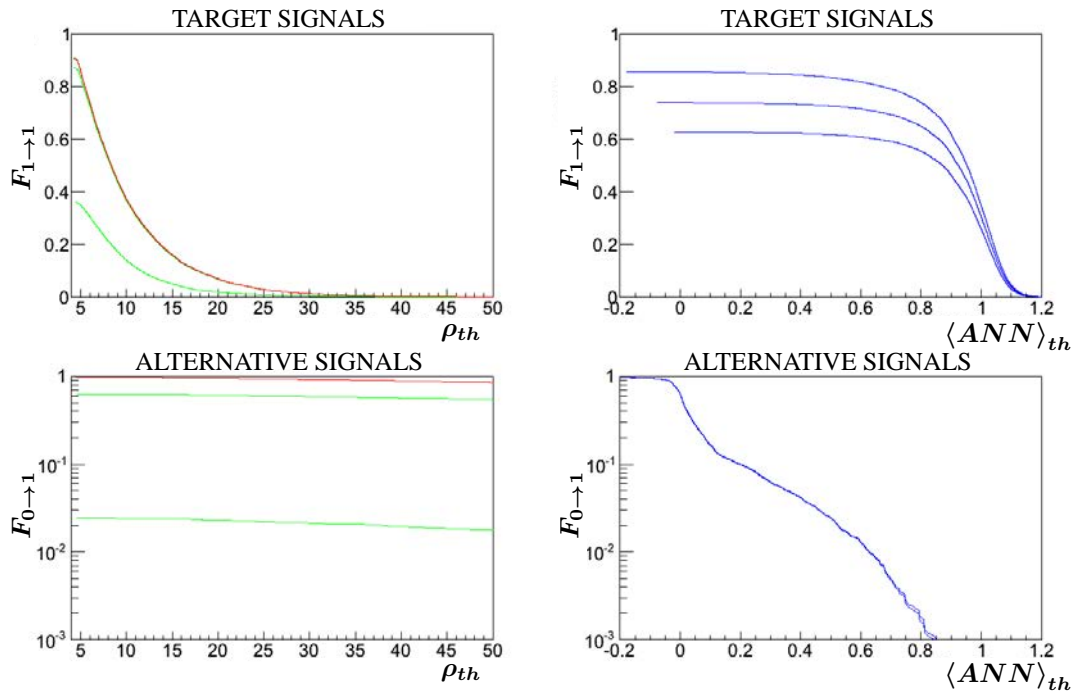
Figure 4.7: The figure is structured as figure 4.6. The right plots clearly illustrate that the ANN average provides an efficient separation of the two GW populations. Results refer to 10^4 type1 signals from the *low-mass* distribution and an equal number of type0 events from the alternative signal class, formed of BRST simulation. All the signals have been injected in recoloured detectors data. For this test, the ANN average is computed from the outputs of just 2 ANNs.

Test3: wide-mass chirp-like GWs vs glitches

The task of the last classification test is separating network glitches from chirp-like signals, drawn from the *wide-mass* range simulation (table 4.3). We report the results in figure 4.8. The plots of figure 4.8 and figure 4.6 exhibit very similar trends. The main difference is that $F_{1\rightarrow1}$ values are generally slightly higher, since the *wide-mass* event distribution includes also louder GWs. Instead, even if the chirping character is weaker for the wide-mass signals distribution, the results show that the ANNs can be trained to give comparable performances with respect to the low-mass case.
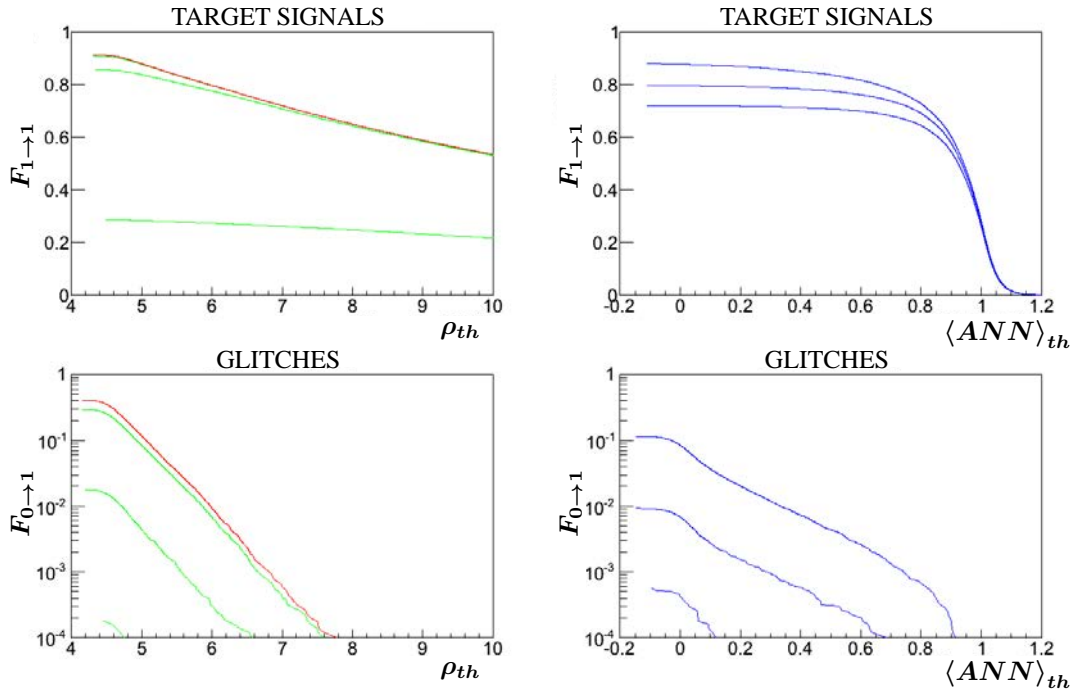
Figure 4.8: The image is structured as figure 4.6. The test is applied on 5×10^4 type1 signals from the *wide-mass* range distribution and 5×10^4 type0 events from the set of recolored network glitches.

4.4.5 Robustness

When the learning is supervised (Stergiou and Siganos), as in our case, the ANN structures are defined thorough procedures mainly driven by the selected type0 and type1 samples. Since the astrophysical distribution of chirp-like GWs is unknown, we need to investigate the robustness of our approach against biases in the training distributions. To this purpose, we consider Receiver Operating Curves ($\overline{ROC}$) computed as $F_{1 \to 1}$ vs $F_{0 \to 1}$ by varying the value of ρ_{th}, while keeping constant $cc_{th} = 0.6$, at selected $\langle ANN \rangle_{th}$ values. Figure 4.9 shows $\overline{ROC}$ curves for $\langle ANN \rangle_{th} = -\infty$ and $\langle ANN \rangle_{th} = 0.25$. The robustness is tested by comparing the improvement related to the application of the $\langle ANN \rangle_{th} = 0.25$ on the $\overline{ROC}$ in two different cases:

- classification results are performed on chirp-like signals belonging to the same type1 distribution used for the training;

- classification results are performed on chirp-like signals belonging to a distri-

bution different from that of the type1 used for the training.

Training set To test the robustness of the improvements obtained by the additional cut of the ANN average, we select 3 specific chirp-mass values to construct the ANNs that we test against a signal population characterised by a wider chirp-mass range. We build a simulation of GW emissions from *three fixed equal-mass binaries* $(10 - 10)M_\odot$, $(25 - 25)M_\odot$ and $(50 - 50)M_\odot$ (see table 4.8). With these three different systems, we consider GW events whose inspiral phase becomes shorter and shorter and the TF representation changes from the clear chirping trace to a less structured burst. Despite the arbitrary units of the 8×8 matrix used to feed the ANNs, increasing the total mass, and therefore the chirp-mass, entails shorter inspiral phase in relation to the total duration of the detected event, causing a degradation of the chirping feature also in the input matrix. On the other hand, increasing the total mass of the system allows to select less noisy pixels, since, given a fixed luminosity distance, the GW signal results lauder. From each of these three sources, we collect an equal number of reconstructed events to compose the training set for the target (type1) signals. The type0 training class is again defined with a sample of network glitches recoloured to mimic the spectral sensitivity in the early phase of the advanced detectors.

Testing sets The first one (i) is composed of samples of the same type1 and type0 populations used to define the training set just described, while the other one (ii) is formed by events drawn from the type1 and type0 classes of line 3 in table 4.5. For both cases, the tested type0 events are independent samples of the recoloured network glitches.

In figure 4.9, we first report the $\overline{ROC}$ curves obtained by applying the standard `cWB` analysis on the two tested sets (i) and (ii) where the included GW signals are sampled from:
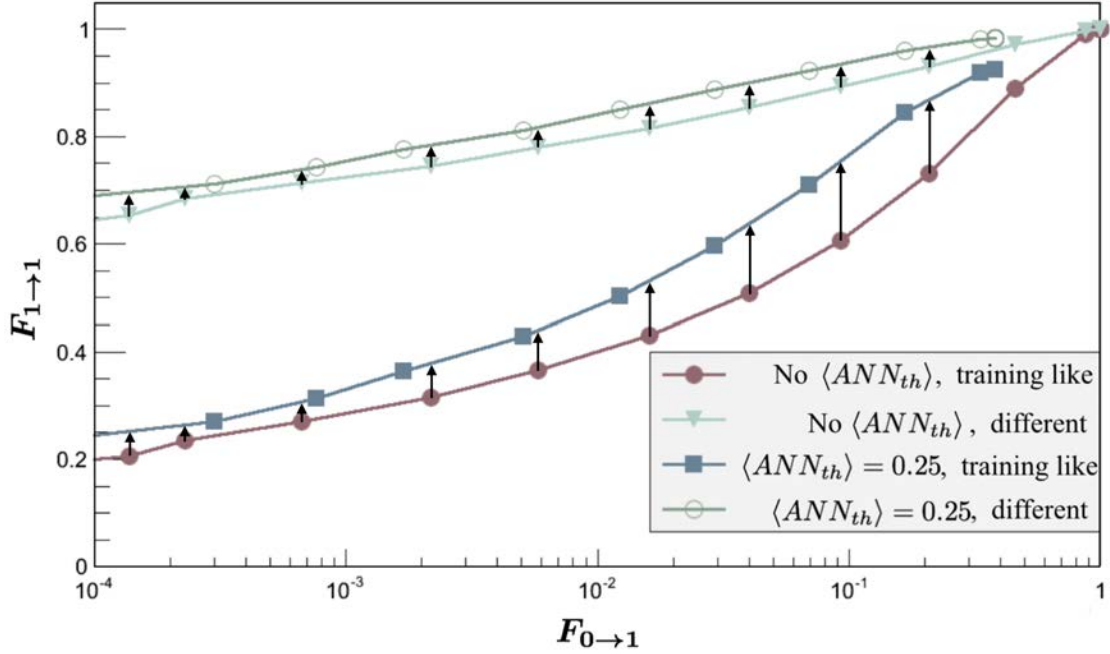
Figure 4.9: $F_{1\to1}$ vs $F_{0\to1}$ measured with (blue squares and green void circles) and without (red filled circles and teal triangles) the application of a threshold on the ANN average of 0.25. Symbols correspond to the same grid of ρ_{th} values. The red and blue curves (*matched*) are the results performed by testing the same signal population used to train the ANNs. The green and teal lines (*mismatched*) trace the $\overline{ROC}$ for a different test set built selecting CBC signals from *the wide-mass* range distribution. In both the cases, 5×10^4 CBC signals form the type1 class and the same number of network glitches form the type0 one.

(i) the *three fixed equal-mass binaries* $((10 - 10)M_{\odot}$, $(25 - 25)M_{\odot}$ and $(50 - 50)M_{\odot})$, reported as ight-filled-triangle blue curve;

(ii) the *wide-mass distribution*, reported as red-filled-circle curve.

We then perform the same analyses with the additional cut on $\langle ANN \rangle$ ($\langle ANN \rangle_{th} = 0.25$) (blue-filled-square and green-void-circles curves respectively correspondents to tests on (i) and (ii) sets), where the ANNs are in both cases trained on samples belonging to the *three fixed equal-mass binary* set. In figure 4.9, the improvements obtained by the introduction of the ANN average is marked with vertical black arrows. Despite cWB sensitivity considerably differ between the two set of signals, the improvement on the $\overline{ROC}$ achieved by implementing the threshold on the ANN average are significant and of comparable value in both testing sets. In this sense, figure 4.9 demonstrates the robustness of our approach against biases in the population-model.

Since the mismatched type1 testing set has a much wider range of chirp-masses than the matched one, we present the achieved results of figure 4.9 as representative of the effect produced by increasing the assumed volume in the parameter space of the source population.

4.4.6   Multivariate analysis

The last versions of the `cWB` pipeline include an estimation of the binary chirp-mass $\mathcal{M}_{est}$, computed as a best fit of the signal multi-resolution TF trace. To compute the fit, the algorithm considers all the pixels obtained with the TF decomposition at different levels, discarding the ones flagged as noise artifacts, according to the procedure defined in (Abbott et al., 2016e; V. Tiwari and Mitselmakher, 2015). Applying such post-processing analysis significantly improves the signal to noise discrimination achieved by `cWB` for CBC signals (V. Tiwari and Mitselmakher, 2015).

The joint distribution of the estimated chirp-mass and the ANN average (see fig. 4.10) demonstrates that the two variables are not fully correlated. This gives the opportunity to further improve the results by a joint use of these variables. In addition we can consider other signal parameters estimated by `cWB` to implement a multivariate analysis (MVA).

For the morphological discrimination we are interested in, we implement an additional classification stage, using four MVA-ANNs (see fig. 4.11). They are characterised by approximately 300 synapses and independently trained on $\sim 10^3$ events per class. The input quantities listed in figure 4.11 are then used to define a MVA-ANN average ($\langle MVA \rangle$). We evaluated the effectiveness of the multivariate approach by comparing the $\overline{ROC}$ obtained from this MVA ranking statistic (MVA-ANN average) with the one driven by different values of correlated SNR, accordingly to the standard `cWB` analysis. Figure 4.12 clearly demonstrates that `cWB`'s performances in discriminating signals from glitches can be considerably improved by adopting the MVA-ANN average as ranking statistic. In fact, at fixed $F_{1 \to 1}$ values $F_{0 \to 1}$ is lowered
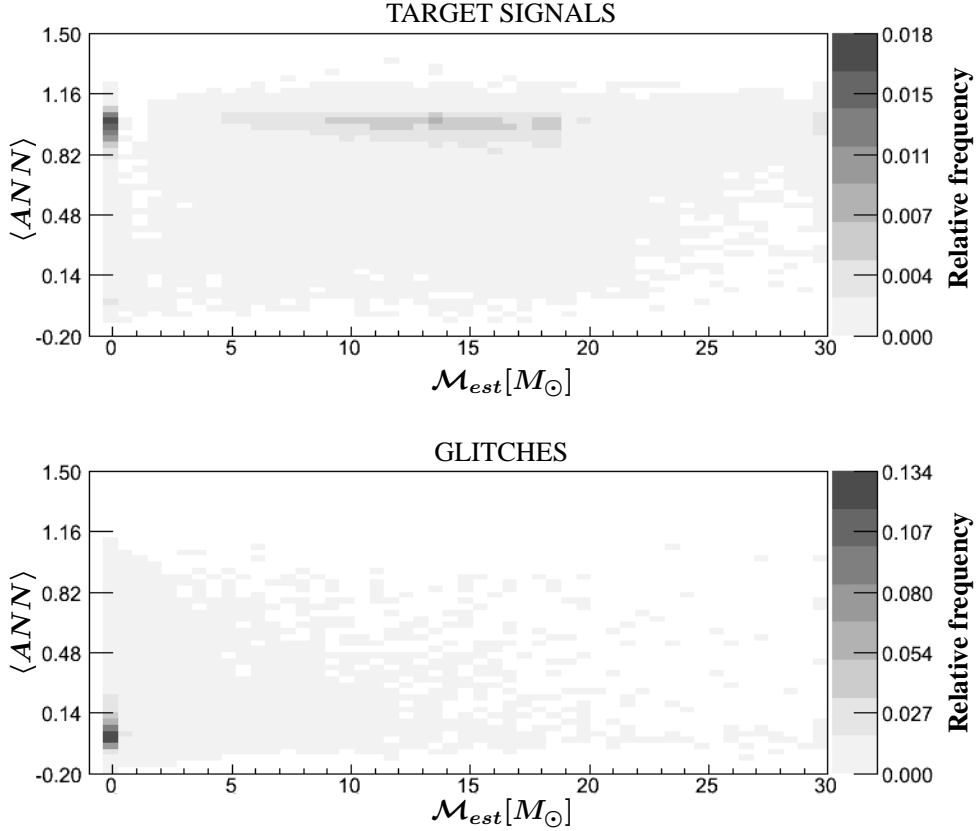
Figure 4.10: Distributions on plane defined by ANN average and the estimated chirp-mass of candidates belonging to *the wide-mass* signal class (*Top panel*) and S6D recoloured glitches (*Bottom panel*). The colour scale represents the fraction of recovered events, over a total of 5×10^4 per class. Negative values estimated chirp-mass are automatically set to zero.

down by three orders of magnitude, when switching the ranking statistic from the correlated SNR to the MVA-ANN average.

We finally performed checks to point out the sensitivity of our MVA-ANN average to the different inputs. These tests show that the estimated chirp-mass and the ANN average are by far the ones that impact more the results. Much smaller contributions comes from the central frequency, the correlated SNR and the network correlation coefficient, while duration and frequency bandwidth are the parameters which appear to be the least effective for our multivariate analysis.
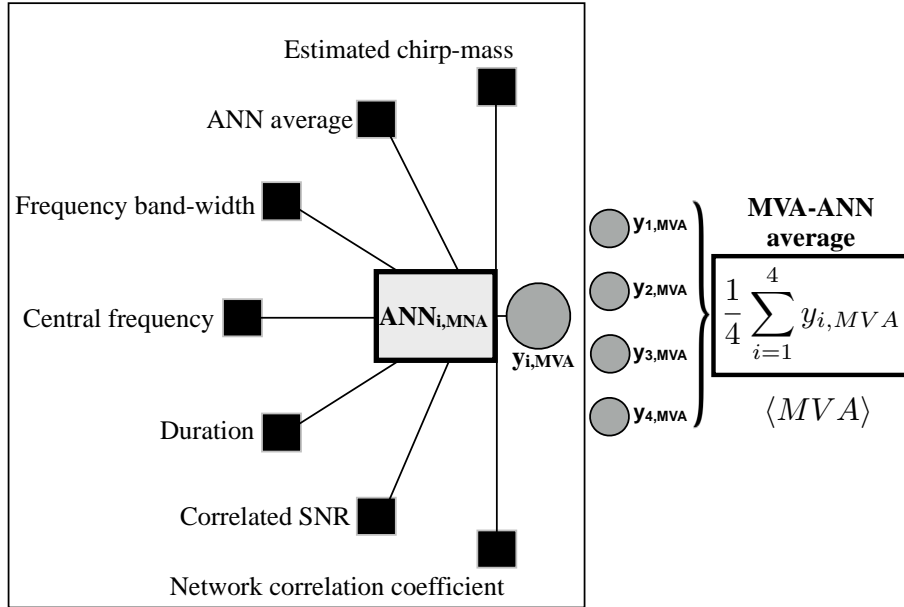
Figure 4.11: Schematic representation of the algorithm adopted to define the MVA-ANN average. In the left square, we list all the input quantities elaborated by all the four $\text{ANN}_{\text{i,MVA}}$ to obtain $\langle MVA \rangle$.
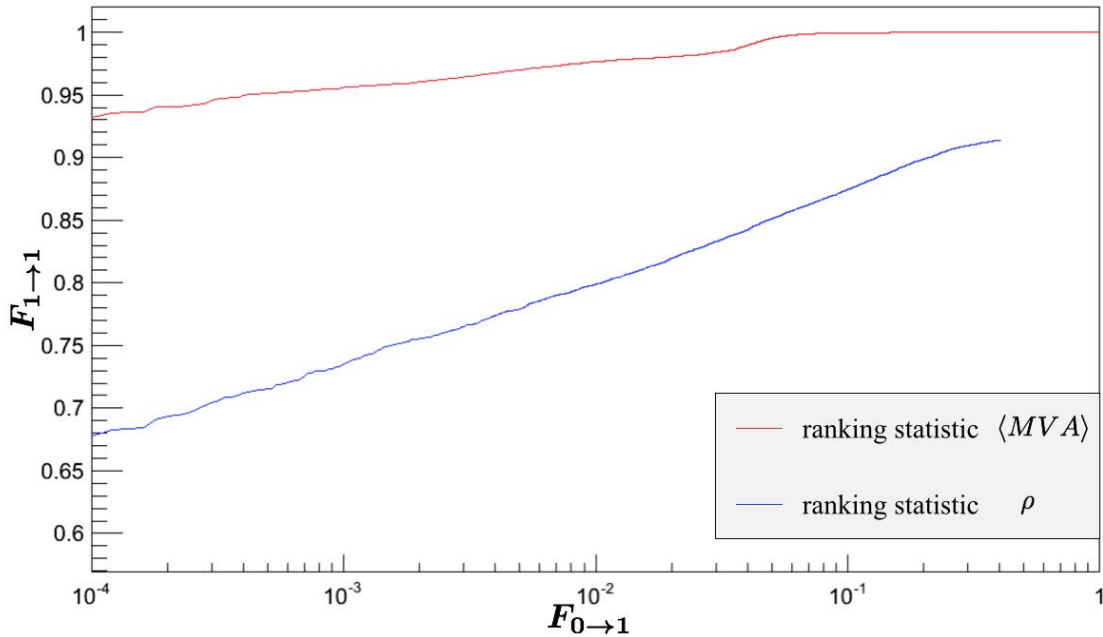
Figure 4.12: $\overline{ROC}$ using the MVA-ANN average (red) and the correlated SNR (blue) as a ranking statistic. In the last case, $F_{1\rightarrow1}$ and $F_{0\rightarrow1}$ are obtained considering a constant threshold on the network correlation coefficient $cc_{th} > 0.6$ and ignoring the ANN average. The testing set, as well as the training one, has been defined by 5×10^4 samples of S6D recoloured glitches (type0) and by 5×10^4 signals drawn from the *wide-mass* range distribution (type1).

4.4.7   Final Remarks

In the previous sections we presented the application of the signal classification to the selected case study, i.e. CBC-like transient signals with an inspiral stage chirping up in frequency. The resulting enhancement of the significance of the detected signals in this class is improved by orders of magnitude, at least in the confidence range investigated here (see fig. 4.12). Alternatively, the gain can be interpreted as a significant increase of the detected fraction of sources at a given confidence, e.g. we recover $\sim 25\%$ more signals at a mis-classification of 0.01% of noise events. The current approach could be further improved by considering more candidate parameters (cc, ρ, $\mathcal{M}_{est}$, etc), as proposed in section 4.4.6 by defining a new ranking statistic $\langle MVA \rangle$ and by generalising the classification to other signal classes.

This search can be easily integrated within the framework of an all-sky search, where the search is general and open to every kind of GW-like signals with no particular assumptions on the morphology. In this situation, we can split the overall set of interesting triggers, W, in two classes, the say *class $A \subset W$* of CBC-like signals and the complementary *class $(W - A)$* of triggers belonging to W but not to A. Following this approach for many waveform classes, all-sky searches can be managed as more separate searches on the same observation time, similarly to the more traditional case of all-sky searches performed on separate frequency bands. To account for the increased number of trials, a relative weight on these searches has to be chosen to portion out the overall false alarm probability of the all-sky search.

Signal classes of astrophysical interest can be, for example, ring-down-like signals as emitted in quasi normal modes of NSs (L. Gualtieri and Chugunov, 2014) - say *class B* signals, or, more generically, signals with a reconstructed duration longer than a number of typical cycles, allowing for a diversity of waveform amplitude envelopes and phase evolutions in time - say *class C* signals. In addition, glitch classification methods can also be implemented for vetoing purposes, i.e. to reject

the more frequent noise transient families at the detectors - say *class Z*. The most straightforward implementation of the all-sky search would then be a hierarchical signal classification scheme in subsequent steps, such as e.g. selecting $A \subset (W - Z)$, then $B \subset (W - Z - A)$, then $C \subset (W - Z - A - B)$ and finally analysing the rest $(W - Z - A - B - C)$. Such a hierarchical implementation would ensure that the considered classes are disjoint, both for signal and for glitches. Of course the more background rejection is accomplished in the first classification steps, the higher will be the resulting background left to the last ones.

In the framework of all-sky searches, the optimisation strategy is not defined, both because we are lacking reliable source population models for most source classes and because we want to be leave room for unexpected detections. The prioritisation of signal classes and the portioning of the overall false alarm probability among the classes is subjective and has to be agreed upon, as a balance between boosting detection probability of better known sources and preserving suitable detection chances for signals in the widest accessible duration-frequency range. The former requires to take into account the detectable source number within the visible volume of the search; therefore, it would prioritise e.g. the frequency band of best spectral sensitivity and/or some waveform or polarisation class. The latter instead calls for the consideration of the entire spectral range of the detectors, including disadvantaged spectral sensitivity bands, and for unmodelled waveforms and polarisation states.

This issue has to be addressed anyway, regardless of the implementation of signal classification methods. In past all-sky searches, the portioning of the false alarm probability has been driven by uniform priors, i.e. by accounting a-posteriori for the trial factor coming from multiple sub-searches on different bandwidths or, in other words, by ranking signal candidates according to a quantity closely related to their inverse false alarm rate, as measured within the related sub-search. A portioning close to uniform makes sense also for the hierarchical search depicted here.

4.4.8   Appendix

Conversion of TF representations into 8×8 frames

ANNs are here trained to recognise the common patterns in the TF representation of chirping signals. ANNs input layer are feed with the values of an 8×8 frame constructed starting from the multi-resolution TF representation of GW candidates obtained from `cWB` 2G analysis. The TF representation is defined by applying the Wilson-Daubechies-Meyer (WDM) transformation to the data (Necula et al., 2012b) at different time (ΔT) and frequency (ΔF) resolutions (related to each other by $\Delta T \times \Delta F = 1/2$). Then the algorithm selects the most energetic pixels of each map from the available resolutions (*core pixels*) to represent a particular event. From this multiple map representation, we analyse the possibility of discarding pixels, according to the rule mentioned in the first footnote of section 1. With this information we are able to focus ("zoom") on the TF region really involved by the event. This selected region is divided into fundamental units, i.e. the minimum time resolution of the selected core pixels and half of the minimum frequency resolution (according to the application of WDM transformations). We finally group all the resulted units so to obtain a 8×8 frame. In order to adjust the "zoomed" region to the 8×8 frame, each of the 8×8 squares can contain more fundamental units, or a fraction of them. The corresponding 64 values are therefore obtained by summing or spreading the likelihood of the all fundamental units used to define each frame square. These values are then normalised and used to feed the ANNs. More details can be found in (Vinciguerra, 2014a).

Analysis and parameters

Table 4.6 reports the `cWB`-parameters adopted for the transient searches described in the paper.

    The training procedure, applied to construct the ANNs used for classifying TF patterns, is defined by the parameters reported in table 4.7 (for more details on the

PARAMETER	VALUE	PARAMETER	VALUE
ρ threshold	5	cc threshold	~ 0.5
search type	i	detector network	V1H1L1
range of f	from $64Hz$ to $2048Hz$	data set	S6D
range of δt	from $\sim 3.90ms$ to $250ms$	range of δf_{max}	from $2Hz$ to $128Hz$
$\Delta t_{cluster}$	$3\ s$	$\Delta f_{cluster}$	$130Hz$

Table 4.6: Main `cWB` parameters used to analyse the recoloured data (S. Klimenko and Mitselmakher, 2008; Necula et al., 2012a).

parameters and their choice see (ROOT, 2016) and (Vinciguerra, 2014a)).

Training set	16384 BKG-events, 16384 SIG-events
Epoch number	650
Normalization	to the total of each matrix representation
	to the maximum for each matrix element on the training set
Architecture	IN: 64; H: 16/32/16; OUT: 1
Learning method	Conjugate Gradients with F.R. updating formula

Table 4.7: The training set includes the examples used for the preliminary tests. The architecture describes the input (IN), the hidden (H) and the output (OUT) layers through their numbers of neurons.

Other signal distribution

To test robustness of the proposed analysis against the uncertainty over the chirp-like signal distribution, we introduced another class of chirping signals, whose distribution is defined by the parameters reported in table 4.8.

Mass range $[M_\odot]$	$m_i \in \{10, 25, 50\}\ i \in \{1, 2\}, m_1 = m_2$
Mass distribution	uniform in the 3 m_i values
Distance range d **[Gpc]**	$\sim [10^{-4}, R_f], R_f \in \{0.7, 1.5, 2.6\}$
Distance distribution	uniform in d^3

Table 4.8: Main parameters and correspondent values adopted to construct the distribution of chirp-like events used in section 4.4.5. R_f's values are calculated taking into account the relation $SNR \propto \frac{\mathcal{M}^{5/6}}{d}$.

Chapter 5

Probing electromagnetic emission model of binary neutron-star mergers

In this chapter we briefly introduce the different types of emission expected from the merger of two Neutron-Stars (NSs) 5.1, summarising the motivation of the work presented in section 5.2.

At the time of the writing of this thesis (March 2018), the material reported in section 5.2 consists of a paper draft which we intend to submit to the Journal Astronomy & Astrophysics. The overall collaboration started thank to the interaction between myself, Ilya Mandel and Marica Branchesi. The investigation reported in the following was motivated by discussions between myself, Marica Branchesi and Giulia Stratta. The data concerning the electromagnetic model adopted for this study were provided by Riccardo Ciolfi. I designed, implemented, tested and applied the algorithm saprEMo. I presented and analysed the methodology with Marica Branchesi, Riccardo Ciolfi and Ilya Mandel. I discussed the main results mostly with Coenraad J. Neijssel, Marica Branchesi, Riccardo Ciolfi and Ilya Mandel. I produced all the plots presented in the paper, considering feedbacks from all the authors, particularly

Coenraad J. Neijssel and Ilya Mandel. The text was written by myself in collaboration with Riccardo Ciolfi. All the authors suggested modifications and gave feedback on the paper draft.

5.1 Electromagnetic and gravitational emission from binary neutron-star mergers

Mergers of Binary NS (BNS) have been for a long time the main target source of ground based GW-detectors. Before the discoveries in the first observing runs of the advanced interferometers, BNSs were the only observed GW source characterised by a fairly certain signal strength. The gravitational signal emitted by such systems is predicted by the theory of GR, and, in the low frequency regime, was indirectly confirmed by the orbital decay of PSR B1913+16, the Hulse and Taylor binary. The emission was expected to reach amplitudes and frequencies detectable by the second generation of interferometers, and indeed was observed by advanced LIGO and Virgo on the 17th of August 2017. Compared to the emission generated by the coalescences of two Black-Holes (BH), GW signals characterising the merger of BNSs contain much more information related to behaviour of matter in extreme physical conditions. The late inspiral of these GW signals is expected to carry signatures of tides, whose strength is mostly determined by the unknown equation of state of NSs. Given the component masses of the system, such relation determines many fundamental properties of the BNS coalescence, including the amount of ejected material and the nature of the merger remnant. These properties in turn strongly affect the expected electromagnetic emission. Depending on the NS's electromagnetic fields, the emission can arise as a precursor, even before the end of the inspiral. However, most of the emission is expected to be generated during the dynamical phase, which begins once tidal effects can no longer be neglected and lasts until a stable configuration is reached. During this stage of the binary evolution, the strong gravitational interaction and the NS microphysics become complicated to model. For

this reason qualitative and quantitative investigations dedicated to BNS emission require numerical simulations which often describe only one of these two aspects in details, approximating the other. To predict accurate GW waveforms, efforts have been devoted to solving the Einstein field equations in full GR regime, simplifying the treatment of matter. On the contrary, for investigating electromagnetic emission associated to BNS mergers, such as short gamma ray bursts (SGRBs), gravitational interactions are often simplified in favour of a more realistic description of matter. Due to their relatively high detection rate and luminosity, SGRBs have for long been considered among the most promising electromagnetic counterparts of GWs emitted by CBCs. However, before August 2018, the origin of such phenomena was only marginally constrained by observations, without any definitive prove of their association to compact binary mergers. SGRBs have themselves being investigated for decades, with satellites such as CGO, Swift and Fermi. Observational evidences, such as the lack of supernovae association and diversity of host galaxy type, have long suggested that these energetic transients originate from a different phenomenon than the long-soft GRBs, generated during the collapse of massive stars. Mergers of compact objects were the first proposed origin of GRBs and were recently identified as sources of (at least some) SGRBs. Many years of observations pointed out unexpected features related to these transients, such as X-ray plateaus. Present in almost $\sim 50\%$ of SGRBs, this long X-ray emission might hint to the generation of a long lived NS after the coalescence. This scenario, supported by the discoveries of stable NSs of $\sim 2M_\odot$, and the growing interests of the scientific community in sources related to GWs, have inspired theoretical investigations, resulting in various proposed EM models (e.g. (Siegel and Ciolfi, 2016a),(Sun et al., 2017),(Kisaka et al., 2016)).

Nowadays many SGRBs, and therefore possibly to BNS mergers, are associated to afterglows emissions. In the standard fireball model for GRBs, afterglows are generated by the external shocks of a relativistic jet with the circumburst environment (Berger, 2014). The consequently released synchrotron emission spans a wide range

of frequencies, from X-ray to radio, and allows for distance measurements. Sky localisation and distance play a fundamental role in the interpretation of the nature of GRBs, allowing host identification and determining the cosmological origin of their sources. Another key emission, associated to SGRBs and predicted as consequence of BNS mergers, is kilonovae (Metzger, 2017). Kilonovae are generated by the radioactive decay of the r-process elements which are expected to be produced in such neutron rich environment. Before the operation of the advanced GW-detectors, the only GRB linked to an optical excess consistent with kilonovae models was GRB 130603B, although other more controversial kilonova detections were later claimed to be associated with different events.

On the 17th of August 2017, the era of multi-messenger astronomy began, with the coincident detection of GWs (GW170817 (Abbott et al., 2017f)) and their electromagnetic counterparts ((Abbott et al., 2017h)). GW170817 is the first observation of GWs consistent with the merger of a BNS. However, GW analysis alone cannot exclude the presence of compact objects different from NSs. The detection of coincident electromagnetic events therefore played a key role for the interpretation of the nature of GW170817's source, pointing to the merger of two NSs. With a combined SNR of 32.4, GW170817 is the clearest gravitational event ever detected by advanced LIGO. The detailed analysis of such a gravitational signal revealed as a source a binary with component masses included in the range $1.17 - 1.60 \ M_\odot$ with a mass ratio $q \in [0.7, 1]$(limiting NS spins according to observations of pulsars in BNSs merging within Hubble time). The system was localised at a luminosity distance of ~ 40 Mpc, in a sky area of $\sim 30 \ \mathrm{deg}^2$, thanks to the 3-detector network (Virgo and the 2 LIGO observatories) operative at the time of the detection. This localisation has allowed many EM facilities to follow up the GW event, already associated to the almost simultaneous (with a delay between EM and gravitational emission of only ~ 1.7 s) detection of the SGRB GRB 170817A. The observational campaign includes instruments covering a wide range of the EM spectra and has already con-

firm some of the predictions mentioned above, such as the association of BNS to
SGRBs, the formation of r-process elements with the consequent kilonova emission
and radio and X-ray afterglows. Most of these EM observations showed peculiar
characteristics (such as the energy of GRB 170817A), which need to be further in-
vestigated. Although the observation of EM counterparts of GW170817 proves the
presence of matter, it does not definitively constrain the nature of the remnant,
leaving some of the proposed models (such as the X-ray emission model adopted in
the following paragraph (Siegel and Ciolfi, 2016a)) to be open for debate. It is in
this context that we propose the *s*implified *a*lgorithm for *pr*edicting EM *o*bservations
(`saprEMo`) presented in the following section. The aim of the tool is to calculate the
expected number of EM emission, characterised by a specific light-curve, present in
a specific survey of electromagnetic data. `sapEMo` can bridge observations to the-
oretical predictions, by allowing (given a BNS merger rate) comparisons between
EM models and real astronomical data. `sapEMo` is designed and implemented with
a flexible structure, allowing its application in different spectral bands as well as to
astrophysical phenomena not related to BNS mergers.

5.2 saprEMo: a simplified algorithm for predict-
ing electromagnetic observations

The multi-wavelength detection of GW170817 has opened multi-messenger astron-
omy. The next challenge consists in interpreting the growing information on mergers
of compact objects in a coherent framework, based on both the electromagnetic and
gravitational-wave inferences.

Analyses of future joint observations can be optimised by constraining the expecta-
tions on electromagnetic (EM) emission associated with transient gravitational-wave
sources and by running targeted searches. This work describes `saprEMo`, a tool aimed
at predicting the number of electromagnetic signals, characterised by specific light-
curve and spectrum, expected in a particular sky survey. By looking at archival data,

`saprEMo` allows us to constrain models of electromagnetic emission or phenomeno-
logical rates. Applying `saprEMo` to proposed astronomical missions/observational
campaigns provides a perspective and outline the scientific impact of adopting dif-
ferent observational strategies. We estimate the number of binary neutron-star coa-
lescences potentially observable in a specific survey, by integrating over cosmic dis-
tances the binary neutron-star merger rate and by convolving the results with the
survey properties. For our first case study, we adopt the spindown-powered X-ray
emission predicted by (Siegel and Ciolfi, 2016a,b) in the case of a binary neutron-
star merger producing a long-lived (or even stable) neutron-star. We evaluate the
fraction of signals that are expected to be detected within the observational win-
dow, distinguishing between transients displaying or not their maximum luminosity
(named *peaks* and *tails*, respectively). We estimate flux and redshift distributions of
these signals for data collected by XMM-Newton and Chandra and by one year of
possible future observations with the mission concept THESEUS. We demonstrate
that our emission and binary neutron-star merger rate models imply the presence of
a few signals in the XMM-Newton catalogs. Comparing these predictions with ac-
tual data and dedicated studies (such as the transient search carried by the ExTRaS
group; (De Luca, 2014)) allows us to validate the implicit assumptions of our inputs.
We also show that the new class of X-ray transients claimed in (Bauer et al., 2017)
is marginally consistent with the expectation rate deduced by assuming the chosen
emission model and with reference to the Chandra Deep Field-South properties. Fi-
nally, by studying the mission concept THESEUS, we prove the substantial impact
of the field of view in searches of X-ray transients associated with binary neutron-star
mergers. According to our study, THESEUS would have the capability of revealing
a population of signals which will considerably constrain the binary neutron-star
merger rate and its dependence on redshift. In this paper, we have outlined an al-
gorithm dedicated to estimating the chance of detecting particular electromagnetic
transients in specific surveys. The flexibility of the code enables investigations on
a large variety of electromagnetic emission models and future mission capabilities.

The general structure of `saprEMo` supports a wide range of applications, involving different phenomena across the whole electromagnetic spectrum.

5.2.1 Introduction

GW170817 ((Abbott et al., 2017g)) has just opened the era of multi-messenger astronomy ((Abbott et al., 2017h)). The first coincident gravitational and electromagnetic observation has already provided an extraordinary insight to the involved mechanisms. Among the key results of such revolutionary discovery, is the confirmation of the association between the merger of two Neutron-Stars (NSs) and (at least some type of) short Gamma-Ray Bursts (SGRBs) ((Abbott et al., 2017h) and references therein). However, many open questions remain on the nature of SGRBs. The intense gamma-ray observation campaign and multi-wavelength follow-ups of the last decades have indeed kept revealing new and unexpected features, such as early and late X-ray flares, extended emission, and X-ray plateaus (e.g., (Berger, 2014) and references therein). Intensified theoretical efforts have been dedicated to explain these observations and coherently explore these and other possible electromagnetic signals generated by these sources.

In order to validate the variety of proposed theoretical scenarios in the context of multi-messenger astronomy with compact binary mergers, we present `saprEMo`, a *Simplified Algorithm for PRedicting ElectroMagnetic Observations*. Given some overall characteristics of an astronomical survey of data, this tool allows to predict how many electromagnetic (EM) signals characterised by a specific light-curve and spectrum should be present in the catalog/data set, for a given cosmological rate of compact binary mergers. Predictions can be used both to validate the theoretical scenarios against data already collected and to critically examine the scientific means of future missions and their observational strategies.[1]

We describe the main features of `saprEMo` in section 5.2.2. As first case study, we use `saprEMo` to investigate the X-ray emission proposed by (Siegel and Ciolfi,

---

[1]While we refer here to the case of compact binary mergers as the prime multi-messenger sources, similar considerations can be extended to other type of transients (e.g. core-collapse supernovae).

2016a,b) (see section 5.2.3) and generated by Binary NS (BNS) mergers leading to the formation of a long-lived and strongly magnetised NS. We apply `saprEMo` to present surveys, collected by XMM-Newton and Chandra, and study the potential of the mission concept THESEUS. Results are reported in section 5.2.3 and discussed in section 5.2.4. Finally, in section 5.2.5 we draw our conclusions summarising our first results and outlining some scientific cases that can be investigated with `saprEMo` in the future.

5.2.2   saprEMo outline

`saprEMo` is a Python algorithm designed to predict how many detectable electromagnetic signals E are present in a survey S.

In view of future EM instruments, answering this question not only allows to outline the main scientific prospectives of the mission, but also tests the impact of different observational strategies. Furthermore, the same investigation can be applied to past and present surveys, in order to prove and constrain theoretical EM (or rate) models by comparing these expectation studies directly with acquired data. With the rate integration over cosmological distances, `saprEMo` estimates the number of signals whose emission flux F at the observer is above the flux limit F_{lim} of the S survey (i.e. $\exists\, t' \,|\, F(t') > F_{lim}$ where t' is the time at source).

Core analysis

`saprEMo` can be applied to any type of EM emission, from transients to continuous sources (with caveats on the definition of number of observations[1]), emitting in any EM spectral range. In this work, we focus on transients associated with mergers of BNS. The expected number of BNS mergers N_{BNS_m} in the volume enclosed within redshift z_{max}, in a time T at the observer, is:

$$N_{BNS_m} = T \int_0^{z_{max}} \frac{R_V(z)}{1+z} \frac{dV_C}{dz}\, dz \qquad (5.1)$$

where $R_V(z)$ is the rate of BNS mergers per unit of comoving volume at source V_C. In our case z_{max} is the maximum distance at which the emission model of interest E, can be seen. z_{max} is calculated considering both the spectral shift due to the source redshift compared to the instrument energy band $E^I \sim \left[E^I_{min}, E^I_{max} \right]$ and the maximum luminosity distance, set by the peak luminosity $L_p(E)$ of the E model and the sensitivity F_{lim} of the survey. We only expect a fraction of N_{BNS_m} to be observed by a specific instrument, depending on the emission properties and the characteristics of the survey. The number of BNS mergers, detectable by the S survey during the peak of the considered emission E, is given by:

$$N_p = \varepsilon \, \frac{FoV}{4\pi} \, \langle T_{obs} \rangle \, n_{obs} \int_0^{z_{max}} \frac{R_V(z)}{1+z} \frac{dVc}{dz} \, dz \qquad (5.2)$$

where T of eq. (5.1) is here the total time given by the product of the average exposure time $\langle T_{obs} \rangle$ and the number of the observations n_{obs} collected in the S survey. $\langle T_{obs} \rangle$ is defined as the mean time of a continuous observation of the same sky-position. In eq. (5.2), the field of view FoV of the instrument reduces the number N_{BNS_m} of signals present in the survey by $FoV[sr]/4\pi$. In the specific case of BNS mergers, the efficiency factor ε typically includes the occurrence rate of a specific merger remnant (ε_{sr}), which are expected to generate the emission E, and source geometry/observational restrictions such as collimation ($\varepsilon_c = 1 - \cos(\theta)$, where θ is the beaming angle), so that $\varepsilon \sim \varepsilon_{sr} \cdot \varepsilon_c$. We define the signals included in N_p **PEAKS**. This contribution only depends on the light-curve of the emission by the predicted luminosity peak and spectra, while it is completely independent from its monochromatic evolution in time. The intrinsic duration of the emission model E, adds an additional contribution to the detectable signals. We call signals belonging to this contribution **TAILS**. These are the mergers whose emission is detected only before (first block of eq. (5.3)) or after (second block of eq. (5.3)) the peak of luminosity (i.e. L_p is outside the observation period); the longer the light-curve is above F_{lim}, the higher the probability of it being observed. To estimate this contribution, we need to account for the evolution in time of the emission luminosity

$L(t')$, which will affect the horizon of the survey:

$$N_t = \varepsilon \, \tilde{n}_{obs} \frac{FOV}{4\pi} \left[\int_{-\infty}^{t'_p} \int_0^{z_t(L(t'))} \frac{R_V(z)}{1+z} \frac{dV}{dz} c \, dz \, dt + \right.$$
$$\left. \int_{t'_p}^{+\infty} \int_0^{z_t(L(t'))} \frac{R_V(z)}{1+z} \frac{dV}{dz} c \, dz \, dt \right] \qquad (5.3)$$
$$= \varepsilon \, \tilde{n}_{obs} \frac{FOV}{4\pi} \int_{-\infty}^{+\infty} \int_0^{z_t(L(t'))} \frac{R_V(z)}{1+z} \frac{dV}{dz} c \, dz \, dt$$

where t and $t' = t/(1+z)$ are the time respectively at observer and source frames and t'_p is the time correspondent to the peak luminosity. $z_t (L(t'))$ represents the horizon of the survey, given the specific intrinsic luminosity of the source $L(t')$. In eq. (5.3) $\tilde{n}_{obs}$ is the "effective" number of observations, which can differ from n_{obs} if the survey contains repeated observations of the same sky coordinates [2]. In practice the time integration of eq. (5.3) is limited by the available light-curve of the emission above the flux limit. The time integral in eq. 5.3 spans the duration of the light curve (not of the typical observation, as in eq. 5.2 [3]). The relative importance of peaks and tails depends on the ratio between the duration of the observable emission and the typical exposure time (see figure 5.1 and the simplified example reported in figure 5.2).

While eq. (5.2) and (5.3) explain the general concept behind the tool, they do not explicitly account for the energy (or wavelength $E = \hbar c/\lambda$) dependence of light-curves, instrument sensitivities and absorption. These effects are particularly important in presence of emissions and instruments which allow to explore the Universe at high redshift. The redshift of the radiation changes the horizon of the detectable light-curve, not only by reducing the flux at observer but also because different components of the emission enter the spectral sensitivity of the instrument.

---

[2]Since `saprEMo` counts the number of signals, multiple observations of the same sources should not contribute to the output numbers. Sky locations that are repeatedly observed should therefore be considered carefully to estimate the tail contributions; indeed for N_t, to include only distinct signals, the time interval between the different exposure times must be sufficiently large to include the whole emission.

[3]For this reason, we are not double counting the peak contribution despite the inclusion in the integral of the emission time (which can indeed be considered infinitesimal) correspondent to the peak of luminosity
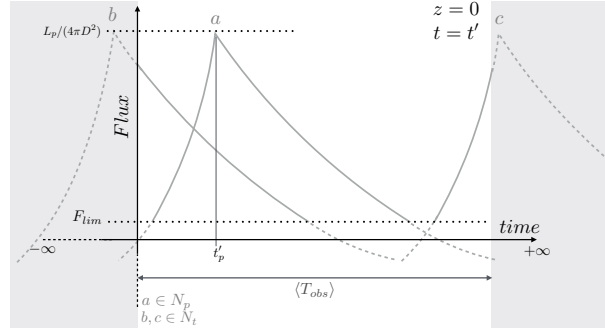
Figure 5.1: Schematic representation of a peak ($t_p \in \langle T_{obs} \rangle$) signal ($a$) and tails ($b$, c). The solid curves represented the part of signals E visible during the exposure time at the observer, the dashed components are the missed (because of time or flux restrictions) part of the emissions. The upper dotted line shows the peak flux $F_p = L_p/(4\pi D^2)$, the lower line the flux limit of the survey.
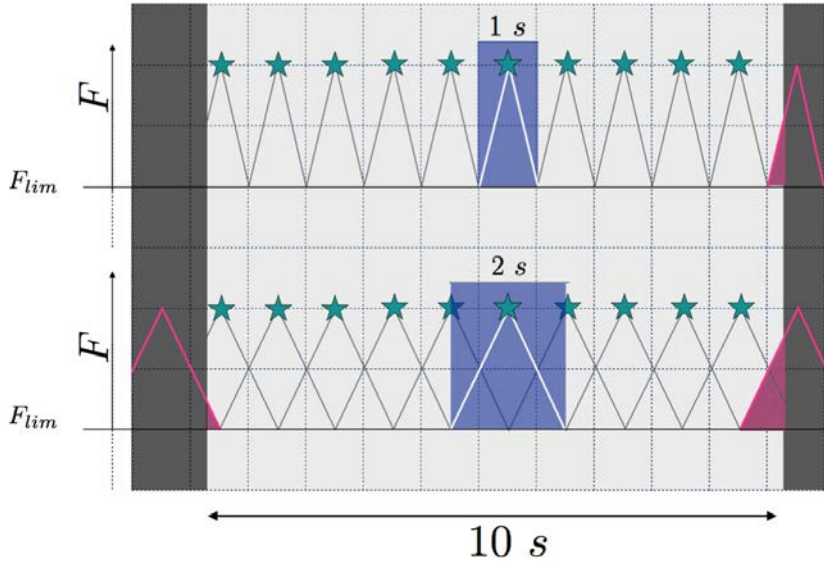
Figure 5.2: **Example of peaks and tails:** we report the ideal case of perfectly periodic events, say BNS mergers, with unrealistic rate $1/1s$. We focus on emission generated in the local Universe, assuming $z_{max} \sim 0$. We consider the simplified case of triangular light curve with durations 1 s (upper panel) and 2 s (bottom panel). $x-$ and $y-$ axes represent respectively the 10 s of observation time and the emission flux F, above the survey sensitivity F_{lim}, in arbitrary units. The graph shows the peak contribution, i.e. the events whose maximum luminosity falls in the observational window (event marked with a green stars) and the tail contribution, i.e. the events detected only before or after the peak of luminosity, emphasised with fuchsia lines. In both upper and bottom cases, we detect 10 peaks, as expected given the fixed 10 s of observation and the rate of 1 merger per second. Differently the number of tails changes from 1 to 2 by doubling the duration of the detectable emission. The graph shows as, given a fixed rate, the number of peaks only depends on the observing time, while the number of tails only depends on the duration of the events.

Moreover in the frequency range of operation of an instrument, its sensitivity is often energy dependent. For this reason, `saprEMo` considers different flux limits $[F_{lim}]_g$ for each of the spectral band g of the survey. Here we denote each energy band $[E^I_{min}, E^I_{max}]_g$ with the label g; we use $[E^I_{min}, E^I_{max}]$ without subscripts, for the whole range of operation.

Redshift / K-correction To evaluate if the emission is visible in a g band of the instrument, we need to calculate the fraction of source light-curve which contributes to the flux in the g band at the observer. We assume a set of light-curves $[L_h(t')]_{h=0}^{h_{max}}$, where each element $L_h(t')$ represents the emission in the source frame within a fixed h energy bin $[E'_{min}, E'_{max}]_h$. The redshifted h energy bin, associated to the light-curve element $L_h(t')$, might only partially overlap with an instrumental energy bin g. To consider only the part of the light-curve which contributes to the emission visible in the energy bin g, we calculate the fraction of the h energy bin that falls into the band g and assume the energy is uniform across its intrinsic curve. Therefore for each numerical step in z, we calculate the emission contribution to each g band:

$$L_g(t', z) = \sum_{h=0}^{h_{max}} L_h(t') w_{hg}(z) \tag{5.4}$$

When the redshifted h bin and the g band of the instrument overlap, the $L_h(t')$ light-curve contribute to the total observable emission in the g band $L_g(t', z)$ with a weight defined by the ratio between the the amount of overlap and the width of the light-curve energy bin:

$$w_{hg}(z) = \begin{cases} \alpha \; \text{if} \; \alpha > 0 \\ 0 \; \text{otherwise} \end{cases} \tag{5.5}$$

where

$$\alpha = \frac{min\left((1+z)^{-1}E'_{max,h}, E^I_{max,g}\right) - max\left((1+z)^{-1}E'_{min,h}, E^I_{min,g}\right)}{(1+z)^{-1}[E'_{max,h} - E'_{min,h}]} \tag{5.6}$$

This approach assumes the light-curve within h bin, $L_h(t')$, can be approximate as uniformly distributed in energy. This assumption of uniform distribution is applied for any number of input energy bands, including the case of a single light-curve available for the whole energy range of interest. This procedure is in general more precise finer are the energy subdivisions at which a light-curve is associated.

Absorption `saprEMo` can account for both host and galactic absorptions. The host-galaxy absorption is included by substituting $L_h(t')$ with $\tilde{L}_h(t') = L_h(t') \exp^{-n_{\mathrm{H,h}}\sigma_h}$, where $n_{\mathrm{H,h}}$ is a typical value of the effective hydrogen column density and σ_h is the average of the absorption cross-section in the h energy band in the source frame. Both of these quantities may depend on the type of the host galaxy. Similarly, the Milky-Way absorption is accounted adopting $\tilde{L}_g(t', z) = L_g(t', z) \exp^{-n_{\mathrm{H,MW}}\sigma_g}$. We estimate an effective hydrogen column density as a function of the observed sky-locations, adopting the sky-map of HI emission-line brightness T_b released by (Kalberla et al., 2005). For each position in the sky, the galactic column density $\eta_{H,MW}$ is calculated adopting equation (4) of (Chengalur et al., 2013) (valid for negligible total opacity). These values then have to be averaged along galactic longitudes l, $\langle \eta_{H,MW} \rangle_l$, and finally associated to the relative frequency of observations in the survey to calculate an effective column density $n_{H,MW}$:

$$n_{H,MW} = \frac{1}{n_{obs}} \sum_{j=1}^{n_{obs}} \langle \eta_{H,MW} \rangle_{l_j} (b_j, l_j) \tag{5.7}$$

where b is the galactic latitude. To establish the detectability of the light-curves $\tilde{L}_g(t', z)$, we calculate the corresponding fluxes:

$$F_g(t', z) = \frac{\tilde{L}_g(t', z)}{4\pi D_L^2(z)} \tag{5.8}$$

Detailed implementation To include absorption, energy dependence of the sur-

vey sensitivity and redshift of the E emission along the cosmic integration, we estimate the peak contribution with:

$$N_p = \varepsilon \ n_{obs} \frac{FOV}{4\pi} \ \langle T_{obs} \rangle \int_0^\infty \frac{R_V(z)}{1+z} \frac{dVc}{dz} Test(z) \, dz \tag{5.9}$$

where

$$Test(z) = \begin{cases} 1 \text{ if exists } g \mid z_{max,g} > z \\[2ex] 0 \text{ otherwise} \end{cases} \tag{5.10}$$

and $z_{max,g}$ is the maximum redshift observable in the g energy band. Similarly, we compute the number of tails with:

$$N_t = \varepsilon \ \tilde{n}_{obs} \frac{FOV}{4\pi} \int_0^{\overline{z_{max}}} R_V(z) \frac{dVc}{dz} D_{sig}^{obs} \, dz \tag{5.11}$$

where $\overline{z_{max}}$ is the maximum redshift which contributes to equation (5.9) and $D_{sig}^{obs} = \bigcup_g [dt'_{vis}]_g$ represents the union of source time-intervals of the light-curve $dt'_{vis,i}$ which are visible at z in at least one g band, i.e.

$$\forall g \quad dt'_{vis,i} = t'_{i+1} - t'_i \mid [F_g(t'_i, z) + F_g(t'_{i+1}, z)] > 2 \ F_{lim,g} \tag{5.12}$$

Inputs and Outputs

We now present inputs and outputs of `saprEMo`.

Inputs:

1. **Light-curves** of the EM emission E in different energy bins (including energies higher than the instrument band, if predicted from the model, to account for redshift effects);

2. **astrophysical rate** at source frame $R_V(z)$;

3. **efficiency** ε of the EM model E (ε should account for source geometry/selection effects, such as collimation, as well as for occurrence of the physical requirements, necessary for the emission generation);

4. **main instrument and survey properties**:

   (a) energy bands of the survey $S\,[E_i, E_s]_g$;

   (b) correspondent flux limits $[F_{lim}]_g$;

   (c) average observation time $\langle T_{obs} \rangle$;

   (d) field of view FoV [1];

   (e) number of observations n_{obs}[1].

Outputs:

- $\boldsymbol{N_p}$ and $\boldsymbol{N_t}$: number of peaks and tails which are expected in the survey S. The number of signals returned by `saprEMo` should be interpreted as expectation values of a Poisson process. Therefore also statistical errors should be considered in addition to the systematics due to rate and emission model uncertainties;

- $\boldsymbol{N_p(F)}$ and $\boldsymbol{N_t(F)}$: distributions of these numbers as a function of fluxes;

- $\boldsymbol{N_p(z)}$ and $\boldsymbol{N_t(z)}$: distributions of these numbers as a function of redshift;

- $\boldsymbol{N_p(D_{sig}^{obs})}$ and $\boldsymbol{N_t(D_{sig}^{obs})}$: expected distribution of durations.

Distributions in redshift are useful to estimate the horizon of the survey to the emission E and for astrophysical interpretations. It allows to predict the cosmological origin of the detectable sources. This can be useful to statistically infer the redshift distribution when a counterpart allowing z measurement is missing, or to constrain cosmic rate models of BNS mergers when the multi-wavelength allows the identification of the source location. Distributions of

---

[1] Or equivalently covered sky-area $f_{sky} \sim n_{obs} \frac{FOV}{4\pi}$.

fluxes and durations are robust observables, which enable comparisons with real data.

At each step in redshift, necessary to compute the integrals (5.9) and (5.11), `saprEMo` not only calculates the contribution to N_t and N_p, but also the associated flux, to gradually build the output distributions. The total flux is obtained by summing the light-curves in luminosity in the different energy bands and rescaling with the associated luminosity distance. A direct comparison with the event flux distributions often reported in survey catalogs require to take into account data analysis procedure which estimates source flux from count rates assuming a model [4]. To estimate the distribution of the signal durations, we save, at each z-step in both peak (5.9) and tail (5.11) integrations, the set of light-curve times correspondent to fluxes higher than the limits, i.e. $[dt'_{vis}](z) = \bigcup_g [dt'_{vis}]_g$ as defined in (5.12). We then analytically approximate the exposure time distribution P_{obs} from the available informations (which might be the actual set of duration or its average and standard distribution) with a *Maxwell–Boltzmann* or *Log-normal* function, according to the user input. We simulate $N_{trials} = 200$ signal durations for each data saved from the cosmic integrations. For the peak contribution and for each trial, we randomly draw the starting time t'_s of the observation from the uniformly distributed time-interval $\left[min\left([t'_{vis}](z)\right), t'_p \right]$, where t'_p is the source time correspondent to the peak of the emission. We then randomly draw N_{trials} exposure times $D_{exp}(z)$ from the defined distribution P_{obs}. The end time of each $i-$ trial $t'_e[i]$ is defined as $t'_e[i] = min\left([max(t'_{vis}(z)), t'_s[i] + D_{exp}[i]/(1 + z)]\right)$. The final duration at observer is then defined as $D[i](z) = (t'_e - t'_s)(1 + z)$. A similar approach is applied for obtaining duration distributions of tails, with the dif-

---

[4]A direct comparison of the emission model to a population of sources should include the following steps: (i) flux estimation at observer, taking into account model luminosity and source distance (as estimated within `saprEMo`), (ii) estimation of photon count rate from model fluxes accounting for energy dependence and instrument response, including sensitivities in different bands, efficiency, statistics on source location in CCDs etc... (iii) calculation of expected fluxes from count rates according to the procedure adopted by the specific S survey (which usually also includes the assumption of a power law source spectrum).

ference of requiring, in the considered interval, the peak luminosity absence, instead of its presence.

In `saprEMo` detections are defined on a flux-based criteria: $\exists\ g,\ t'\ |\ F_g(t') > F_{lim,g}$, i.e. a signal is flagged as observed if at least in one energy band the flux is over the limit of the survey. We plan to upgrade the tool in the near future by including the possibility of choosing different detection criteria, accounting for background and simplified relations between quantities such as integration times and limiting fluxes.

5.2.3   Application to soft X-ray emission from long-lived binary neutron-star merger remnants

In the following, we consider a specific application of `saprEMo` referred to the case of spindown-powered X-ray transients from long-lived NS remnants of BNS mergers.

Depending on the involved masses and the NS equation of state (EOS), a BNS merger can either produce a short-lived remnant, collapsing to a Black-Hole (BH) within a fraction of a second, or a long-lived massive NS. The latter can survive for much longer spindown timescales (minutes to hours or more) prior to collapse or even be stable forever. The recent discovery of single NSs with a mass of ~ 2 M$_\odot$ (Demorest et al., 2010), (Antoniadis et al., 2013) favour stiff EOS and suggests that a relevant fraction of BNS merger remnants will be long-lived. According to recent estimates, this fraction should range from a few percent up to more than half of all BNS mergers (e.g., (Piro et al., 2017)).

An additional supporting element in favour of long-lived remnants is given by the observation of long-lasting ($\sim$ minutes to hours) X-ray transients following a significant fraction of SGRBs (e.g., (Rowlinson et al., 2013),(Gompertz et al., 2014), (Lü et al., 2015)). Given the short accretion timescale of a remnant disk onto the central BH ($\lesssim 1$ s), such long-lasting emission represents a

challenge for the canonical BH-disk scenario of SGRBs while it can be easily explained by alternative scenarios involving a long-lived NS central engine, e.g., the magnetar (Zhang and Mészáros, 2001), (Metzger et al., 2008) and the time-reversal (Ciolfi and Siegel, 2015) scenarios. According to this view, the fraction of SGRBs accompanied by long-lasting X-ray transients might reflect the fraction of BNS mergers producing a long-lived NS.

If the merger remnant is a long-lived NS, its spindown-powered electromagnetc emission represents an additional energy reservoir that can potentially result in a detectable transient. Recent studies taking into account the reprocessing of this radiation across the baryon-polluted environment surrounding the merger site have shown that the resulting signal should peak at wavelengths between optical and soft X-rays, with luminosities in the range $10^{43} - 10^{48}$ erg/s and time scales of minutes to days (e.g., (Yu et al., 2013), (Metzger and Piro, 2014), (Siegel and Ciolfi, 2016a,b)). Besides representing a rather natural explanation for the long-lasting X-ray transients accompanying many SGRBs, this spindown-powered emission has been recently identified as a promising electromagnetic counterpart to BNS mergers (e.g., (Stratta et al., 2017) and references therein), having the advantage of being both very luminous and nearly isotropic.

For our first direct application of saprEMo, we consider the spindown-powered transient model by (Siegel and Ciolfi, 2016a,b) (hereafter SC16), described in the next section 5.2.3, in which the emission is expected to peak in the soft X-ray band. The high luminosity and isotropy of the model make indeed SC16 particularly interesting for highlighting the potential impact of our analysis. In section 5.2.3 we then present our results referring to three different X-ray satellites: XMM-Newton, Chandra, and the proposed THESEUS. A general discussion on the results is presented in section 5.2.4.

Reference emission model

The model recently proposed by Siegel & Ciolfi (SC16) describes the evolution
of the environment surrounding a long-lived NS formed as the result of a BNS
merger. The spindown radiation from the NS injects energy into the system
and interacts with the optically thick baryon-loaded wind ejected isotropically
in the early post-merger phase, rapidly forming a baryon-free high-pressure
cavity or "nebula" (with properties analogous to a pulsar wind nebula) sur-
rounded by a spherical shell of "ejecta" heated and accelerated by the incom-
ing radiation. As long as the ejecta remain optically thick, the non-thermal
radiation from the nebula is reprocessed and thermalised before eventually es-
caping. As soon as the ejecta become optically thin, a signal rebrightening
is expected, accompanied by a transition from dominantly thermal to non-
thermal spectrum. The model can also take into account the collapse of the
NS to a BH at any time during the spindown evolution phase.[5]

Exploring a wide range of physical parameters, SC16 found that the escaping
spindown-powered signal has a delayed onset of $\sim 10 - 100$ s and in most cases
peaks $\sim 100 - 10^4$ s after merger. Furthermore, the emission typically falls
inside the soft X-ray band (peaking at $\sim 0.1 - 1$ keV) and the peak luminosity
is in the range $10^{46} - 10^{48}$ erg s^{-1}.

In this work, we consider only one representative case, corresponding to the
"fiducial case" of SC16. Light-curve and spectral distribution of this particular
model are shown in fig. 5.3. The main parameters of the model are as follows.
The early baryon-loaded wind ejects mass isotropically at an initial rate of
5×10^{-3} $M_\odot$ s^{-1}, decreasing in time with timescale of 0.5 s. The dipolar
magnetic field strength at the poles of the NS is 10^{15} G and the initial rotational
energy of the NS is 5×10^{52} erg ($\sim$ ms initial spin period). Moreover, in this case
the remnant evolves without collapsing to a BH. In fig. 5.3 we can distinguish

---

[5] We refer to SC16 and (Ciolfi, 2016) for a detailed discussion of the model and its current
limitations.
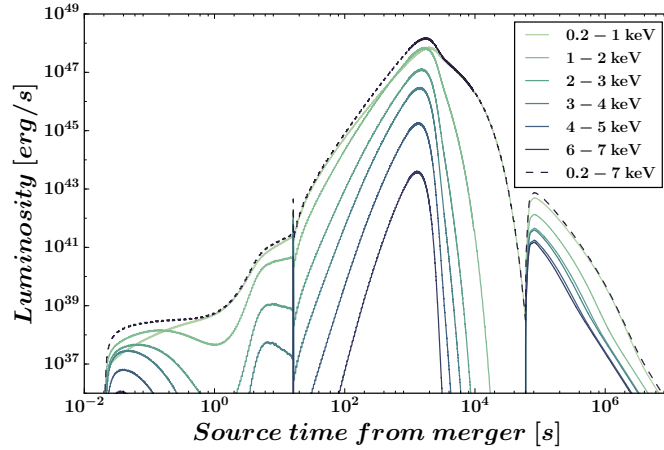
Figure 5.3: Light-curve of the spindown-powered emission from a long-lived BNS merger remnant according to the model proposed by (Siegel and Ciolfi, 2016a,b) (corresponding to their "fiducial" case; see text). The solid curves represent the contributions of different energy bands to the total light-curve (dashed line).

two important transitions. The first, around ~ 10 s, marks the end of the early baryon wind phase and the beginning of the spindown phase. The second, at several times 10^4 s, corresponds to the time when the ejecta become optically thin.

While the emission described by the above model is essentially isotropic, allowing us to set $\varepsilon_c \sim 1$, only a fraction of BNS mergers ε_{LLNS} is expected to generate a long-lived NS. The value of this fraction mainly depends on the unknown NS EOS and distribution of component masses, which leaves a considerable uncertainty. Here, we assume for simplicity a one-to-one correspondence between the fraction ε_{LLNS} and the fraction of SGRBs accompanied by a long-lasting X-ray transient (i.e. extended emission and/or X-ray plateau). Following the analysis presented in (Rowlinson et al., 2013), we assign $\varepsilon_{LLNS} \sim 50\%$.

Once we set $\varepsilon_{sr} = \varepsilon_{LLNS}$, the resulting total efficiency of the emission is $\varepsilon \sim \varepsilon_{sr} \cdot \varepsilon_c \sim 50\%$.

Results

We now proceed with the application of `saprEMo` to the chosen EM transient (discussed in the previous Section 5.2.3) with the aim of predicting the expected detection occurrence of this type of signal in different present and future surveys or observational campaigns. In order to emphasise the impact of the survey properties, we keep fixed throughout our calculations not only the light curve, but also the assumed astrophysical rate and the efficiency. In particular, we consider:

- two present surveys, collected during the decade of operation of XMM-Newton, for providing predictions on available data;

- the *Chandra* Deep Field - South (CDF-S) for verifying if the transient class discovered by (Bauer et al., 2017) is statistically consistent with the SC16 model;

- 1 year of THESEUS observations, for testing the sensitivity of this mission concept to transients associated to BNS mergers, such as SC16.

BNS merger rate model For these investigations we assume a constant rate of BNS mergers in the range $R_V(z) = 100 - 10000 \ \mathrm{Gpc^{-3}yr^{-1}}$ which extends up to a maximum z of $z \sim 6$. This wide range approximates the local rate interval inferred with the detection of GW170817 ($[320, 4740] \ \mathrm{Gpc^{-3}yr^{-1}}$ at 90% probability (Abbott et al., 2017f)) and is broadly consistent also with values obtained by different studies ((Abbott et al., 2016i),(Abadie et al., 2010b),(Chruslinska et al., 2017),(Paul, 2017)). Our information of the rate dependence over redshift is even more poorly constrained, from the observation point of view. For this reason we adopt a simplified model constant in redshift. As a representative case, we report distributions and results for $R_V(z) = 1000 \ \mathrm{Gpc^{-3}yr^{-1}}$. This rate is shown in fig. 5.4, where is compared to three other scenarios:
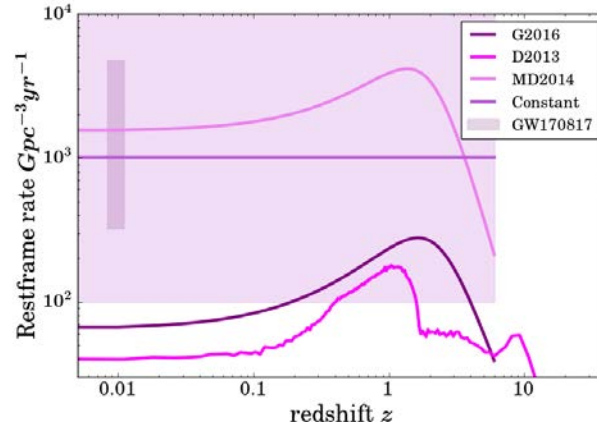
Figure 5.4: BNS merger rate as a function of redshift for different models: D2013 (Dominik et al., 2013) in magenta, G2016 (Ghirlanda et al., 2016) in purple, MD2014 convolved with $P(t_{del}) \propto t_{del}^{-1}$ in pink, our default constant model in violet and light shadowed area to include the whole range and the 90% interval obtained from the analysis of GW170817 thistle. For this latter case the rate range has been plotted at the location of the GW170817 source.

D2013 the standard model, *high-end* metallicity evolution scenario, proposed by (Dominik et al., 2013) outlined in the context of population synthesis;

G2016 the analytic approximation based on SGRB observations described in eq. (12) of (Ghirlanda et al., 2016) (adopting the average value of the parameter reported for case *a* with an opening angle of 4.5 deg);

MD2014 the analytic prescription for the star formation history proposed by (Madau and Dickinson, 2014) convolved with a probability distribution of delay time given by the power low $P(t_{del}) \propto t_{del}^{-1}$, with a minimum time of 20×10^6 *yr*. The distribution adopted in this work has been then normalised to the local BNS merger rate estimated with GW170817 of 1540 Gpc^{-3}yr^{-1}.

Because we consider a constant $R_V(z)$, the results for the upper (lower) bound of the whole range $R_V(z) = 100 - 10000$ Gpc^{-3}yr^{-1}, can be obtained by scaling up (down) the output quantities by one order of magnitude. Our analyses assume a flat cosmology with: $H_0 = 70$ km s^{-1} Mpc^{-1},

$\Omega_M = 0.3$, $\Omega_\Lambda = 0.7$ and, consequently $\Omega_k = 0.0$.

Absorption model In section 5.2.2, we describe a general procedure to account for hosting and galactic hydrogen column densities. More specific absorption models can be implemented accordingly to the energy range of interest. In (Willingale et al., 2013), the authors investigate hundreds of GRB afterglows detected by Swift to model the effective total galactic column density in X-ray $n_{H_{tot},MW}$. The atomic and molecular hydrogens represents the dominant components of $n_{H_{tot},MW} \approx n_{H,MW} + 2\ n_{H_2,MW}$. In `saprEMo` we adopt the model proposed by (Willingale et al., 2013) to estimate the molecular hydrogen component from the atomic contribution

$$n_{H_2,MW} = n_{H_2max} \left[1 - \exp\left(\frac{n_{H,MW}}{n_c} \right) \right]^\alpha \qquad (5.13)$$

where $n_{H_2max} = 7.5\ 10^{20}$ molecules/cm^2, $n_c = 2.37\ 10^{21}$ atoms/cm^2 and $\alpha = 2$.

The effective cross section of the interstellar medium, for each of the energy bands included in the range $0.03 - 10$ keV, is analytically estimated as a function of energy E:

$$\sigma_{ISM}(E)[cm^2] = (c_0 + c_1 E + c_2 E^2)E^{-3}\ 10^{24} \qquad (5.14)$$

as reported in (Morrison and McCammon, 1983).

XMM-Newton We apply `saprEMo` to two different surveys of data collected during the life-time of XMM-Newton.

XMM-Newton Serendipitous Source Catalog (3XMM DR7) These data have been collected during pointed observations (hereafter PO) made between 3/2/2000 and 15/12/2016 ((Consortium, 2017), (Rosen

et al., 2016)). The survey properties are summarised in tab. 5.3 and tab. 5.4.

XMM-Newton Slew Survey Clean Source Catalog, v2.0 These data have been collected while changing target in the sky (hereafter SLEW), according to XMM-Newton observation program ((A. P. Smale, the Astrophysics Science Division at NASA/GSFC, the High Energy Astrophysics Division of the Smithsonian Astrophysical Observatory, 2017), (Saxton et al., 2008; Read and Saxton, 2016; Saxton et al., 2017)). The survey properties are summarised in tab. 5.5 and tab. 5.6.

In tab. 5.1 we report the number of signals predicted by `saprEMo` for PO and SLEW surveys. In both cases, the statistical uncertainties due to the assumed Poisson distribution are almost negligible compared to the systematics due to the ε and BNS merger rate uncertainties.

Although the data have been collected by the same instrument, PO and SLEW considerably differ in terms of exposure time (and therefore sensitivity), sky coverage and energy responses, as shown by tables in appendix 5.2.6. Table 5.1 shows that in PO, peaks and tails have similar expectation values. This is because the typical exposure time of pointed observations is comparable to the duration of the emission. Completely different is instead the situation for SLEW observations, which are characterised by a much shorter average exposure time. Because SLEW typical observations only last for few seconds, the probability of detecting a signal exactly at its luminosity peak is considerably lower compared to the chance of observing it at any other time of the emission. For this reason, in the SLEW survey tails dominate over peaks.

The difference in SLEW and PO sensitivities are reflected in the information carried by the two surveys and quantified in the graphs reported in figure 5.5. Although the SLEW survey is less sensitive, the rapid ac-

|	XMM-Newton	
	PO	SLEW
$\mathbf{N_p}$	8	0.05
$\mathbf{N_t}$	25	120

Table 5.1: Average numbers of observations expected in PO and SLEW surveys. The Poisson statistic of the actual number of peaks and tails present in the survey S implies a standard deviation equal to the square root of these values.

quisition of such data has allowed to scan a much wider area of the sky, so that the total number of expected signals in the survey is actually considerably higher compared to the correspondent PO values (see tab. 5.1). SLEW observations, assuming correct identification (see sec. 5.2.4), could indeed already reveal a consistent population of BNS merger events. Because PO observations are longer and (therefore) deeper, the survey scans a larger volume in redshift, considerably exploring cosmological distances. In particular, the bottom graph of figure 5.5a implies that, under the assumption of a constant cosmic BNS merger rate, such signals, if present in the survey, have about the same probability of being originated from $z < 2$ and $z > 2$. The double bump in the tail distribution is explained by the blue and yellow curves which respectively represent the duration of the signal above the threshold at a fixed redshift z, $D_{sig}^{obs}(z)$, and $\alpha R_V(z)\, dVc/dz$ (where α is $\varepsilon\, CSA$ and $CSA \sim \tilde{n}_{obs} FoV/4\pi$ is the Covered Sky Area). Given our simplified BNS merger rate model, the yellow and black lines scale like the redshift derivative of the comoving volume, since in both cases only constants multiply the element dV_c/dz. The blue curve has instead a very peculiar behaviour which depends on the specific emission light curve compared to the limit fluxes of the survey. The distinct trends in the blue lines of fig. 5.5, are due to features very peculiar to the adopted light curve (fig. 5.3). When the flux, of the thermal second peak, drops down the limit, it generates the first change in the overall visible duration, which happens at $z \sim 0.5$ and $z \sim 0.05$ for PO and SLEW respectively. The second turn over in the overall duration,

very clear in PO, is instead due to the discretisation of the light curves in energy bins and the low hardness ratio of these transients. Specifically $z \sim 4$ is when the first energy bin characterising the light curve ($L_{h=0}$) exits the band of the instrument ($z = (E'_{max,h=0}/E^I_{min}+1) \sim (1 \,\mathrm{keV}/0.2-1)$ taking $E'_{max,h=0}$ the maximum energy of the h bin and $E'_{max,h=0} = 1$ keV the minimum detectable energy by the instrument $E^I_{min} = 0.2$ keV). Instead the SLEW limits in fluxes determine the sensitivity to a closer population of BNS mergers, mainly localised at $z < 2$, which are consequently characterised by higher flux values. Fluxes in PO are distributed differently according to their peak or tail nature. Interestingly, `saprEMo` predicts a PO flux distribution of peaks whose typical value is considerably higher than the sensitivity limits, enhancing the actual possibility of detecting them. A longer campaign with the same observational properties of PO, would therefore allow to reveal signals, similar to SC16, generated up to considerable cosmic distances with enough details to allow an identification. For what concerns PO, and similarly deep surveys, the factor which impacts the most on the fraction of visible N_{BNS_m} is the FoV.

Chandra and the new, faint X-ray population Bauer et al. (2017) have recently claimed the discovery of a new X-ray transient class in the Chandra Deep Field - South (CDF-S), a deep survey of a well localized sky region composed of 102 observations collected in different periods during the last decade. Interestingly, the main properties of the event presented in Bauer et al. (2017) are broadly consistent with the emission model proposed by SC16. The maximum luminosity of $\sim 10^{47}$ erg/s, the spectral peak around ~ 2 keV (source frame), the rise time of ~ 100 s, and the overall duration of $\sim 10^4$ s are all in broad agreement with the model predictions. Here we do not attempt to provide convincing evidence for
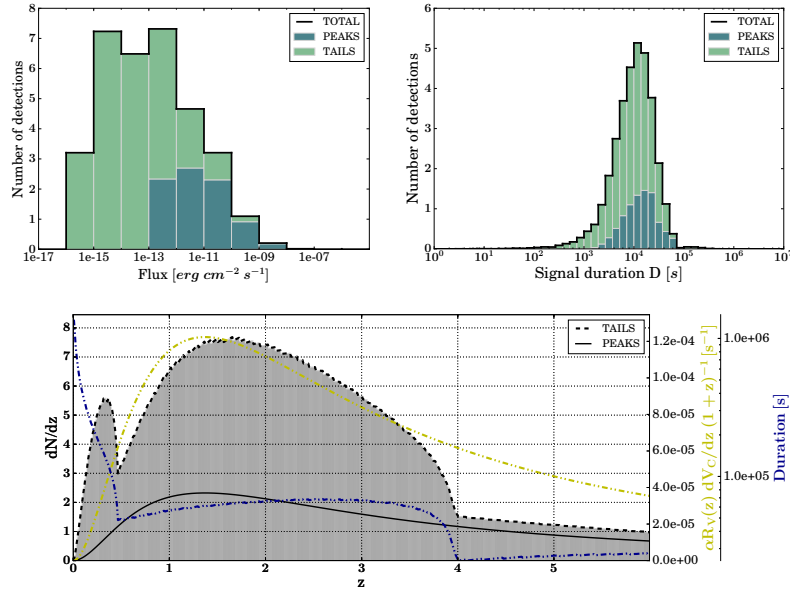
(a) Results for observations in XMM-Newton PO survey.
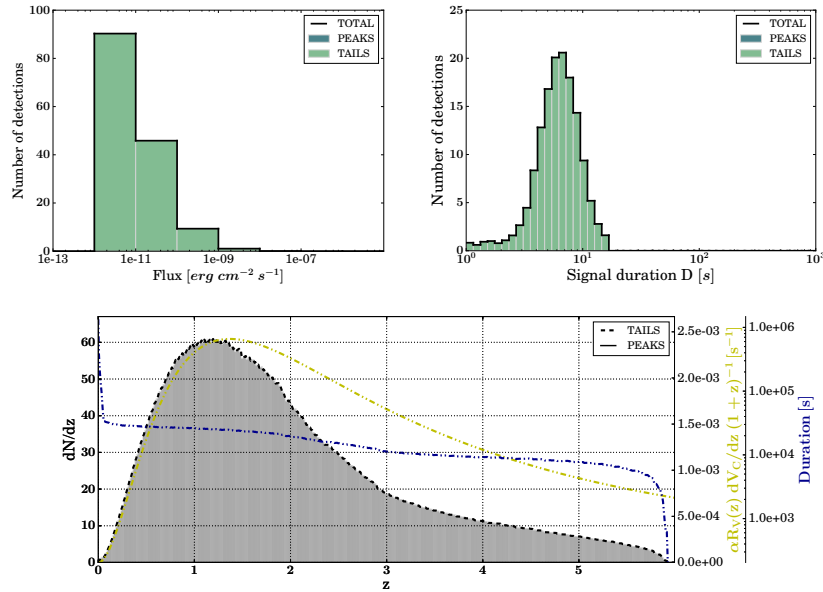
(b) Results for observations in XMM-Newton SLEW survey. Because of the low expected values for peaks compared to tails (see table 5.1), the black solid line in bottom graph is not visible.

Figure 5.5: Comparison between expected signal distributions in PO and SLEW surveys. The upper-left panel shows the flux distributions obtained summing peak (dark green) and tail (green) contributions. The upper-right panel shows the expected duration of peak and tail distributions in transparency one over the other. The redshift distributions in the bottom panel represents the differential contribution of peaks and tails throughout the scanned comoving volume of Universe). The yellow and blue curves have been added to explain the trend of the tail number and represent respectively the scaled argument of the z integral 5.11 and the duration $D_{sig}^{obs}(z)$. The different properties of PO and SLEW surveys are reflected in the diverse flux, duration and redshift distributions.

a potential match, but we take advantage of the above indications to show another interesting case for exploiting the capabilities of `saprEMo`. By assuming that this transient was produced according to the emission model of SC16, we can check the probability of such an observation, for given BNS merger rate, cosmology, and so on. For simplicity, we assume a signal analogous to the SC16 fiducial case adopted throughout this paper only rescaled to have a maximum luminosity of 10^{47} erg/s (referred to as "rescaled SC16 model/signal" in the following).

To test the rate consistency between the detected X-ray transient and the rescaled SC16 model, we apply `saprEMo` to the CDF-S, adopting a galactic neutral column density of $n_{H_{tot},MW} \approx n_{H,MW} \sim 8.8 \times 10^{19}$ cm^{-2}, as reported in (Bauer et al., 2017). Our results and conclusions do not consider any association (or missed association) to other electromagnetic counterparts. Because of the presence of a luminosity maximum and of the upper limits claimed at previous time, we need to evaluate only the peak component. We can therefore consider the total ~ 7 Ms of CDF-S as a single observation. `saprEMo` predicts an expectation value of ~ 0.14 signals in the CDF-S. Given the adopted constant rate model, the probability of one rescaled SC16 signal being present at its luminosity peak in the ~ 7 Ms of the CDF-S is $\sim 12\%$ (with probability of 0 signals of 87%). Considering the whole range of allowed BNS merger rates, this value ranges from $\sim 1.4\%$ (with probability of 0 signals of 98.6%) and $\sim 35\%$ (with probability of 0 signals of 25%). Despite the broad consistency of the transient revealed by (Bauer et al., 2017) with the SC16 emission model, our analysis shows that a real association between the two is rather unlikely, although not completely inconsistent given the uncertainties over rate and emission model. Assuming instead that the detected transient is exactly the rescaled SC16 signal adopted in the above calculation, the constant BNS merger rate value required to have one event in the CDF-S

(expectation value $N_p = 1$) is ~ 7100 Gpc^3 yr^{-1}, higher than the one inferred from GW170817 (see section 5.2.3).

Future observations with THESEUS In the last few years, many wide-FoV X-ray missions have been proposed to monitor the X-ray sky, and specifically to follow up GRBs and GWs ((Feng et al., 2016; Barcons et al., 2012; Yuan et al., 2015; Merloni et al., 2012)). In particular, the mission concept THESEUS has been recently presented to explore the transient high-energy sky and contribute to the multi-messenger astronomy (Amati et al., 2017; Stratta et al., 2017). We therefore apply `saprEMo` to test the sensitivity of such mission to BNS mergers emitting in the X-ray according to the SC16 model. On THESEUS payload, the Soft X-ray Imager (SXI) would be the instrument sensitive to such emission. From fig. 4 of (Amati et al., 2017), we extrapolated SXI flux sensitivity as a function of the exposure time with a broken power-law, in the conservative case of typical Galactic plane absorption ($N_H = 5 \times 10^{22}$ cm^{-2}). We explore 1 year of THESEUS operation (given a 100% duty cycle), assuming two different observational campaigns (both of which avoid effective [6] overlaps in sky locations, see appendix 5.2.6 for more details):

Case a: a year of pointing toward the same sky position, allowing for a deeper survey in flux;

Case b: a year broken down into 30 observations of $\sim 10^6$ s each.

We report the expectation values of N_p and N_t for both cases **a** and **b** in tab. 5.2 and show redshift distributions of N_p in fig. 5.6.

Tab. 5.2 shows that the expectation value of peaks for both the hypothetical THESEUS campaigns are several orders of magnitude higher than the ones predicted for present surveys (see XMM-Newton PO and SLEW in tab. 5.1 and CDF-S in 5.2). This highlights the huge impact of the FoV

---

[6]Case **b** includes region overlaps but assumes a separation in time between observations of the same sky location of roughly 6 months.

	Chandra	**THESEUS**	
	CDF-S	Case a	Case b
$\mathbf{N_p}$	0.14	26500	23000
$\mathbf{N_t}$	✘	16	290
FoV [deg^2]	0.08	3300	
$\mathbf{n_{obs} \langle T_{obs} \rangle}$ [s]	$\sim 6.73 \times 10^6$	$\sim 31.5 \times 10^6$	

	XMM-Newton PO		
Rate model	MD2014	D2013	G2016
$\mathbf{N_p}$	20	0.8	1.5
$\mathbf{N_t}$	65	2.3	4.9
FoV [deg^2]	MOS 0.3, PN: 0.2		
$\mathbf{n_{obs} \langle T_{obs} \rangle}$ [s]	$\sim 234 \times 10^6$		

	THESEUS Case a		
Rate model	MD2014	D2013	G2016
$\mathbf{N_p}$	62000	2250	4800
$\mathbf{N_t}$	50	1.7	3.4

Table 5.2: Expected values for peaks (N_p) and tails (N_t) for different surveys and rate models. *Top*: Chandra Deep Field - South (CDF-S) and 1 year of THESEUS operation for a single observation (case a), and 30 distinct observations (case b). *Middle* and *bottom*: comparison of expectation values assuming different BNS merger rate models, from left to right (i) constant default model; (ii) standard rate model population, based on the population synthesis study (Dominik et al., 2013), at high metallicity scenario (D2013) and (iii) model based on SGRB statistics (Ghirlanda et al., 2016) with opening angle of 4.5 deg (G2016). Numbers have been rounded accordingly to the statistical standard deviation expected in the survey.

on the detections of relatively rare phenomena such as BNS mergers. The discrepancy between the results obtained for THESEUS and the present surveys is indeed consistent with the differences in FoV and total time of observations: indeed THESEUS FoV is more than 4 orders of magnitude larger than the cameras in Chandra and XMM-Newton, while total observing time favour present survey compared to one full year of THESEUS observations by just a factor of ~ 10.

With the numbers in tab 5.2, `saprEMo` proves that the characteristics of the mission concept THESEUS suit the target of X-ray emission generated during BNS mergers. It also demonstrates that for instruments
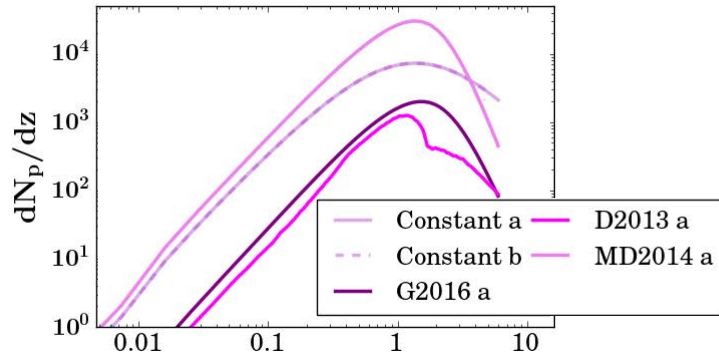
Figure 5.6: Expected redshift distribution for peak signals of 1 year of THESEUS observations. Because of our detection definition, all the events in the FoV are visible until the peak flux on the emission is above the sensitivity threshold. In the default configuration of constant BNS merger rates (solid and dashed violet lines), we test 2 different observing strategies, changing position on the sky results in a lower flux limit which is indeed reflected by the different maximum distance which could be reached by the two surveys of data. We also report the peak distribution as a function of redshift in the case of the other tested BNS merger models: D2013 in magenta, MD2014 in pink and G2016 in purple.

provided by a FoV and flux-exposure time relation similar to THESEUS's one, longer observation periods localised in specific regions of the sky, increase the number of detectable sources in the FoV, even accounting for the tail contribution. Indeed the lower fluxed reached with a single observation (case a) allows to detected signals at further cosmological distances, as shown in (fig. 5.6) . This difference between case a and b is also reflected in the flux distributions, which only differ by the presence of events at lower fluxes. In both a and b cases, the peak contribution dominates over the tails. Given our assumption of constant rate, the distribution of peaks over redshift (fig. 5.6) follows the comoving volume dependence over redshift, so that also signals generated at relatively high redshift would be detected. The redshift distribution of tails in THESEUS observations follows a trend similar to the SLEW one, because of the similar values of flux limits.

5.2.4   Discussion

With `saprEMo`, we tested the sensitivity of different astronomical surveys to the emission model SC16. The analysis has outlined that the introduced tail component dominates over peaks when the typical exposure time of the catalog is considerably shorter than the duration of the emission model, as in the case of XMM-Newton SLEW. However tails are generally more difficult to recognise; they often appear as simple decaying signals, which can be even more easily misinterpreted and associated to other X ray transients (e.g. tails of tidal disruption events (Lodato and Rossi, 2011), SNae (Dwarkadas and Gruszko, 2011) etc..). Moreover the tail durations can last just few seconds, because of their definition. This means that even in long observations, some of these signals could require a dedicated transient analyses (as the EXTraS group has carried out (De Luca, 2014) Understanding this citation (De Luca et al., 2016)) to be revealed over the integrated background flux. The identification of tails is even more challenging when the observations last only few seconds, as is the case for the SLEW survey. Indeed some emission models, as SC16, predict a time evolution of the emission properties which would likely result in detections of signals considerably different from each other and therefore hard to associate. The identification issue is mitigated in the case of campaigns characterised by typically longer observations, such as the XMM-Newton PO and Chandra CDF-S. The extension of the typical exposure time to thousands of seconds and the finer subdivision in energy bands, allow for the acquisition of more informative data, which should be sufficient for a direct model comparison.

For the fiducial light curve of SC16, the majority of the signal duration is given by the second non-thermal peak. However the luminosity of such signal part is several orders of magnitude dimmer compared to the main peak. Therefore, although from the duration we would have expected the tails to be dominated by such non-thermal component of the emission model, the flux sensitivity

compared to its intensity actually makes this part of the light curve difficult to be detect at cosmological distances. This is shown by the rapid decay (within $z \sim 0.5$ even for the most sensitive surveys) of the duration reported in the bottom graphs of fig. 5.5.

Our first analyses demonstrate that, with some simple assumptions, few detections can already constrain the wide range of constant BNS merger rate considered in this study. For example, assuming the emission model proposed by (Siegel and Ciolfi, 2016b), the probability of detecting more than 3 peaks in XMM-Newton PO at the lowest limit of our constant rate range $(100 \ \mathrm{Gp^{-3}yr^{-1}})$ is less than 1.2%. Assuming ε not higher then 0.5, the identification of few peak emissions generated during BNS mergers in PO would therefore set a new lower limit on it. Moreover explaining the presence of few peaks in PO through considerations over the emission model would be quite challenging. Indeed the proposed emission model already achieves luminosity as high as $\sim 10^{48} erg/s$, setting the possibility of detecting signals generated at redshifts as high as $z \sim 15$ with PO sensitivities.

Similar constrains can be obtained also assuming the association of the Chandra X-ray transient with the SC16 emission model. In this case our analysis can put a lower limit over the BNS merger rate of $\sim 750 \ \mathrm{Gp^{-3}yr^{-1}}$ at 90% credible interval, assuming a constant rate up to $z \sim 6$. The peak luminosity of the SC16 emission is indeed bright enough to actually be visible throughout all the considered comoving volume, even once accounted for the Milky Way absorption. However such a value $(\sim 750 \ \mathrm{Gp^{-3}yr^{-1}})$ hinges on `saprEMo` inputs, which therefore constitute our assumptions, and is particularly sensitive (inversely proportional) to changes over ε. As for PO, also in the CDF-S, detections definitely associated to BNS mergers would considerably reduce the uncertainties over the lower limit of BNS merger rate, since our predictions are based on optimistic ε and L_p. Moreover peak results only depend on the maximum and its energy distribution of the emission model, being completely

unaffected by the details of the light curves. With the analysed present surveys of data, the BNS merger rate can only be marginally constrained by few confirmed detections, while the zero-signal case is consistent with the whole constant range for both PO and CDF-S (not for SLEW, where however there is the complication of the identification). A completely different scenario is expected for future surveys collected with missions dedicated to multi-messenger and multi-wavelength astronomy, as THESEUS. As demonstrated by the numbers in the tab. 5.2, observing campaigns, such as case a and b, will allow population studies, which will likely constrain both BNS merger rate and emission models. The high number of expected detections should allow a strong classification procedure, able to identify signals generated by the same sources while capturing differences of individual systems. The prospective of this rich future population of signals hints to the possibility of inferring information also on BNS merger rate as a function of redshift (and therefore also on ε), assuming that multi-wavelength observations will allow some redshift associations.

To test the impact of the model of BNS merger rate, we apply `saprEMo` to PO and THESEUS, case a, assuming the three additional scenarios previously introduced (sec. 5.2.3): D2013, G2016 and MD2014, assuming a time delay probability distribution of $P(t_{del}) \propto t_{del}^{-1}$ (Madau and Dickinson, 2014). The four rate models, together with the local BNS merger range constrained by GW170817, are reported in fig. 5.4. The absolute expectation values reported in tab. 5.2, reflect the trend of the rate models reported in fig. 5.4. All the considered rates are affected by considerable uncertainties or assumptions, we therefore avoid conclusions on scaling, though noticing that D2013 and G2016 are inconsistent with the local rate range obtained with GW170817. Qualitatively speaking the peculiarities of the different BNS merger rate models are reflected in the flux distributions of peaks and tails. Peak distributions are easier to interpret, since they are not directly convoluted with emission properties specific of the proposed models. Looking at the flux distributions

of peaks in PO we indeed notice that there are correlation between the redshift and the flux distributions. For example, broader maxima in the BNS merger rate correspond to wider maxima in the flux distribution and also, lower the redshift correspondent to the highest rate, the more are the signals detected at higher fluxes. However, the analysis and comparison of that results obtained with the two surveys of data (PO and THESEUS case a), emphasises that even assuming the unrealistic case of a single light curve characterising all the emitting BNS merger systems many there is a considerable degree of degeneracy between the parameters which can affect the flux distribution, as spectral sensitivity of the survey in different energy bands and absorption. BNS merger rate models are therefore hard to be distinguished directly from flux distributions. With the case of THESEUS, we also demonstrate that `saprEMo` can be used to determine advantages and disadvantages compared to a particular emission, of adopting different observational strategies. Given a fixed mission duration, different observational strategies result in different traits among the catalog properties; in particular the exposure time swings the balance between flux limit and sky coverage of the survey. Specifically we proved that for SC16 sources, with THESEUS SXI sensitivity as a function of exposure time, an extended observation of the same sky location would be more effective than scanning a wider area of the sky with typical exposure times of $\sim 10^6$ s. Indeed the expectation values for peaks and tails in the two cases show that the increased tails (of case b) do not match up with the sources available with a deeper flux limit (of case a).

With `saprEMo`, it is possible to investigate also the impact of other key survey properties, such as FoV (see sections 5.2.3 or 5.2.4) and division in energy bands. We test the horizon of the surveys in terms of flux and energy bands by considering an unrealistic constant BNS merger rate up to $z \sim 20$. Although the average CDF-S flux limit is almost an order of magnitude lower than the one of XMM-Newton PO, the maximum redshift that the two surveys can reach

with the peak luminosity of the fiducial SC16 is almost identical ($z_{max} \sim 7$). This is due to the sensitivity of PO to a lower energy band ($[0.2 - 0.5]$ keV). Despite the significant absorption of such energy band, the instrument sensitivity at those frequencies considerably impacts the survey capability of detecting SC16 signals, which indeed show a spectral distribution strongly peaked at low X-ray energies (see fig. 5.3). Further tests also demonstrate that the sensitivity to the proposed emission model (at least within our detection definition) is improved when the spectral range of the survey sensitivity is divided in more bands.

5.2.5   Summary and Outlook

In this study we have shown some inferences that can be achieved by applying our tool `saprEMo` on specific emission models and surveys. In terms of multi-messenger astronomy, our results show that the luminosities predicted by the SC16 emission model can be detected up to cosmological distances which extend much further than the horizon of present ((Aasi et al., 2016)) and future gravitational-wave detectors ((Sathyaprakash et al., 2012)), both in the cases of current surveys, such as CDF-S and XMM-Newton PO and SLEW, and concept missions, such as THESEUS. In this first application we show that `saprEMo` provides theoretical predictions allowing us to:

- to compare predictions with actual data. E.g. we proved that some signals consistent with the model could already be detected in present surveys of data such as XMM-Newton PO and SLEW;

- to test potential associations. E.g. we proved that the new transient found by (Bauer et al., 2017) is only marginally consistent with the model;

- and to assess the effectiveness of proposed mission concepts for a specific type of signal. World-wide initiatives have been and are going to be pro-

posed to contribute to the new field of multi-messenger astronomy. It is therefore becoming more and more crucial to be able to evaluate the performances of these proposed mission concepts (in X-ray other interesting cases are e.g. eRosita (Cappelluti et al., 2011)). With the case study of THESEUS, we demonstrate that `saprEMo` well suits this task. The mission concept THESEUS is very effective for catching bright and isotropic signals, as SC16, associated with BNS mergers (see also (Stratta et al., 2017)). The large FoV of THESEUS SXI would allow for the detection of up to thousands of signals, enabling considerable constrains on both the BNS merger rate and the emission models.

In general `saprEMo` allows us to test both survey and astrophysical properties. This study has mainly focused on the former, exploring the impact of different trade offs among such properties (including exposure time, sky localisation, and spectral sensitivity), assuming a single light-curve model from SC16. However `saprEMo` can also test (and infer overall values) astrophysical quantities such as absorption, which can be modelled in different ways, or light-curve characteristics such as emission duration, peak luminosity and spectra. In the presence of unknown quantities such as emission or rate models, the flexibility of `saprEMo` allows to test every single scenario, given the other assumptions are true.

Once the design sensitivity of Advanced interferometers will be achieved, detections of EM bright sources will occur more and more often and very likely at lower SNRs. In this context, identifying specific emission model will become more and more crucial for the multi-messenger astronomy. Statistical studies, such as the one carried out with `saprEMo`, can contribute to a more informed expectation of the astronomical community, by constraining models comparing predictions with archived data, allowing a more optimised search of EM counterparts of GWs. Predicting the presence of particular emission in specific surveys of data can also point out margins of improvements in search and

analysis methods, potentially revealing new sources (as happened in the search of pulsars in radio data, by implementing a more sensitive analysis (Knispel et al., 2013)). Such considerations on analysis are particularly powerful once the emission model has already matched, at least once, with the data. With the EM emissions associated to GW170817, `saprEMo` could indeed be used to analyse the peculiar GRB 170817A and how often we should have expected to detect similar signals, testing the different hypotheses (including geometrical arguments on viewing angle) proposed to explain its weakness in energy. The connected issue of lack of detection of off-axis GRBs can actually be analysed independently from GW170817 with `saprEMo`, again to review theoretical models or improve the dedicated analysis. It is indeed important to quantify and be aware of biases in data analysis procedures, to correctly evaluate astrophysical quantities derived from observations which might be affected by them, such as rates. Similar investigations have therefore the potential of contributing to our overall understanding of mechanisms occurring in mergers of BNS and their formation/evolution.

We conclude remarking that the flexibility of the implemented methodology allows considerations of emission model spanning the whole electromagnetic spectrum, so that also kilonovae models can be tested. Moreover our analysis include no priors on nature of EM sources, so that it can be applied to a wide range of phenomena, including emission not related to compact binary coalescences, such as supernovea or fast radio bursts, for which, for example it could test different proposed origins. With its analysis dedicated to treat high redshift effects, `saprEMo` particularly suits studies on emission of cosmological origin. `saprEMo` can be applied to sources characterised by any duration, however the signal duration is a parameter which has to be taken into account when statistically considering tails [7].

---

[7]Indeed depending on timing and sky locations of the surveys, long emissions might be detected (and counted in `saprEMo` tail outputs) multiple times.

5.2.6   Appendix

XMM-Newton parameters

In this section we report the parameters adopted to apply `saprEMo` to XMM-Newton surveys: SLEW and PO. The information have been collected by dedicated website and files. To analyse PO, we apply the absorption model to source locations of the clean data set [8] the catalogs (Rosen et al., 2016).

PARAMETER	VALUE
Minimum energy	0.2 keV
Maximum energy	12 keV
$\langle T_{obs} \rangle$ [a]	19000 s
$\sigma^2_{T_{obs}}$ [a]	17900 s
Covered Sky area	1750 (1032^b) $\deg^2$

Table 5.3: **PO:** general characteristics of pointed observations contributing to the XMM-Newton Serendipitous Source Catalog. The data are part of the 3XMM-DR7 catalogue (Rosen et al., 2016); we adopted the fit file $3xmmdr7\_obslist.fits$ available at (XMM-Newton SSC Consortium, 2017b).
a: From clean observations (OBS_CLASS < 3);
b: Excluding overlaps.

ENERGY BAND [keV]	SENSITITY [erg cm^{-2} s^{-1}]
$0.2 - 0.5$	5.8×10^{-16}
$0.5 - 1.0$	1.7×10^{-15}
$1.0 - 2.0$	2.7×10^{-15}
$2.0 - 4.5$	3.8×10^{-15}
$4.5 - 12.0$	6.6×10^{-15}

Table 5.4: **PO:** spectral bands of pointed observations contributing to the XMM-Newton Serendipitous Source Catalog. Medians in each band from catalog as suggested from website (A. P. Smale, 2017b), catalog available at (XMM-Newton SSC Consortium, 2017a) catalog : $3XMM\_DR7$ cleaned with the same criteria used for calculating average and variance of exposure times

Similarly, to analyse the SLEW survey we use the clean observations collected in the catalog $xmmsl2\_clean.fits$ found at (A. P. Smale, the Astrophysics Science Division at NASA/GSFC, the High Energy Astrophysics Division of the Smithsonian Astrophysical Observatory, 2017) [9].

---

[8]Catalog requirement: CLEAN = OBS_CLASS < 3.

[9]Data concerning average and standard deviation of observations are based on total band (Exp_Map_B8). Locations adopted for the absorption model are inferred from source locations.

PARAMETER	VALUE
Minimum energy	0.2 keV
Maximum energy	12 keV
$\langle T_{obs} \rangle$ [a]	6.9 s
$\sigma^2_{T_{obs}}$ [a]	2.4 s
Covered Sky area	84% of the sky

Table 5.5: **SLEW:** general characteristics of slew data contributing to the XMM-Newton Slew Survey Catalogue.
a: from clean observations according to *xmmsl2_clean.fits* file at (A. P. Smale, the Astrophysics Science Division at NASA/GSFC, the High Energy Astrophysics Division of the Smithsonian Astrophysical Observatory, 2017);
b: percentage when overlaps are excluded from (A. P. Smale, the Astrophysics Science Division at NASA/GSFC, the High Energy Astrophysics Division of the Smithsonian Astrophysical Observatory, 2017)

ENERGY BAND [keV]	SENSITITY [erg cm^{-2} s^{-1}]
$0.2 - 2.0$	1.2×10^{-12}
$2.0 - 12.0$	9.3×10^{-12}

Table 5.6: **SLEW:** spectral bands of slew data contributing to the XMM-Newton Slew Survey Catalogue. Medians in each band from website (A. P. Smale, the Astrophysics Science Division at NASA/GSFC, the High Energy Astrophysics Division of the Smithsonian Astrophysical Observatory, 2017). The energy range in SLEW catalog is divided just in 2 bands.

CHANDRA

To apply `saprEMo` to the CDF-S we use data from (A. P. Smale, 2017a),(Lehmer et al., 2005) and (Luo et al., 2016). As quoted in the same references, we adopted $N_H = 8.8 \times 10^{19}$. Following the link at (A. P. Smale, 2017a), it is possible to find more details on the set of observations.

(A. P. Smale, 2017a)

PARAMETER	VALUE
Minimum energy	0.5 keV
Maximum energy	7 keV
FoV	285 arcmin^2
$\langle T_{obs} \rangle$	6.727×10^6 s
n_{obs}	1

Table 5.7: **CHANDRA CDF-S:** FoV and energy range from (Lehmer et al., 2005), total time from (Luo et al., 2016).

ENERGY BAND [keV]	SENSITITY [erg cm^{-2} s^{-1}]
$0.5 - 2.0$	6.7×10^{-17}
$2.0 - 7.0$	5.7×10^{-16}
$0.5 - 7.0$	3.1×10^{-16}

Table 5.8: **CHANDRA CDF-S:** median fluxes of source distribution in every energy band, from figure 14 (Lehmer et al., 2005).

THESEUS

The data concerning THESEUS have been extrapolated from (Amati et al., 2017). We analyse a 1 year of observations collected with two different strategies:

a) 1 single observation lasting the whole year;

b) 30 distinct observations of $\sim 10^6$ s each.

In the following we report the adopted properties:

PARAMETER	VALUE
Minimum energy	0.3 keV
Maximum energy	6 keV
FoV	110×30 deg^2

Table 5.9: **THESEUS:** general properties from (Amati et al., 2017).

	$\langle T_{obs} \rangle$ [s]	n_{obs}	SENSITIVITY [erg cm^{-2} s^{-1}]
Case a.	31.54×10^6	1	1×10^{-13}
Case b.	1.05×10^6	30	6×10^{-13}

Table 5.10: **THESEUS:** properties of the two proposed observational campaigns. Sensitivity extrapolated from fig 4 (Amati et al., 2017).

General consideration on data treatment

For each of the considered survey, we use as many energy bands as available. Sources are indeed usually detected first in one of the refined band.

The results obtained by applying `saprEMo` to present surveys of data, do not directly depend on the actual sky- locations of the observations. We do not

account for different probabilities of detecting signals related to galaxy distributions. We instead rely on exploring cosmological distances and therefore on the isotropy of our Universe. We however use sky location of observations in the case of XMM-Netwon surveys to estimate the absorption due to the Milky Way. Although we don't expect source locations to reflect the same distribution of the sky-positions of the observations (more sources are expected from an observation in the galactic plane or pointing toward dense populated regions, like galaxies or stellar clusters), we adopt them when data on observations are not clear/available. This should imply an slightly over estimation of the local absorption, since more sources are generally expected on the galactic plane.

For the cases reported in this paper, we consider the bias introduced by this procedure negligible compared to uncertainties and other assumptions.

Chapter 6

Conclusions and final remarks

With the opening the era of gravitational-waves, we have not only started revealing so far unexplored astrophysical phenomena, but also begun combining independent information to formulate a faithful and coherent representation of our Universe. To efficiently achieve this ultimate goal, an effective analysis of the data is fundamental. Focusing on GW transients, up to now, most of the investigation strategies have been developed in view of a handful of initial gravitational-wave detections. With the rapid growth of the field, we are now in the process of transitioning from this peculiar regime to a high number of available sources, more similar to classical astronomy. The challenges we are starting to face are less concerned with detection and more with managing characterisation and interpretation of a population of events. In fact, the rate estimates inferred with the first observing runs imply a high number of future gravitational-wave detections (Abbott et al., 2016j). In this context, effective data treatment and combination of information, deduced by different channels and analyses, are therefore becoming key challenges for the science revealed by present and future GW-detectors. We will need to face computational and organisational challenges, starting from the ones pointed out by the first observing runs of the advanced interferometer. We need to prepare the infrastructures necessary to carry out those statistical studies which, I believe,

will soon dominate the science inferred from gravitational-waves.

Estimation of the source parameters is the first step toward signal interpretation. My experience in this topic consists in the project presented in chapter 3. We develop a multi-banding strategy, dedicated to effectively down-sample the Fourier components necessary to faithfully represent a GW waveform, exploiting its well-known chirping behaviour. Implementing this approach, we demonstrate that it is possible to mitigate the computational issues related to such type of analysis for generic GW waveform models, without requiring storage of pre-calculated templates (e.g. ROM (Canizares et al., 2015b)).

Machine learning techniques are gaining popularity among the gravitational-wave community as effective tools for efficiently manipulating data. They are particularly useful for dealing with large amounts of data and, indeed, one of their most common applications in GW data analysis is in the classification and recognition of noisy events. However in view of the promising GW astronomy, signal characterisation might also benefit from such tools. In chapter 4, we present one possible application of machine learning techniques for mitigating the impact of non-Guassian noise tails in GW transient searches. We use artificial neural networks to recognise, as a first case study, chirping features in the time-frequency representation generated by the analysis of the pipeline cWB. We prove that the signal characterisation can significantly enhance the significance of GW candidates in generic burst searches, especially once combined with other statistical properties in a multi-variate analysis. An overall strategy combining both signal and noise classification might therefore boost the analysis performed by all-sky searches, potentially improving our sensitivity to GW sources of any kind. Such ideas can be further developed in view of different scientific targets such as supernovae and signals emitted by compact binary coalescences characterised by extreme or rare parameters (such as eccentricity, high masses, high mass ratio, etc.), for which the efficiency between match filtering techniques and unmodelled approaches is expected to be at

least comparable. Such peculiar CBC sources can potentially shed light on many queries involved in our understanding of the Universe. Targeting such signals also offers the perfect opportunity to promote and develop an effective infrastructure to efficiently combine information extracted from completely different analyses. Indeed, I believe that connections and interactions are the basis for the development of our future knowledge, not only in astronomy but in any scientific field. Sharing information is becoming increasingly more crucial and fruitful, giving different communities the opportunity to learn how to deal with specific problems, new to a particular subject, with tools already developed in other contexts. Among the most challenging quests that we will have to address in the near future is how to effectively combine information coming from: (i) different GW analyses, (ii) different EM studies and most importantly (iii) gravitational and electromagnetic investigations. Although the first two observing runs of the advanced interferometers already gave us the opportunity to test such group interactions, there are considerable margins of improvements, for example in the speed of communication between the communities or in the organisation between the several astronomical groups involved in the search for EM counterparts of GWs. Despite the exceptional success of the discoveries related to GW170817, EM follow-ups, especially for further sources, were and are expected to be challenging, due to the large sky localisation area normally provided by the only analysis of GWs (Abbott et al., 2016j). This issue is emphasised by the several uncertainties affecting predictions on EM emissions expected in relation to gravitational-wave events. The lack of a defined counterpart model particularly affects spectral bands characterised by many contaminants (such as the optical band). Although after the multi-wavelength observations in association with GW170817 and GRB 170817A (Abbott et al., 2017h), some of these have been solved, many other quests remain open, including emissions strictly dependent on the nature of the BNS merger remnant. To strengthen the bridge between astronomical observations

and theoretical models, we developed `saprEMo`. The tool, presented in chapter 5, consists in a *s*implified *a*lgorithm for *pr*edicting electromagnetic (*EM*) *o*bservations. It aims to estimate the number of electromagnetic events, given a specific emission model, which are expected in a particular survey of data. The initial goal of the project was to provide predictions between expected and real observations, to constrain source rate or EM emission models. However the tool has been designed and implemented in targeting generic transients, so that it can actually be applied to any type of EM source peaking in any spectral band. The flexibility of the `saprEMo` allows its application for a variety of tasks, including probing the sensitivity of future mission concepts, comparing different observational strategies and testing statistical consistency between observations and the proposed nature of correspondent sources. Generic tools such `saprEMo` can be applied to a series of interesting queries; for example it can shed light on astronomical questions, such as why off-axis GRBs had never been detected before the unclear case of GRB 170817A. Moreover it can be applied to test consistency between population synthesis results and astronomical observations.

All these projects gave me the opportunity to widen my background and develop different professional skills, such as managing and summarising large amounts of data (see chapters 3 and 5) and dealing with astronomical catalogues (see chapter 5). They also gave me the opportunity to meet and collaborate with people from different institutions such us the University of Trento, for burst analysis of the project described in chapter 4, and the Gran Sasso Institute/University of Urbino, for the development of the tool `saprEMo` as presented in chapter 5.

As member of the LIGO Scientific Collaboration, I have been involved in the recent discoveries and personally felt the rapid development of the field. Al-

though we have already accomplished incredible achievements, a lot more is still to come. I hope to devote my experience and connections to effectively contribute to the development of such infrastructures under various aspects, enabling a more effective analysis and interpretation of the many gravitational-wave events that we expect to detect. I want to keep contributing to our understanding and interpretation of this new information, particularly focusing on revealing the physics behind gravitational-waves generated by coalescences of compact binaries with innovative data analysis techniques. I aim to maximise the science coming from present and future observations by developing data analysis strategies to investigate the science of gravitational-waves, in the upcoming statistical regime. I would like to contribute in setting up an efficient framework to analyse gravitational-wave information, taking advantage of this new era of multi-messenger astronomy and of cutting edge techniques already applied in different fields. To do that, I plan to collaborate with different groups, including the ones I have been in contact during my PhD and for the development of the projects mentioned in this work.

My ideas and myself in these last three years have considerably evolved. The PhD programme at the University of Birmingham has helped me in opening my mind, giving me a broad background on astrophysical topics and more. As during all properly worthwhile experiences, during my PhD I had to face several challenges: giving talks, being independent, developing code, learning new languages, etc... These challenges have led my professional and personal growth. For this reason I would like to conclude this work thanking again all people which have allowed me to have such as insightful experience: from my supervisors, Ilya Mandel, John Veitch and Alberto Vecchio, to the EU commission and people leading the GraWIToN project, with which I have been financed, Michele Punturo, Elena Cuoco and Erika Morucci. Finally I would like to also thank again all my colleagues, who made my whole PhD

much more fun and productive than it was supposed to be, and the people that I met in conferences and collaborations with other groups. You are many but you all contributed to make this experience extraordinary.

Thank you.

Bibliography

A. Buonanno, B. R., Iyer, E. Ochsner, Y. P., and Sathyaprakash, B. S. (2009). Comparison of post-newtonian templates for compact binary inspiral signals in gravitational-wave detectors. Physical Review D, 80(8):084043.

A. P. Smale, the Astrophysics Science Division at NASA/GSFC, t. H. E. A. D. o. t. S. A. O. (2017a). Chandfs7ms - chandra deep field-south 7-megasecond x-ray source catalog. `https://heasarc.gsfc.nasa.gov/W3Browse/chandra/chandfs7ms.html`. Online; accessed November 2017.

A. P. Smale, the Astrophysics Science Division at NASA/GSFC, t. H. E. A. D. o. t. S. A. O. (2017b). XMMSSC - XMM-Newton Serendipitous Source Catalog (3XMM DR7 Version). `https://heasarc.gsfc.nasa.gov/W3Browse/xmm-newton/xmmssc.html`. Online; accessed November 2017.

A. P. Smale, the Astrophysics Science Division at NASA/GSFC, the High Energy Astrophysics Division of the Smithsonian Astrophysical Observatory (2017). XMMSLEWCLN - XMM-Newton Slew Survey Clean Source Catalog, v2.0). `https://heasarc.gsfc.nasa.gov/w3browse/all/xmmslewcln.html`. Online; accessed November 2017.

Aasi, J. et al. (2015a). Advanced ligo. Classical and Quantum Gravity, 32(7):074001.

Aasi, J. et al. (2015b). Characterization of the ligo detectors during their sixth science run. Classical and Quantum Gravity, 32(11):115012.

Aasi, J. et al. (2015c). Characterization of the LIGO detectors during their sixth science run. Class. Quant. Grav., 32(11):115012.

Aasi, J. et al. (2016). Prospects for Observing and Localizing Gravitational-Wave Transients with Advanced LIGO and Advanced Virgo. Living Rev. Relat., 19:1.

Abadie, J. et al. (2010a). All-sky search for gravitational-wave bursts in the first joint ligo-geo-virgo run. Physical Review D, 81(10):102001.

Abadie, J. et al. (2010b). Predictions for the rates of compact binary coalescences observable by ground-based gravitational-wave detectors. Classical and Quantum Gravity, 27(17):173001.

Abadie, J. et al. (2012a). All-sky search for gravitational-wave bursts in the second joint ligo-virgo run. Physical Review D, 85(12):122007.

Abadie, J. et al. (2012b). All-sky search for gravitational-wave bursts in the second joint ligo-virgo run. Physical Review D, 85(12):122007.

Abadie, J. et al. (2012c). First low-latency LIGO+ Virgo search for binary inspirals and their electromagnetic counterparts. Astron. Astrophys., 541:A155.

Abadie, J. et al. (2012d). Search for gravitational waves from intermediate mass binary black holes. Physical Review D, 85(10):102004.

Abbott, B. P. et al. (2009a). LIGO: The Laser interferometer gravitational-wave observatory. Rept. Prog. Phys., 72:076901.

Abbott, B. P. et al. (2009b). An upper limit on the stochastic gravitational-wave background of cosmological origin. Nature, 460(7258):990.

Abbott, B. P. et al. (2016a). Astrophysical implications of the binary black hole merger gw150914. The Astrophysical Journal Letters, 818(2):L22.

Abbott, B. P. et al. (2016b). Binary Black Hole Mergers in the first Advanced LIGO Observing Run. Phys. Rev., X6(4):041015.

Abbott, B. P. et al. (2016c). Characterization of transient noise in advanced ligo relevant to gravitational wave signal gw150914. Classical and Quantum Gravity, 33(13):134001.

Abbott, B. P. et al. (2016d). Observation of gravitational waves from a binary black hole merger. Physical review letters, 116(6):061102.

Abbott, B. P. et al. (2016e). Observing gravitational-wave transient gw150914 with minimal assumptions. Physical Review D, 93(12):122004.

Abbott, B. P. et al. (2016f). Properties of the binary black hole merger GW150914. Phys. Rev. Lett., 116:241102. https://dcc.ligo.org/LIGO-P1500218/public/main.

Abbott, B. P. et al. (2016g). The rate of binary black hole mergers inferred from advanced ligo observations surrounding gw150914. arXiv preprint arXiv:1602.03842.

Abbott, B. P. et al. (2016h). Tests of general relativity with GW150914. Phys. Rev. Lett., 116:221101.

Abbott, B. P. et al. (2016i). Upper limits on the rates of binary neutron star and neutron star–black hole mergers from advanced ligo's first observing run. The Astrophysical Journal Letters, 832(2):L21.

Abbott, B. P. et al. (2017a). Exploring the sensitivity of next generation gravitational wave detectors. Classical and Quantum Gravity, 34(4):044001.

Abbott, B. P. et al. (2017b). Gravitational waves and gamma-rays from a binary neutron star merger: Gw170817 and grb 170817a. The Astrophysical Journal Letters, 848(2):L13.

Abbott, B. P. et al. (2017c). Gw170104: observation of a 50-solar-mass binary black hole coalescence at redshift 0.2. Physical Review Letters, 118(22):221101.

Abbott, B. P. et al. (2017d). Gw170608: Observation of a 19 solar-mass binary black hole coalescence. The Astrophysical Journal Letters, 851(2):L35.

Abbott, B. P. et al. (2017e). Gw170814: A three-detector observation of gravitational waves from a binary black hole coalescence. Physical review letters, 119(14):141101.

Abbott, B. P. et al. (2017f). Gw170817: observation of gravitational waves from a binary neutron star inspiral. Physical Review Letters, 119(16):161101.

Abbott, B. P. et al. (2017g). Gw170817: observation of gravitational waves from a binary neutron star inspiral. Physical Review Letters, 119(16):161101.

Abbott, B. P. et al. (2017h). Multi-messenger observations of a binary neutron star merger. Astrophysical Journal Letters, 848(2):L12.

Abbott, B. P. et al. (2017i). Search for intermediate mass black hole binaries in the first observing run of advanced ligo. Physical Review D, 96(2):022001.

Abbott, P. B. et al. (2016j). Prospects for observing and localizing gravitational-wave transients with advanced ligo and advanced virgo. Living Rev. Relativity, 19(1).

Accadia, T. et al. (2012). Virgo: a laser interferometer to detect gravitational waves. JINST, 7:P03012.

Acernese, F. et al. (2005). A hierarchical bayesian framework for nonlinearities identification in gravitational wave detector outputs. Classical and Quantum Gravity, 22(18):S1223.

Acernese, F. et al. (2014). Advanced virgo: a second-generation interferometric gravitational wave detector. Classical and Quantum Gravity, 32(2):024001.

Adams, T., Buskulic, D., Germain, V., Guidi, G. M., Marion, F., Montani, M., Mours, B., Piergiovanni, F., and Wang, G. (2016). Low-latency analysis pipeline for compact binary coalescences in the advanced gravitational wave detector era. Class. Quant. Grav., 33(17):175012.

Adams, T. et al. (2013). Gravitational-wave detection using multivariate analysis. Physical Review D, 88(6):062006.

Affeldt, C. et al. (2014). Advanced techniques in geo 600. Classical and quantum gravity, 31(22):224002.

Agathos, M., Del Pozzo, W., Li, T. G. F., Van Den Broeck, C., Veitch, J., and Vitale, S. (2014). TIGER: A data analysis pipeline for testing the strong-field dynamics of general relativity with gravitational wave signals from coalescing compact binaries. Phys. Rev. D, 89(8):082001.

Allen, B. (1997). The stochastic gravity-wave background: sources and detection. In Relativistic Gravitation and Gravitational Radiation, Proceedings of the Les Houches School of Physics, held in Les Houches, Haute Savoie, volume 26, pages 373–418.

Amati, L. et al. (2017). The Transient High Energy Sky and Early Universe Surveyor (THESEUS).

Andersson, N. et al. (2013). The transient gravitational-wave sky. Classical and Quantum Gravity, 30(19):193002.

Antoniadis, J., Freire, P. C. C., Wex, N., Tauris, T. M., Lynch, R. S., van Kerkwijk, M. H., Kramer, M., Bassa, C., Dhillon, V. S., Driebe, T., Hessels, J. W. T., Kaspi, V. M., Kondratiev, V. I., Langer, N., Marsh, T. R., McLaughlin, M. A., Pennucci, T. T., Ransom, S. M., Stairs, I. H., van Leeuwen, J., Verbiest, J. P. W., and Whelan, D. G. (2013). A Massive Pulsar in a Compact Relativistic Binary. Science, 340:448.

Antonini, F., Toonen, S., and Hamers, A. S. (2017). Binary black hole mergers from field triples: Properties, rates, and the impact of stellar evolution. The Astrophysical Journal, 841(2):77.

Armano, M. et al. (2016). Sub-femto-g free fall for space-based gravitational wave observatories: Lisa pathfinder results. Physical Review Letters, 116(23):231101.

Aso, Y., Michimura, Y., Somiya, K., Ando, M., Miyakawa, O., Sekiguchi, T., Tatsumi, D., and Yamamoto, H. (2013). Interferometer design of the KAGRA gravitational wave detector. Phys. Rev. D, 88(4):043007.

Astone, P. et al. (2010). Igec2: A 17-month search for gravitational wave bursts in 2005–2007. Physical Review D, 82(2):022003.

Audley, H. et al. (2017). Laser interferometer space antenna. arXiv preprint arXiv:1702.00786.

Baird, E., Fairhurst, S., Hannam, M., and Murphy, P. (2013). Degeneracy between mass and spin in black-hole-binary waveforms. Phys. Rev. D, 87(2):024035.

Baker, P. T. et al. (2015). Multivariate Classification with Random Forests for Gravitational Wave Searches of Black Hole Binary Coalescence. Phys. Rev., D91(6):062004.

Barcons, X. et al. (2012). Athena (advanced telescope for high energy astrophysics) assessment study report for esa cosmic vision 2015-2025. arXiv preprint arXiv:1207.2745.

Barkett, K. et al. (2016). Gravitational waveforms for neutron star binaries from binary black hole simulations. Physical Review D, 93(4):044064.

Barrault, M., Maday, Y., Nguyen, N. C., and Patera, A. T. (2004). An empirical interpolation'method: application to efficient reduced-basis discretization of partial differential equations. Comptes Rendus Mathematique, 339(9):667–672.

Barrett, J. W., Gaebel, S. M., Neijssel, C. J., Vigna-Gómez, A., Stevenson, S., Berry, C. P. L., Farr, W. M., and Mandel, I. (2017). Accuracy of inference on the physics of binary evolution from gravitational-wave observations. arXiv preprint arXiv:1711.06287.

Bauer, F. E. et al. (2017). A new, faint population of x-ray transients. Monthly Notices of the Royal Astronomical Society, 467(4):4841–4857.

Belczynski, K. et al. (2016a). Compact binary merger rates: comparison with ligo/virgo upper limits. The Astrophysical Journal, 819(2):108.

Belczynski, K. et al. (2016b). The first gravitational-wave source from the isolated evolution of two stars in the 40–100 solar mass range. Nature, 534(7608):512.

Belczynski, K., Kalogera, V., and Bulik, T. (2002). A comprehensive study of binary compact objects as gravitational wave sources: evolutionary channels, rates, and physical properties. The Astrophysical Journal, 572(1):407.

Belczynski, K. and Bulik, T. and Fryer, C. L. and Ruiter, A. and Valsecchi, F. and Vink, J. S. and Hurley, J. (2010). On the maximum mass of stellar black holes. The Astrophysical Journal, 714(2):1217.

Berger, E. (2014). Short-duration gamma-ray bursts. Annual review of Astronomy and Astrophysics, 52:43–105.

Berry, C. P. L. et al. (2015). Parameter Estimation for Binary Neutron-star Coalescences with Realistic Noise during the Advanced LIGO Era. Astrophys. J., 804(2):114.

Betz, E. (2016). Even Einstein doubted his gravitational waves. Astronomy.

Bildsten, L. (1998). Gravitational radiation and rotation of accreting neutron stars. The Astrophysical Journal Letters, 501(1):L89.

Blackman, J. et al. (2017). Numerical relativity waveform surrogate model for generically precessing binary black hole mergers. Physical Review D, 96(2):024058.

Buonanno, A., Cook, G. B., and Pretorius, F. (2007). Inspiral, merger, and ring-down of equal-mass black-hole binaries. Physical Review D, 75(12):124018.

Buonanno, A. and Sathyaprakash, B. S. (2014). Sources of gravitational waves: theory and observations. arXiv preprint arXiv:1410.7832.

Canizares, P., Field, S. E., Gair, J., Raymond, V., Smith, R., and Tiglio, M. (2015a). Accelerated Gravitational Wave Parameter Estimation with Reduced Order Modeling. Phys. Rev. Lett., 114:071104.

Canizares, P., Field, S. E., Gair, J., Raymond, V., Smith, R., and Tiglio, M. (2015b). Accelerated gravitational wave parameter estimation with reduced order modeling. Physical review letters, 114(7):071104.

Canizares, P., Field, S. E., Gair, J. R., and Tiglio, M. (2013). Gravitational wave parameter estimation with compressed likelihood evaluations. Phys. Rev. D, 87:124005.

Cannon, K., Chapman, A., Hanna, C., Keppel, D., Searle, A. C., and Weinstein, A. J. (2010). Singular value decomposition applied to compact binary coalescence gravitational-wave signals. Phys. Rev. D, 82:044025.

Cannon, K., Emberson, J. D., Hanna, C., Keppel, D., and Pfeiffer, H. P. (2013). Interpolation in waveform space: Enhancing the accuracy of gravitational waveform families using numerical relativity. Phys. Rev. D, 87(4):044008.

Cannon, K. et al. (2012a). Toward Early-warning Detection of Gravitational Waves from Compact Binary Coalescence. Astrophys. J., 748(2):136.

Cannon, K., Hanna, C., and Keppel, D. (2012b). Interpolating compact binary waveforms using the singular value decomposition. Phys. Rev. D, 85(8):081504.

Cappelluti, N. et al. (2011). erosita on srg. a x-ray all-sky survey mission. Memorie della Societa Astronomica Italiana Supplementi, 17:159.

Casares, J. and Jonker, P. (2014). Mass measurements of stellar and intermediate-mass black holes. Space Science Reviews, 183(1-4):223–252.

Chen, H. Y. and Holz, D. E. (2014). The Loudest Gravitational Wave Events. arXiv preprint arXiv:1409.0522.

Chengalur, J. N., Kanekar, N., and Roy, N. (2013). Accurate measurement of the h i column density from h i 21 cm absorption-emission spectroscopy. Monthly Notices of the Royal Astronomical Society, 432(4):3074–3079.

Chruslinska, M., Belczynski, K., Klencki, J., and Benacquista, M. (2017). Double neutron stars: merger rates revisited. Monthly Notices of the Royal Astronomical Society.

Ciolfi, R. (2016). X-ray Flashes Powered by the Spindown of Long-lived Neutron Stars. ApJ, 829:72.

Ciolfi, R. and Siegel, D. M. (2015). Short Gamma-Ray Bursts in the "Time-reversal" Scenario. ApJ, 798:L36.

Cognola, G. (2015/2016). General relativity and cosmology (lecture notes). `http://www.science.unitn.it/~cognola/DIDATTICA/RGeng.pdf`. Univerity of Trento.

Consortium, X.-N. S. (2017). XMMSSC - XMM-Newton Serendipitous Source Catalog (3XMM DR7 Version). `https://heasarc.gsfc.nasa.gov/w3browse/all/xmmssc.html`.

Corral-Santana, J. M., Casares, J., Muñoz-Darias, T., Bauer, F. E., Martinez-Pais, I. G., and Russell, D. M. (2016). Blackcat: A catalogue of stellar-mass black holes in x-ray transients. Astronomy & Astrophysics, 587:A61.

Cutler, C. and Flanagan, E. E. (1994). Gravitational waves from merging compact binaries: How accurately can one extract the binary's parameters from the inspiral waveform? Physical Review D, 49(6):2658.

Danzmann, K. et al. (1996). Lisa: Laser interferometer space antenna for gravitational wave measurements. Classical and Quantum Gravity, 13(11A):A247.

De Luca, A. (2014). Exploring the x-ray transients and the variable sky. `http://www.extras-fp7.eu`.

De Luca, A., Salvaterra, R., Tiengo, A., D'Agostino, D., Watson, M. G., Haberl, F., and Wilms, J. (2016). Science with the extras project: Exploring the x-ray transient and variable sky. In The Universe of Digital Sky Surveys, pages 291–295. Springer.

Demorest, P. B., Pennucci, T., Ransom, S. M., Roberts, M. S. E., and Hessels, J. W. T. (2010). A two-solar-mass neutron star measured using Shapiro delay. Nature, 467:1081–1083.

Dominik, M., Belczynski, K., Fryer, C., Holz, D. E., Berti, E., Bulik, T., Mandel, I., and O'Shaughnessy, R. (2013). Double compact objects. ii. cosmological merger rates. The Astrophysical Journal, 779(1):72.

Drago, M. (2009). Reconstruction of gravitational wave bursts with ligo-virgo network. `https://dcc.ligo.org/public/0003/G0900548/005/Drago_Amaldi09_LIGO-G0900548-v5.pdf`.

Drago, M. (2010). Search for transient gravitational wave signals with unknown waveform in the ligo-virgo network of interferometric detectos using a fully coherent algorithm. `http://paduaresearch.cab.unipd.it/2916/1/tesi_completa.pdf`.

Dwarkadas, V. V. and Gruszko, J. (2011). What are published x-ray light curves telling us about young supernova expansion? Monthly Notices of the Royal Astronomical Society, 419(2):1515–1524.

Einstein, A. (1916). Näherungsweise integration der feldgleichungen der gravitation. Wiley Online Library.

Einstein, A. (1918). Über gravitationswellen. Sitzungsberichte der Königlich Preußischen Akademie der Wissenschaften (Berlin), Seite 154-167.

Evangelista, E. F. D. and de Araujo, J. C. N. (2015). Stochastic background of gravitational waves generated by eccentric neutron star binaries. Monthly Notices of the Royal Astronomical Society, 449(3):2700–2705.

Faber, J. A. and Rasio, F. A. (2012). Binary neutron star mergers. Living Reviews in Relativity, 15(1):8.

Farr, W. M., Stevenson, S., Miller, M. C., Mandel, I., Farr, B., and Vecchio, A. (2017). Distinguishing spin-aligned and isotropic black hole populations with gravitational waves. Nature, 548(7667):426.

Feng, H. et al. (2016). extp: Enhanced x-ray timing and polarimetry mission.

Field, S. E., Galley, C. R., Herrmann, F., Hesthaven, J. S., Ochsner, E., and Tiglio, M. (2011). Reduced Basis Catalogs for Gravitational Wave Templates. Phys. Rev. Lett., 106:221102.

Finkelstein, D. (1958). Past-future asymmetry of the gravitational field of a point particle. Physical Review, 110(4):965.

Flanagan, E. E. and Hughes, S. A. (1998). Measuring gravitational waves from binary black hole coalescences. i. signal to noise for inspiral, merger, and ringdown. Physical Review D, 57(8):4535.

Foster, R. S. and Backer, D. C. (1990). Constructing a pulsar timing array. The Astrophysical Journal, 361:300–308.

Gerstenshtein, M. E. and Pustovoit, V. I. (1963). On the detection of low frequency gravitational waves. Journal of Experimental and Theoretical Physics, 16(2):433–435.

Ghirlanda, G. et al. (2016). Short gamma-ray bursts at the dawn of the gravitational wave era. Astronomy & Astrophysics, 594:A84.

Golfarelli, M. (2017/18). Data mining: Materiale didattico. `http://bias.csr.unibo.it/golfarelli`.

Gompertz, B. P., O'Brien, P. T., and Wynn, G. A. (2014). Magnetar powered GRBs: explaining the extended emission and X-ray plateau of short GRB light curves. MNRAS, 438:240–250.

Hannam, M., Husa, S., Ohme, F., and Ajith, P. (2010). Length requirements for numerical-relativity waveforms. Phys. Rev. D, 82(12):124052.

Hannam, M., Schmidt, P., Bohé, A., Haegel, L., Husa, S., Ohme, F., Pratten, G., and Pürrer, M. (2014). Simple model of complete precessing black-hole-binary gravitational waveforms. Phys. Rev. Lett., 113(15):151101.

Hartwig, T., Volonteri, M., Bromm, V., Klessen, R. S., Barausse, E., Magg, M., and Stacy, A. (2016). Gravitational waves from the remnants of the first stars. Monthly Notices of the Royal Astronomical Society: Letters, 460(1):L74–L78.

Haster, C. J., Mandel, I., and Farr, W. M. (2015). Efficient method for measuring the parameters encoded in a gravitational-wave signal. Class. Quant. Grav., 32(23):235017.

Hild, S. (2012). Beyond the second generation of laser-interferometric gravitational wave observatories. Classical and Quantum Gravity, 29(12):124006.

Hinderer, T. et al. (2016). Effects of neutron-star dynamic tides on gravitational waveforms within the effective-one-body approach. Phys. Rev. Lett., 116(18):181101.

Hulse, R. A. and Taylor, J. H. (1975). Discovery of a pulsar in a binary system. The Astrophysical Journal, 195:L51–L53.

I. Bratko, R. S. M. and Kubat, M. (1999). Machine learning and data mining: methods and applications.

Jenet, F. A. et al. (2005). Detecting the stochastic gravitational wave background using pulsar timing. The Astrophysical Journal Letters, 625(2):L123.

Kalberla, P. M. W., Burton, W. B., Hartmann, D., Arnal, E. M., Bajaja, E., Morras, R., and Pöppel, W. G. L. (2005). The leiden/argentine/bonn (lab) survey of galactic hi-final data release of the combined lds and iar surveys with improved stray-radiation corrections. Astronomy & Astrophysics, 440(2):775–782.

Kerr, R. P. (1963). Gravitational field of a spinning mass as an example of algebraically special metrics. Physical review letters, 11(5):237.

Kisaka, S., Ioka, K., and Nakar, E. (2016). X-ray-powered macronovae. The Astrophysical Journal, 818(2):104.

Klimenko, S. et al. (2016). Method for detection and reconstruction of gravitational wave transients with networks of advanced detectors. Physical Review D, 93(4):042004.

Knispel, B. et al. (2013). Einstein@ home discovery of 24 pulsars in the parkes multi-beam pulsar survey. The Astrophysical Journal, 774(2):93.

Kostas, D. K. (2002). Gravitational wave physics. Encyclopedia of Physical Science and Technology, 3rd Edition, 7.

Kotsiantis, S. B., Zaharakis, I., and Pintelas, P. (2007). Supervised machine learning: A review of classification techniques. Emerging artificial intelligence applications in computer engineering, 160:3–24.

Kruskal, M. D. (1960). Maximal extension of schwarzschild metric. Physical review, 119(5):1743.

L. Gualtieri, E. M. Kantor, M. E. G. and Chugunov, A. I. (2014). Quasinormal modes of superfluid neutron stars. Physical Review D, 90(2):024010.

Lai, D. and Wiseman, A. G. (1996). Innermost stable circular orbit of inspiraling neutron-star binaries: Tidal effects, post-newtonian effects, and the neutron-star equation of state. Physical Review D, 54(6):3958.

Laycock, S. G. T., Maccarone, T. J., and Christodoulou, D. M. (2015). Revisiting the dynamical case for a massive black hole in ic10 x-1. Monthly Notices of the Royal Astronomical Society: Letters, 452(1):L31–L35.

Lehmer, B. D. et al. (2005). The extended chandra deep field-south survey: Chandra point-source catalogs. The Astrophysical Journal Supplement Series, 161(1):21.

LIGO (2015). Instrument Science White Paper. `https://dcc.ligo.org/public/0113/T1400316/004/T1400316-v5.pdf`.

LIGO Scientific Collaboration. LIGO. `https://www.ligo.org`.

Lipunov, V. M., Postnov, K. A., and Prokhorov, M. E. (1997). Formation and coalescence of relativistic binary stars: The effect of kick velocity. Monthly Notices of the Royal Astronomical Society, 288(1):245–259.

Lodato, G. and Rossi, E. M. (2011). Multiband light curves of tidal disruption events. Monthly Notices of the Royal Astronomical Society, 410(1):359–367.

Lü, H.-J., Zhang, B., Lei, W.-H., Li, Y., and Lasky, P. D. (2015). The Millisecond Magnetar Central Engine in Short GRBs. ApJ, 805:89.

Luo, B. et al. (2016). The chandra deep field-south survey: 7 ms source catalogs. The Astrophysical Journal Supplement Series, 228(1):2.

Madau, P. and Dickinson, M. (2014). Cosmic star-formation history. Annual Review of Astronomy and Astrophysics, 52:415–486.

Maggiore, M. (2000). Gravitational wave experiments and early universe cosmology. Physics Reports, 331(6):283–367.

Mandel, I. and de Mink, S. E. (2016). Merging binary black holes formed through chemically homogeneous evolution in short-period stellar binaries. Monthly Notices of the Royal Astronomical Society, 458(3):2634–2647.

Mandic, V., Bird, S., and Cholis, I. (2016). Stochastic gravitational-wave background due to primordial binary black hole mergers. Physical review letters, 117(20):201102.

Mapelli, M. (2016). Massive black hole binaries from runaway collisions: the impact of metallicity. Monthly Notices of the Royal Astronomical Society, 459(4):3432–3446.

Mazzolo, G. (2013). Search for intermediate mass black hole binaries with networks of ground-based gravitational-wave detectors. PhD thesis, Observational Relativity and Cosmology, AEI-Hannover, MPI for Gravitational Physics, Max Planck Society.

Mazzolo, G. et al. (2014). Prospects for intermediate mass black hole binary searches with advanced gravitational-wave detectors. Physical Review D, 90(6):063002.

McLelland, D., Cavaglia, M., Evans, M., Schnabel, R., Lantz, B., Quetschke, V., and Martin, I. (2016). The LSC-Virgo White Paper on Instrument Science (2016-2017 edition). `https://dcc.ligo.org/LIGO-T1600119/public`.

Mennekens, N. and Vanbeveren, D. (2014). Massive double compact object mergers: gravitational wave sources and r-process element production sites. Astronomy & Astrophysics, 564:A134.

Merloni, A. et al. (2012). erosita science book: mapping the structure of the energetic universe. arXiv preprint arXiv:1209.3114.

Metzger, B. D. (2017). Kilonovae. Living Reviews in Relativity, 20(1):3.

Metzger, B. D. and Piro, A. L. (2014). Optical and X-ray emission from stable millisecond magnetars formed from the merger of binary neutron stars. MNRAS, 439:3916–3930.

Metzger, B. D., Quataert, E., and Thompson, T. A. (2008). Short-duration gamma-ray bursts with extended emission from protomagnetar spin-down. MNRAS, 385:1455–1460.

Miller, M. C. and Miller, J. M. (2015). The masses and spins of neutron stars and stellar-mass black holes. Physics Reports, 548:1–34.

Mino, Y. et al. (1997). Black hole perturbation. Progress of Theoretical Physics Supplement, 128:1–121.

Misner, C. W., Thorne, K. S., and Wheeler, J. A. (2017). Gravitation. Princeton University Press.

Morrison, R. and McCammon, D. (1983). Interstellar photoelectric absorption cross sections, 0.03-10 kev. The Astrophysical Journal, 270:119–122.

Moss, G. E., Miller, L. R., and Forward, R. L. (1971). Photon-noise-limited laser transducer for gravitational antenna. Applied Optics, 10(11):2495–2498.

Necula, V., Klimenko, S., and Mitselmakher, G. (2012a). Transient analysis with fast wilson-daubechies time-frequency transform. In Journal of Physics: Conference Series, volume 363, page 012032. IOP Publishing.

Necula, V., Klimenko, S., Mitselmakher, G., and Levin, J. (2012b). Gravitational waves from eccentric binary systems. Bulletin of the American Physical Society, 57.

Nelemans, G., Steeghs, D., and Groot, P. J. (2001). Spectroscopic evidence for the binary nature of am cvn. <u>Monthly Notices of the Royal Astronomical Society</u>, 326(2):621–627.

Nilsson, N. J. (1998). Introduction to machine learning. `http://robotics.stanford.edu/~nilsson/MLBOOK.pdf`.

Ohme, F. (2012). Analytical meets numerical relativity: status of complete gravitational waveform models for binary black holes. <u>Class. Quant. Grav.</u>, 29(12):124002.

Pan, Y. et al. (2011). Inspiral-merger-ringdown multipolar waveforms of non-spinning black-hole binaries using the effective-one-body formalism. <u>Physical Review D</u>, 84(12):124052.

Pannarale, F., Berti, E., Kyutoku, K., Lackey, B. D., and Shibata, M. (2015). Aligned spin neutron star-black hole mergers: A gravitational waveform amplitude model. <u>Physical Review D</u>, 92(8):084050.

Paul, D. (2017). Binary neutron star merger rate via the luminosity function of short gamma-ray bursts. <u>arXiv preprint arXiv:1710.05620</u>.

Piro, A. L., Giacomazzo, B., and Perna, R. (2017). The Fate of Neutron Star Binary Mergers. <u>ApJ</u>, 844:L19.

Porter, E. K. (2014). A New Method of Accelerated Bayesian Inference for Comparable Mass Binaries in both Ground and Space-Based Gravitational Wave Astronomy. <u>arXiv preprint arXiv:1411.0598</u>.

Postnov, K. A. and Yungelson, L. R. (2014). The evolution of compact binary star systems. <u>Living Reviews in Relativity</u>, 17(1):3.

Powell, J. et al. (2015). Classification methods for noise transients in advanced gravitational-wave detectors. <u>Classical and Quantum Gravity</u>, 32(21):215012.

Press, W. H., Teukolsky, S. A., Vetterling, W. T., and Flannery, B. P. (2007). <u>Numerical recipes 3rd edition: The art of scientific computing</u>. Cambridge university press.

Prestwich, A. H. et al. (2007). The orbital period of the wolf-rayet binary ic 10 x-1: dynamic evidence that the compact object is a black hole. <u>The Astrophysical Journal Letters</u>, 669(1):L21.

Prix, R. (2007). Search for continuous gravitational waves: Metric of the multidetector f-statistic. <u>Physical Review D</u>, 75(2):023004.

Punturo, M. et al. (2010). The Einstein Telescope: a third-generation gravitational wave observatory. <u>Class. Quant. Grav.</u>, 27(19):194002.

Punturo, M. et al. (2011). Einstein gravitational wave Telescope conceptual design study. `http://www.et-gw.eu/etdsdocument`.

Pürrer, M. (2014). Frequency-domain reduced order models for gravitational waves from aligned-spin compact binaries. <u>Classical and Quantum Gravity</u>, 31(19):195010.

Ravanini, F. (2008). General relativity and cosmology (lecture notes). `http://www.bo.infn.it/~ravanini/relativity/Generale.pdf`. Univerity of Bologna.

Read, A. M. and Saxton, R. D. (2016). EPIC-pn SLEW-specific PSF parameterisation. `https://www.cosmos.esa.int/web/xmm-newton/ccf-release-notes`.

Riles, K. (2013). Gravitational waves: Sources, detectors and searches. Progress in Particle and Nuclear Physics, 68:1–54.

Rodriguez, C. L., Chatterjee, S., and Rasio, F. A. (2016a). Binary black hole mergers from globular clusters: Masses, merger rates, and the impact of stellar evolution. Physical Review D, 93(8):084029.

Rodriguez, C. L., Haster, C. J., Chatterjee, S., Kalogera, V., and Rasio, F. A. (2016b). Dynamical formation of the gw150914 binary black hole. The Astrophysical Journal Letters, 824(1):L8.

Rodriguez, C. L., Morscher, M., Pattabiraman, B., Chatterjee, S., Haster, C.-J., and Rasio, F. A. (2015). Binary black hole mergers from globular clusters: implications for advanced ligo. Physical Review Letters, 115(5):051101.

Roger, P. (2002). Spectral methods for incompressible viscous flow.

Rojas, R. (2013). Neural networks: a systematic introduction. Springer Science & Business Media.

ROOT (2016). Tmultilayerperceptron class reference. `https://root.cern.ch/doc/master/classTMultiLayerPerceptron.html`.

Rosen, S. R. et al. (2016). The XMM-Newton serendipitous survey. VII. The third XMM-Newton serendipitous source catalogue. A&A, 590:A1.

Rosen, S. R. et al. (2016). The xmm-newton serendipitous survey-vii. the third xmm-newton serendipitous source catalogue. Astronomy & Astrophysics, 590:A1.

Rota, B. S. Appunti di reti neurali. `http://www.dsi.unive.it/$\sim$srotabul/files/AppuntiRetiNeurali.pdf`.

Rowlinson, A., O'Brien, P. T., Metzger, B. D., Tanvir, N. R., and Levan, A. J. (2013). Signatures of magnetar central engines in short GRB light curves. MNRAS, 430:1061–1087.

S. Klimenko, I. Yakushin, A. M. and Mitselmakher, G. (2008). A coherent method for detection of gravitational wave bursts. Classical and Quantum Gravity, 25(11):114029.

S. Klimenko, S. Mohanty, M. R. and Mitselmakher, G. (2005). Constraint likelihood analysis for a network of gravitational wave detectors. Physical Review D, 72(12):122002.

S. Rampone, V. Pierro, L. T. and Pinto, I. M. (2013). Neural network aided glitch-burst discrimination and glitch classification. International Journal of Modern Physics C, 24(11):1350084.

Sathyaprakash, B. et al. (2012). Scientific objectives of einstein telescope. Classical and Quantum Gravity, 29(12):124013.

Sathyaprakash, B. S. (2013). Gravitational waves and astrophysical sources. Comptes Rendus Physique, 14(4):272–287.

Saulson, P. R. (2011). Josh goldberg and the physical reality of gravitational waves. General Relativity and Gravitation, 43(12):3289–3299.

Saxton, R. D., Read, A. M., Esquej, P., Freyberg, M. J., Altieri, B., and Bermejo, D. (2008). The first xmm-newton slew survey catalogue: Xmmsl1. Astronomy & Astrophysics, 480(2):611–622.

Saxton, R. D., Read, A. M., Robrade, J., and Schmitt, J. H. M. M. (2017). Optical loading in the XMM-Newton slew source catalogue. `http://xmm2.esac.esa.int/docs/documents/CAL-TN-0210-0-1.ps.gz`.

Schutz, B. F. and Ricci, F. (2010). Gravitational waves, sources, and detectors. arXiv preprint arXiv:1005.4735.

Schwarzschild, K. (1916). Über das gravitationsfeld einer kugel aus inkompressibler flüssigkeit nach der einsteinschen theorie. In Sitzungsberichte der Königlich Preussischen Akademie der Wissenschaften zu Berlin, Phys.-Math. Klasse, 424-434 (1916).

Sesana, A. (2016). Prospects for Multiband Gravitational-Wave Astronomy after GW150914. Phys. Rev. Lett., 116:231102.

Siegel, D. M. and Ciolfi, R. (2016a). Electromagnetic emission from long-lived binary neutron star merger remnants. i. formulation of the problem. The Astrophysical Journal, 819(1):14.

Siegel, D. M. and Ciolfi, R. (2016b). Electromagnetic emission from long-lived binary neutron star merger remnants. ii. light curves and spectra. The Astrophysical Journal, 819(1):15.

Siemens, X., Mandic, V., and Creighton, J. (2007). Gravitational-wave stochastic background from cosmic strings. Physical Review Letters, 98(11):111101.

Sigurdsson, S. and Hernquist, L. (1993). Primordial black holes in globular clusters. Nature, 364(6436):423.

Silverman, J. M. and Filippenko, A. V. (2008). On ic 10 x-1, the most massive known stellar-mass black hole. The Astrophysical Journal Letters, 678(1):L17.

Smith, R., Field, S. E., Blackburn, K., Haster, C. J., Pürrer, M., Raymond, V., and Schmidt, P. (2016). Fast and accurate inference on gravitational waves from precessing compact binaries. Phys. Rev. D, 94(4):044031.

Smith, R. J. E., Cannon, K., Hanna, C., Keppel, D., and Mandel, I. (2013). Towards rapid parameter estimation on gravitational waves from compact binaries using interpolated waveforms. Phys. Rev. D, 87:122002.

Spera, M. and Mapelli, M. and Bressan, A. (2015). The mass spectrum of compact remnants from the PARSEC stellar evolution tracks. Monthly Notices of the Royal Astronomical Society, 451(4):4086–4103.

Stergiou, C. and Siganos, D. Neural networks. `https://www.doc.ic.ac.uk/~nd/surprise_96/journal/vol4/cs11/report.html`.

Stevenson, S., Berry, C. P. L., and Mandel, I. (2017). Hierarchical analysis of gravitational-wave measurements of binary black hole spin–orbit misalignments. Monthly Notices of the Royal Astronomical Society, 471(3):2801–2811.

Stone, N. C., Metzger, B. D., and Haiman, Z. (2016). Assisted inspirals of stellar mass black holes embedded in agn discs: solving the 'final au problem'. Monthly Notices of the Royal Astronomical Society, 464(1):946–954.

Stratta, G. et al. (2017). THESEUS: a key space mission for Multi-Messenger Astrophysics. ArXiv e-prints.

Sun, H., Zhang, B., and Gao, H. (2017). X-ray counterpart of gravitational waves due to binary neutron star mergers: Light curves, luminosity function, and event rate density. The Astrophysical Journal, 835(1):7.

Taylor, J. H. and Weisberg, J. M. (1982). A new test of general relativity-gravitational radiation and the binary pulsar psr 1913+ 16. The Astrophysical Journal, 253:908–920.

Tetarenko, B. E., Sivakoff, G. R., Heinke, C. O., and Gladstone, J. C. (2016). Watchdog: A comprehensive all-sky database of galactic black hole x-ray binaries. The Astrophysical Journal Supplement Series, 222(2):15.

Thorne, K. S. (1987). Gravitational radiation. Three hundred years of gravitation, pages 330–458.

Tiwari, V. et al. (2015). Regression of environmental noise in ligo data. Classical and Quantum Gravity, 32(16):165014.

Tiwari, V. et al. (2016). Proposed search for the detection of gravitational waves from eccentric binary black holes. Physical Review D, 93(4):043007.

Tutukov, A. and Yungelson, L. (1973). Evolution of massive close binaries. Nauchnye Informatsii, 27:70.

Unnikrishnan, C. S. (2013). Indigo and ligo-india: Scope and plans for gravitational wave research and precision metrology in india. International Journal of Modern Physics D, 22(01):1341010.

V. Tiwari, S. Klimenko, V. N. and Mitselmakher, G. (2015). Reconstruction of chirp mass in searches for gravitational wave transients. Classical and Quantum Gravity, 33(1):01LT01.

Vedovato, G. et al. The cWB 2G clustering algorithms. `https://www.atlas.aei.uni-hannover.de/~waveburst/doc/cwb/man/The-cWB-2G-clustering-algorithms.html#The-cWB-2G-clustering-algorithms`.

Veitch, J. et al. (2015a). Parameter estimation for compact binaries with ground-based gravitational-wave observations using the lalinference software library. Physical Review D, 91(4):042003.

Veitch, J. et al. (2015b). Parameter estimation for compact binaries with ground-based gravitational-wave observations using the LALInference software library. Phys. Rev. D, 91:042003.

Veitch, J. and Vecchio, A. (2010). Bayesian coherent analysis of in-spiral gravitational wave signals with a detector network. Physical Review D, 81(6):062003.

Vinciguerra, S. (2014a). cwb - artificial neural network. `https://www.atlas.aei.uni-hannover.de/~waveburst/doc/cwb/man/ANN.html`.

Vinciguerra, S. (2014b). Gravitational wave searches for transient signals: classification of candidates consistent with binary black hole mergers. `www.infn.it/thesis/PDF/getfile.php?filename=9723-Vinciguerra-magistrale.pdf`.

Vinciguerra, S., Drago, M., Prodi, G. A., Klimenko, S., Lazzaro, C., Necula, V., Salemi, F., Tiwari, V., Tringali, M. C., and Vedovato, G. (2017a). Enhancing the significance of gravitational wave bursts through signal classification. Classical and Quantum Gravity, 34(9):094003.

Vinciguerra, S., Veitch, J., and Mandel, I. (2017b). Accelerating gravitational wave parameter estimation with multi-band template interpolation. Classical and Quantum Gravity, 34(11):115006.

Vines, J., Flanagan, É. É., and Hinderer, T. (2011). Post-1-Newtonian tidal effects in the gravitational waveform from binary inspirals. Phys. Rev. D, 83(8):084051.

Vitale, S. (2016). Multiband Gravitational-Wave Astronomy: Parameter Estimation and Tests of General Relativity with Space- and Ground-Based Detectors. Phys. Rev. Lett., 117:051102.

Weber, J. (1960). Detection and generation of gravitational waves. Physical Review, 117(1):306.

Weiss, R. (1972). Electronically coupled broadband gravitational antenna. Citation:.

Willingale, R., Starling, R. L. C., Beardmore, A. P., Tanvir, N. R., and O'Brien, P. T. (2013). Calibration of x-ray absorption in our galaxy. Monthly Notices of the Royal Astronomical Society, 431(1):394–404.

XMM-Newton SSC Consortium (2017a). 3XMM-DR7. `http://xmmssc.irap.omp.eu/Catalogue/3XMM-DR7/3XMM_DR7.html`. Online; accessed November 2017.

XMM-Newton SSC Consortium (2017b). Table 2.1: A list of all 9710 observations and exposures used for the 3XMM-DR7 source detection. `http://xmmssc.irap.omp.eu/Catalogue/3XMM-DR7/3xmmdr7_obslist.html`. Online; accessed November 2017.

Yu, Y.-W., Zhang, B., and Gao, H. (2013). Bright "Merger-nova" from the Remnant of a Neutron Star Binary Merger: A Signature of a Newly Born, Massive, Millisecond Magnetar. ApJ, 776:L40.

Yuan, W. et al. (2015). Einstein probe-a small mission to monitor and explore the dynamic x-ray universe. arXiv preprint arXiv:1506.07735.

Zevin, M. et al. (2016). Gravity spy: Integrating advanced ligo detector characterization, machine learning, and citizen science. arXiv preprint arXiv:1611.04596.

Zhang, B. and Mészáros, P. (2001). Gamma-Ray Burst Afterglow with Continuous Energy Injection: Signature of a Highly Magnetized Millisecond Pulsar. ApJ, 552:L35–L38.

Zhu, X. et al. (2011). Stochastic gravitational wave background from coalescing binary black holes. The Astrophysical Journal, 739(2):86.

Zwart, S. F. P. and McMillan, S. L. W. (1999). Black hole mergers in the universe. The Astrophysical Journal Letters, 528(1):L17.